

Computer Sciences Corporation

CSC/PM-79/6313

UD3

NASA CR-183444

CSC

(NASA-CR-183444-Rev-3) SPACE TELESCOPE
MOMENTUM MANAGEMENT PROCEDURES, REVISION 3
(Computer Sciences Corp.) 203 p

N90-70183

Unclass
05/89 0232373

SPACE TELESCOPE MOMENTUM

MANAGEMENT PROCEDURES

(REVISION 3)

Prepared for

GODDARD SPACE FLIGHT CENTER

By

COMPUTER SCIENCES CORPORATION

Under

Contract NAS 5-24300
Task Assignment 17100

Prepared by:

Lily C. Chen 1/30/81
Dr. L. C. Chen Date
General Software Corporation

Approved by:

Samuel P. Fallon III 2/3/81
Dr. L. Fallon III Date
Section Manager

Paul B. Davenport 1/30/81
P. B. Davenport Date
Goddard Space Flight Center

S. E. Chevront 2/3/81
S. E. Chevront Date
Department Manager

Conrad R. Sturch 1/29/81
Dr. C. R. Sturch Date
Task Leader

ABSTRACT

This technical memorandum presents an analysis of the minimum energy and cross product momentum management control laws which have been selected for use in the Space Telescope (ST) mission. The ground support requirements for implementation of the minimum energy law are discussed. The impact of each law on routine operations and the scientific program is assessed. Revision 1 of this document included physical interpretations of control laws, suggestions for new procedures, and discussion of published accuracy requirements for the implementation of the original control laws. Revision 2 contained corrections of minor errors in the earlier versions and a more detailed presentation of the implementation of the minimum energy law during maneuvers. The current version of the document, Revision 3, describes recent changes in ST momentum management, including the elimination of reaction wheel speed limits and onboard computation of the nominal momentum profile for use in the operation of the minimum energy law. The discussion of physical interpretation of control laws has been revised and results of new computer studies have been added. Several new explanatory appendixes are also included. Changes from Revision 1 are indicated by vertical lines in the page margins of Sections 1 through 4 and 6.

TABLE OF CONTENTS

<u>Section 1 - Introduction</u>	1-1
<u>Section 2 - Analysis of Onboard Momentum Management Schemes</u>	2-1
2.1 General Analytical Considerations	2-1
2.2 Cross Product Control Law	2-6
2.2.1 Description of Onboard Implementation	2-12
2.2.2 Required Support by the Ground System	2-15
2.3 Minimum Energy Control Law	2-16
2.3.1 Derivation of Minimum Energy Control Law	2-16
2.3.2 Description of Onboard Implementation	2-19
2.3.3 Required Support by the Ground System	2-26
2.3.4 Revisions of Onboard Implementation and Ground Support . . .	2-27
<u>Section 3 - Analytical Consideration for Ground Support of the ME Control Law</u>	3-1
3.1 Overview of Computation Sequence	3-1
3.2 Numerical Integration Technique--Fourth-Order Runge-Kutta Method	3-4
3.3 Computation of Gravity-Gradient Torques	3-5
3.4 Calculation of Geomagnetic Field	3-6
3.4.1 Spherical Harmonic Model	3-6
3.4.2 Magnetic Dipole Model	3-11
<u>Section 4 - Operational Impact of Onboard Control Laws</u>	4-1
4.1 Applicability of the CP and ME Control Laws	4-2
4.2 Impact on Routine Operations	4-9
4.3 Impact on Scientific Program	4-11
4.4 Estimation of Required Resources	4-13
<u>Section 5 - Physical Interpretation of Control Laws and Alternative Techniques</u>	5-1
5.1 Introduction	5-1
5.2 Physical Interpretation and General Discussion	5-3
5.2.1 Closed-Loop Versus Open-Loop Control Laws	5-3
5.2.2 Minimization Criteria	5-10
5.2.3 Comparisons and Modifications	5-12
5.3 Summary of Current Control Laws	5-16

TABLE OF CONTENTS (Cont'd)

Section 5 (Cont'd)

5.4	Alternative Techniques	5-21
5.4.1	Alternative Technique at Inertial Attitudes	5-21
5.4.2	Alternative Technique for Maneuvers	5-23

Section 6 - Mathematical Model Accuracies

6.1	Mathematical Models	6-1
6.2	Accuracy Requirements and Estimates	6-4

Section 7 - Computer Studies of Momentum Management Procedures . . .

7.1	Analytical Software	7-1
7.2	Computer Studies	7-3
7.2.1	Properties of Physical Quantities and Accuracy of H _{NOM} Computations	7-8
7.2.2	Performance of Control Laws at Inertial Attitudes	7-22
7.2.2.1	Performance of Closed-Loop Control Laws	7-23
7.2.2.2	Performance of Open-Loop Control Laws	7-31
7.2.2.3	Performance of Mixed-Mode Control Laws	7-39
7.2.2.4	Comparison of Control Laws	7-44
7.2.3	Performance of Control Laws During Maneuvers	7-51

Appendix A - Derivation of Minimum Wheel Speed Laws

Appendix B - NAMELISTs

Appendix C - Analytical Approximations to Momentum Management Expressions

LIST OF ILLUSTRATIONS

Figure

1-1	Major PCS Hardware Items	1-2
1-2	Reaction Wheel Configuration	1-3
1-3	Magnetic Torquer Configuration	1-4
1-4	Pointing Control System	1-5
2-1	Interaction of Desaturation Law with ST Components	2-2
2-2	Definition of RW Center Speed Momentum Vectors	2-13
2-3	Baseline Diagram of Onboard CP Law Implementation	2-14
2-4	Implementation of ME Control Law	2-21
2-5	Desaturation Intervals	2-23
2-6	Baseline Diagram of Onboard ME Law Implementation	2-25
2-7	Baseline Diagram of Onboard Calculation of Fourier Approximation of Nominal Momentum	2-28
3-1	Computation Flow for the Fourier Coefficients of the Nominal Momentum Profile	3-3
3-2	Coordinate System Definitions	3-7
5-1	Physical Interpretation of the Costate Vector in an Open-Loop Control Law	5-7
5-2	Geometrical Variations of the Desired Torque for a Closed-Loop Control Law	5-9
5-3	Baseline Diagram of Mixed-Mode MWS Control Law at Inertial Attitudes	5-22
5-4	Baseline Diagram of Mixed-Mode MWS Control Law for Maneuvers	5-25
7-1	Sample Orbit Geometries	7-5
7-2	Attitude Definition	7-6
7-3	Variation of Eighth-Order Geomagnetic Field for Three Orbits, Orbit A (B_x , 16-percent deviation; b_y , 18-percent deviation; B_z , 16-percent deviation, $ B $, 11-percent deviation.)	7-10
7-4	Variation of Eighth-Order Geomagnetic Field for Three Orbits, Orbit B (B_x , 14-percent deviation; B_y , 16-percent deviation; B_z , 14-percent deviation; $ B $, 18-percent deviation.)	7-11
7-5	Comparison of Eighth-Order Geomagnetic Field Over Half-Orbit Intervals, Orbit A (B_x , 34-percent deviation; B_y , 37-percent deviation; B_z , 34-percent deviation, $ B $, 39-percent deviation.)	7-12

LIST OF ILLUSTRATIONS (Cont'd)

Figure

7-6	Comparison of Eighth-Order Geomagnetic Field Over Half-Orbit Intervals, Orbit B (B_x , 20-percent deviation; B_y , 32-percent deviation; B_z , 32-percent deviation; $ B $, 27-percent deviation.)	7-13
7-7	Comparison of Second- and Eighth-Order Geomagnetic Fields, Orbit A	7-14
7-8	Gravity-Gradient Torque With Secular Term in Y Direction	7-15
7-9	$ \hat{H}_{NOM} $ Profiles With Constant and Updated Costate Vectors, Orbit B	7-17
7-10	Variation in \hat{H}_{NOM} for Three Orbits, Orbit B	7-18
7-11	Errors in First-, Second-, and Third-Order Fourier Representation of \hat{H}_{NOM} for Cycling Time of One Half-Orbit	7-19
7-12	Errors in, Second-, Fourth- and Sixth-Order Fourier Representation of \hat{H}_{NOM} for Cycling Time of One Orbit	7-20
7-13	Parametric Study of K_M	7-24
7-14	Dependence of Maximum Wheel Speed on K_Σ	7-25
7-15	Dependence of Energy Consumption on K_Σ	7-27
7-16	Comparison of Closed-Loop Control Law Performance for Different Orbit Geometries	7-30
7-17	Comparison of Control Laws Under Nominal and Error Conditions	7-49
7-18	Comparison of Wheel Speed Settling Times Required by Different Control Laws	7-50

LIST OF TABLES

Table

4-1	Comparison of Peak Reaction Wheel Speeds for the CP and ME Control Laws	4-3
4-2	Maximum Lead and Lag Times	4-5
4-3	Performance of the Modified CP Law and the ME Law With Lead and Lag Times for 14 Identical Maneuvers	4-7
5-1	Summary of Equations for Current Control Laws	5-4
5-2	Physical Interpretation of \bar{T}_M for Different Minimization Criteria	5-11
5-3	Summary of Control Law Equations	5-17
6-1	Mathematical Model Accuracies and Requirements	6-7
7-1	Orbital Parameters Used in Studies	7-4
7-2	Attitudes Used in Computer Studies	7-7
7-3	Geometry Dependence of Closed-Loop Control Laws	7-28
7-4	Closed-Loop Control Law Performance for Comparison of Different Attitude Geometries	7-29
7-5	Effects on Closed-Loop Control Laws Due to Coil and Wheel Failures	7-32
7-6	Initial Conditions Study for Closed-Loop Control Laws	7-33
7-7	Comparison of Open-Loop Control Law Performance for Different Orbit Geometries	7-35
7-8	Comparison of Open-Loop Control Law Performance for Different Attitude Geometries	7-36
7-9	Comparison of Open-Loop Control Law Performance With Different Minimization Criteria	7-38
7-10	Initial Conditions Study for Open-Loop Control Laws	7-39
7-11	Comparison of Mixed-Mode Control Law Performance for Different Orbit Geometries	7-41
7-12	Comparison of Mixed-Mode Control Law Performance for Different Attitude Geometries	7-42
7-13	Comparison of Mixed-Mode Control Law Performance With Different Minimization Criteria	7-43
7-14	Initial Conditions Study for Mixed-Mode Control Laws	7-44
7-15	Comparison of the Mixed-Mode Law With the Open-Loop Under Nominal Conditions With ME Criterion	7-45
7-16	Comparison of the Mixed-Mode Law With the Open-Loop Law Under Nominal Conditions With MWS Criterion	7-46
7-17	Comparison of the Mixed-Mode MWS Law With the Current ME Law Under Nominal Conditions	7-48
7-18	Simulated Maneuvers	7-52

LIST OF TABLES (Cont'd)

Table

7-19	Reaction Wheel Speed Following Maneuvers	7-54
7-20	Energy Consumption for Maneuvers	7-55
7-21	Maneuvers Under Abnormal Conditions (Maneuver 1, Orbit Type A)	7-58

SECTION 1 - INTRODUCTION

The Space Telescope (ST) is an astronomical observatory to be launched in late 1984 by the Space Shuttle into a nominal 565-kilometer circular orbit.

The Pointing Control System (PCS) provides the attitude reference and control stability for the ST. The most challenging requirement of the PCS is the pointing stability of 0.007 arc-second (one sigma) (Reference 1-1).

The PCS uses software residing in the onboard flight computer and hardware located throughout the Support Systems Module (SSM) to accomplish these goals. Major hardware components used by the PCS are shown in Figure 1-1. The Sun sensors and fixed-head star trackers are required primarily for initial attitude determination and recovery. Each of the three fine guidance sensors (FGSs) track star images within a quadrant of the telescope focal surface extending from 10.2 to 14 arc-minutes off the optical (+V1) axis (Reference 1-2). The output of two FGSs is used by the PCS for position error and rate determination. Additional rate information is provided by the three rate gyro assemblies (RGAs) that contain a total of six gyros, four of which are used for nominal operation. The PCS actuates torques through four reaction wheel assemblies (RWAs) mounted in a skewed configuration. Excess speed is removed from the reaction wheels by a set of four magnetic torquer (MT) bars that interact with the Earth's magnetic field. The torque generated by the MTs is applied directly to the SSM body and then transferred to the reaction wheels. The configurations of the RWAs and MTs are shown in Figures 1-2 and 1-3, respectively. Measurements of the geomagnetic field are provided to the PCS by two redundant three-axis magnetometers.

The PCS uses the Digital 224 Flight Computer to process input from the Sun sensors, fixed-head star trackers, FGSs, RGAs, and magnetometers and to command the MTs and RWAs. Figure 1-4 is a block diagram of the PCS. This document is primarily concerned with operational and scientific impacts

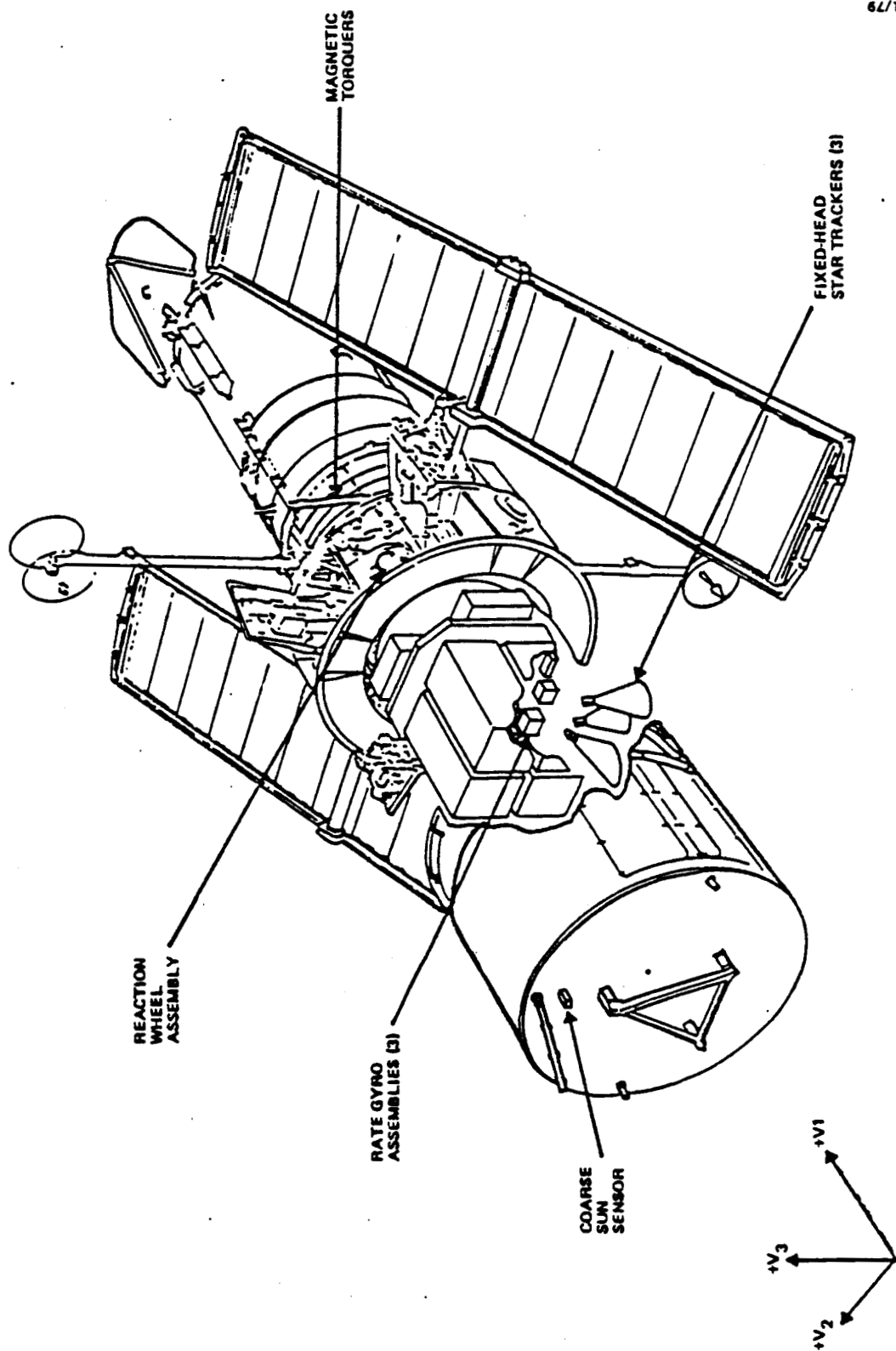


Figure 1-1. Major PCS Hardware Items. (The figure is adapted from Reference 1-1.)

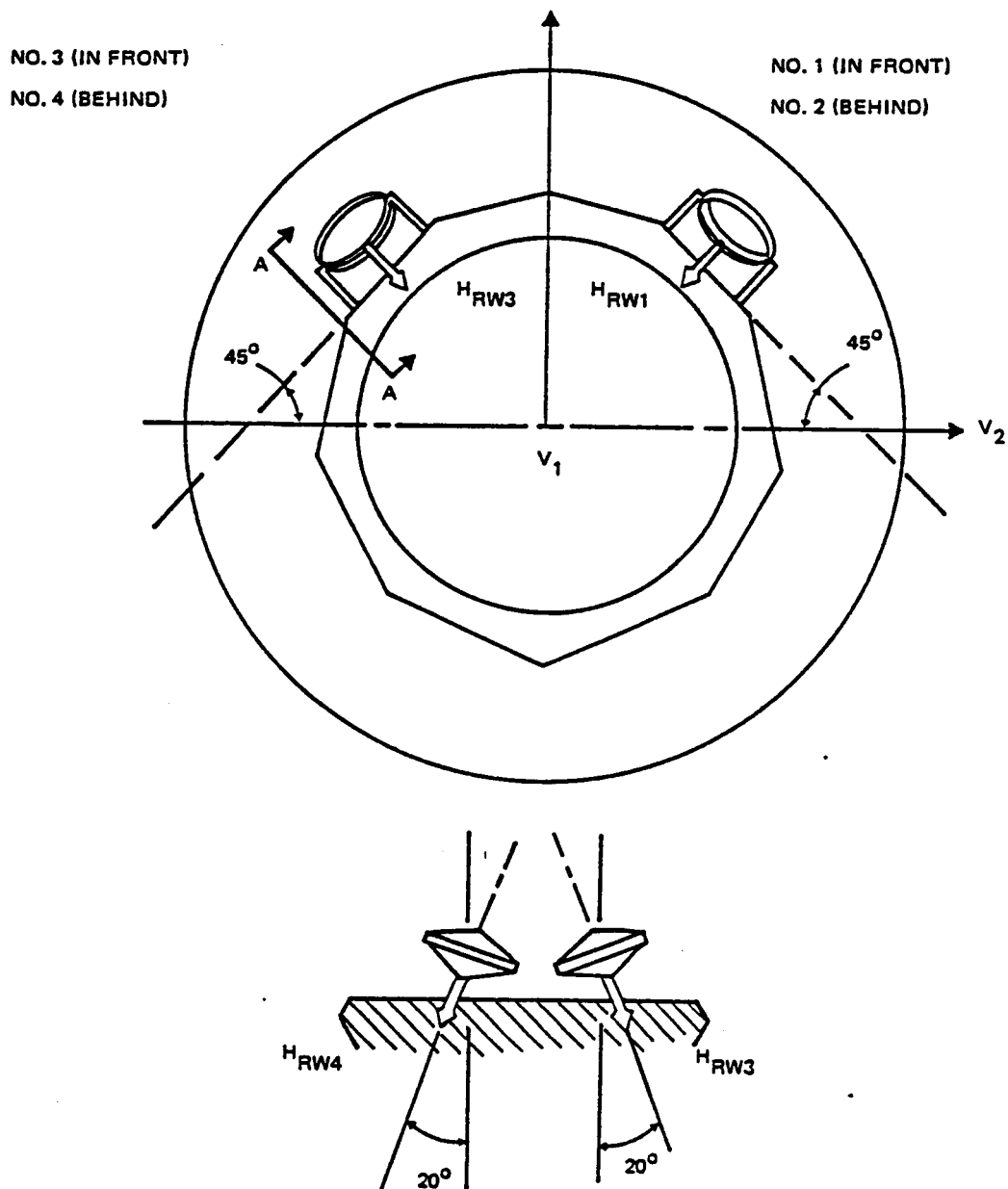


Figure 1-2. Reaction Wheel Configuration. (The figure is adapted from Reference 1-2.)

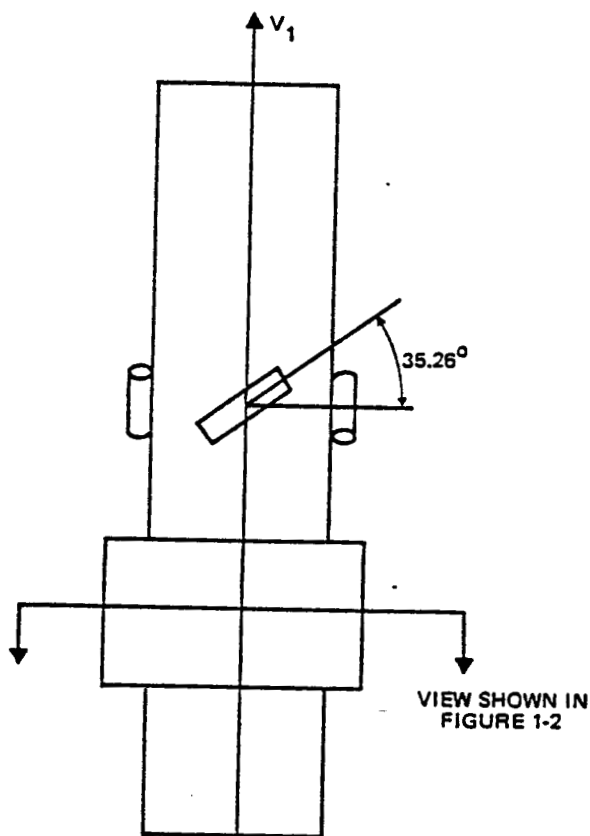
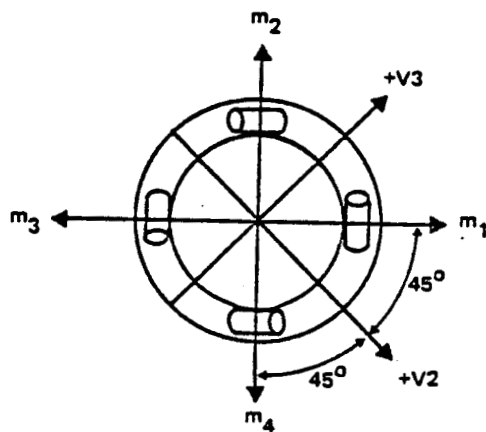


Figure 1-3. Magnetic Torquer Configuration. (The figure is adapted from Reference 1-2.)

of magnetic desaturation or momentum management control laws, i.e., the methods by which the commanded magnetic torques are computed for control of the reaction wheel speeds.

To achieve the 0.007-arc-second stability required in the fine pointing mode, vibrations generated by the rotating reaction wheels must not excite significant ST bending modes. Because the dominant vibration produced by the RWAs occurs at the rotational frequency of the reaction wheels, it is required that reaction wheel speeds remain below approximately 600 rpm (10 hertz) while the ST is in the fine pointing mode (References 1-2 through 1-4).¹ The momentum management control is required to limit the reaction wheels to 10 hertz under normal operating conditions and also in the case of RWA or MT failure. It is also desired that the smallest possible magnetic dipole moments be employed to keep the magnetic contamination of the ST scientific instruments within acceptable levels.

Several momentum management control laws have been proposed for desaturating the reaction wheels (References 1-2 and 1-3), two of which are recommended by Lockheed Missiles and Space Company. These are the minimum energy (ME) control law and the cross product (CP) control law. The ME control law minimizes the amount of energy required to generate the control magnetic dipole over a given time interval, which will bring the SSM angular momentum to a desired final value. The CP law is a closed-loop law that computes a deterministic control magnetic dipole proportional to the error signal with the constraint that it always be perpendicular to the Earth's magnetic field. The CP law can be implemented entirely onboard the ST and must be used during initial phases of the mission and during safe mode operations

¹Limiting reaction wheel speeds to 10 hertz is no longer a requirement of ST momentum management. Revised requirements are discussed in Sections 2.3.4 and 3.

when interface with the Space Telescope Operations Control Center (STOCC) is unreliable. The ME law now requires little ground support.

Section 2 presents an analysis of the CP and ME control laws, including derivations of the laws, descriptions of onboard implementation, and delineation of the ground system support requirements. Section 3 contains an analytical study of computation required on the ground for implementation of the ME law. In Section 4, the impact of each law on routine operations and the scientific program is discussed. Estimates of resources required to support each law also are given in Section 4. Section 5 discusses the physical interpretation of control laws. This section describes control laws in general, summarizes the current control laws implemented for ST, and presents alternative techniques for both inertial targets and maneuvers. Section 6 delineates the mathematical models used in the current control laws implemented for ST and reviews the published accuracy requirements and estimates for these models. Section 7 describes the results of new computer studies of momentum management procedures. Two appendixes derive analytical expressions and a third describes computer program parameters.

REFERENCES

- 1-1. Lockheed Missiles and Space Company, LMSC 4171847A, ST Mission Operations Requirements, DR OP-01, volume III, August 1979
- 1-2. A. Wernli, "Minimization of Reaction Wheel Momentum Storage with Magnetic Torquers," J. Astronautical Sciences, vol. 26, no. 3, p. 257, July-September 1978
- 1-3. Lockheed Missiles and Space Company, LMSC-HREC TM D496086, Reaction Wheel Speed Minimization through Magnetic Desaturation, A. Wernli, November 1976
- 1-4. --, SE-03, Section H, Space Telescope Project, Support Systems Module, Appendix 3, April 1979

SECTION 2 - ANALYSIS OF ONBOARD MOMENTUM MANAGEMENT SCHEMES

2.1 GENERAL ANALYTICAL CONSIDERATIONS

This section provides some analytical considerations which apply in general to all momentum management desaturation control laws. Specific considerations for the cross product (CP) and minimum energy (ME) control laws are given in Sections 2.2 and 2.3, respectively.

The interaction of the desaturation law with the components of the ST is schematically shown in Figure 2-1 (adopted from Reference 2-1). For any given measured reaction wheel (RW) system angular momentum, \vec{H}_{RW} , the desaturation law computes the commanded magnetic dipole moment, $\vec{\mu}_T$, for the four magnetic torquers. The components of $\vec{\mu}_T$ then combine to form the system magnetic dipole moment vector, $\vec{\mu}_M$, through the following relation:

$$\vec{\mu}_M = \begin{bmatrix} s & s & s & s \\ c & -c & -c & c \\ c & c & -c & -c \end{bmatrix} \vec{\mu}_T = M \vec{\mu}_T \quad (2-1)$$

where $s = \sin 35.26^\circ$

$$c = (1/\sqrt{2})\cos 35.26^\circ$$

The matrix M in Equation (2-1) is called the magnetic coil mounting matrix, which results from the magnetic torquer mounting configuration shown in Figure 1-3. The interaction between the system magnetic dipole moment $\vec{\mu}_M$ and the geomagnetic field \vec{B} produces a magnetic torque given by

$$\vec{T}_M = \vec{\mu}_M \times \vec{B} \quad (2-2)$$

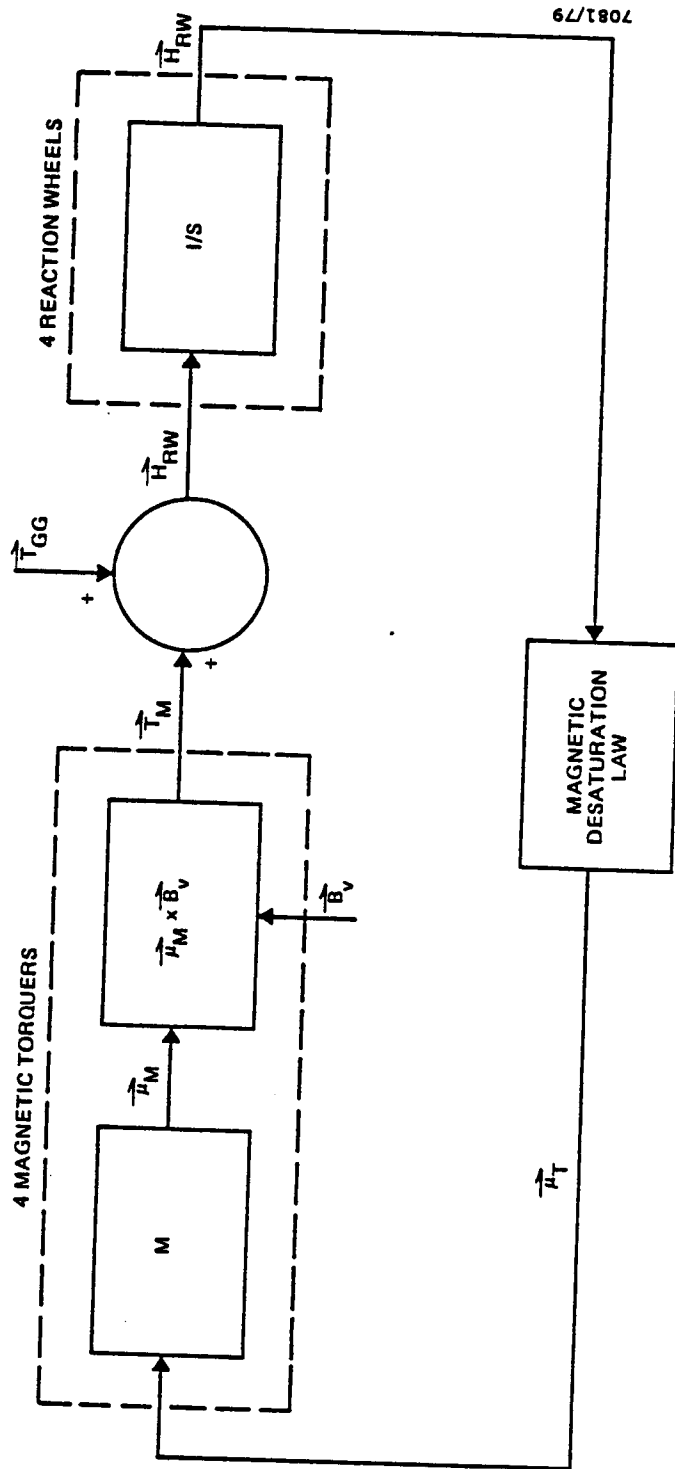


Figure 2-1. Interaction of Desaturation Law With ST Components

This magnetic torque \vec{T}_M is the external torque produced by the momentum management desaturation laws to counteract the environmental disturbance torques, which are dominated by the gravity-gradient torque \vec{T}_{GG} , and thus to reduce the buildup of the system momentum and to prevent the reaction wheel speed saturation. It is evident from Equation (2-2) that at any instant no magnetic torque can be produced in the direction of the geomagnetic field. Only because the direction of the geomagnetic field changes in the course of an orbit can dumping of momentum occur in three axes.

With the ST in an inertial attitude, all external torques are absorbed by the reaction wheels. That is,

$$\dot{\vec{H}}_{RW} = \vec{T}_M + \vec{T}_{GG} \quad (2-3)$$

The dumping of reaction wheel momentum \vec{H}_{RW} is thus achieved by the magnetic torque \vec{T}_M through Equation (2-3). The momentum dumping process results in a new reaction wheel momentum which is fed back to the momentum management desaturation laws for the computation of the next desaturation loop. Equation (2-3) can be generalized to cover the cases of maneuvers by replacing \vec{H}_{RW} by the total system momentum \vec{H}_T . That is,

$$\dot{\vec{H}}_T = \dot{\vec{H}}_{RW} + \dot{\vec{H}}_V = \vec{T}_M + \vec{T}_{GG} \quad (2-4)$$

where \vec{H}_V is the vehicle momentum.

The four reaction wheels are mounted in a configuration as shown in Figure 1-2. The relation between the total reaction wheel system momentum and the individual RW angular velocities, $\vec{\omega}_{RW}$, are given by

$$\vec{H}_{RW} = \begin{bmatrix} a & -a & a & -a \\ -b & -b & b & b \\ -b & -b & -b & -b \end{bmatrix} I_{RW} \vec{\omega}_{RW} = W I_{RW} \vec{\omega}_{RW} \quad (2-5)$$

where $a = \sin 20^\circ$, $b = (1/\sqrt{2})\cos 20^\circ$, I_{RW} is the reaction wheel inertia, and the matrix W is called the reaction wheel mounting matrix.

Since the method of Lagrange multipliers is used in the derivation of both the CP law and the ME law, the mathematics used in this method is outlined below. The problem is a minimization problem of the general form

$$J = h(\vec{x}(t_f)) + \int_{t_0}^{t_f} g(\dot{\vec{x}}, \vec{x}, \vec{u}) dt \quad (2-6)$$

with the constraint

$$f(\dot{\vec{x}}, \vec{x}, \vec{u}, t) = 0 \quad (2-7)$$

The necessary conditions for a minimum of J are

$$\frac{\partial g_a}{\partial \vec{x}} - \frac{d}{dt} \left(\frac{\partial g_a}{\partial \dot{\vec{x}}} \right) = 0 \quad (2-8)$$

$$\frac{\partial g_a}{\partial \vec{u}} = 0 \quad (2-9)$$

$$\left. \frac{\partial g_a}{\partial \dot{\vec{x}}} \right|_{t=t_f} = 0 \quad (\text{boundary condition}) \quad (2-10)$$

where

$$g_a = g(\vec{x}, \dot{\vec{x}}, \vec{u}) + \left(\frac{\partial h}{\partial \dot{\vec{x}}} \right)^T \dot{\vec{x}} + \vec{P}^T \vec{f}(\vec{x}, \dot{\vec{x}}, \vec{u}, t) \quad (2-11)$$

and where \vec{x} = state vector

\vec{u} = independent (control) variable

\vec{P} = costate vector (Lagrange multipliers)

2.2 CROSS PRODUCT CONTROL LAW

The CP law is a closed-loop control law with the actuating signal proportional to the error signal. In other words, it provides the commanded momentum dipole moments, based on the measured reaction wheel momentum, to achieve the momentum desaturation instantaneously.

The original CP law is a simple control law which generates a control dipole along the direction perpendicular to the geomagnetic field with the assumption that the vehicle is in an inertial attitude, i.e., that all external torques are absorbed by the reaction wheels. This CP law is later modified (Reference 2-2) to (1) use the total system momentum \vec{H}_T rather than the RW momentum \vec{H}_{RW} for absorption of the external torques (i.e., use Equation (2-4) rather than Equation (2-3)) so that the law can be used for both maneuvers and observations; (2) minimize the norm of the reaction wheel speed vector to keep the reaction wheel speed during an observation minimal; and (3) add the reaction wheel center speed control loop so that the RW speeds will automatically center after a maneuver and remain centered during an observation. The derivation of the modified CP law, which will be used onboard the ST, is given below.

At any given time in the orbit, the desired magnetic torque, \vec{T}_D , is the one that cancels the gravitational gradient torque \vec{T}_{GG} and reduces the total system momentum \vec{H}_T . From Equation (2-4), by changing \vec{T}_M to \vec{T}_D and choosing the desired change in \vec{H}_T , $\dot{\vec{H}}_T$, to be in the direction of but opposite to \vec{H}_T ,

$$\vec{T}_D = -\vec{T}_{GG} - K_M \vec{H}_T \quad (2-12)$$

where K_M is the positive constant commonly called the magnetic gain.

However, \vec{T}_D given in Equation (2-12) cannot always be achieved by the magnetic torquers because the magnetic torque \vec{T}_M given by Equation (2-2) has to be perpendicular to the geomagnetic field. One way of determining \vec{T}_M is to let¹

$$\vec{T}_M = \begin{bmatrix} K_1 & 0 & 0 \\ 0 & K_2 & 0 \\ 0 & 0 & K_3 \end{bmatrix} \vec{T}_D \quad (2-13)$$

and to determine the gain factors K_1 , K_2 , and K_3 by minimizing the mean square reaction wheel speed, $\vec{\omega}_{RW}^T \vec{\omega}_{RW}$, under the constraint

$$\vec{T}_M \cdot \vec{B} = 0 \quad (2-14)$$

From the minimum norm reaction wheel momentum distribution law (Reference 2-2), $\vec{\omega}_{RW}^T \vec{\omega}_{RW}$ is minimum when expressed in the following form:

$$\begin{aligned} \vec{\omega}_{RW}^T \vec{\omega}_{RW} &= \frac{1}{I_{RW}^2} \vec{H}_{RW}^T (W W^T)^{-1} \vec{H}_{RW} \\ &= \frac{1}{4b^2 I_{RW}^2} \vec{H}_{RW}^T \begin{bmatrix} b^2/a^2 & 0 & 0 \\ 0 & 1 & 0 \\ 0 & 0 & 1 \end{bmatrix} \vec{H}_{RW} \end{aligned} \quad (2-15)$$

where a and b are defined in Equation (2-5).

¹Appendix A gives an alternative derivation of the CP law without this assumption. |

Since the resulting RW angular momentum \vec{H}_{RW} during an observation is proportional to the difference between the desired magnetic torque \vec{T}_D and the actual magnetic torque \vec{T}_M , it is seen from Equations (2-13) and (2-15) that $\vec{\omega}_{RW}^T \vec{\omega}_{RW}$ can be minimized by minimizing the quantity

$$\left[\frac{b}{a} T_{D_1} (K_1 - 1) \right]^2 + \left[T_{D_2} (K_2 - 1) \right]^2 + \left[T_{D_3} (K_3 - 1) \right]^2 \quad (2-16)$$

subject to the constraint of Equation (2-14), i.e.,

$$K_1 T_{D_1} B_1 + K_2 T_{D_2} B_2 + K_3 T_{D_3} B_3 = 0 \quad (2-17)$$

Applying the method of Lagrange multipliers gives

$$\begin{aligned} 2 \left(\frac{b}{a} T_{D_1} \right)^2 (K_1 - 1) + \lambda T_{D_1} B_1 &= 0 \\ 2 T_{D_2}^2 (K_2 - 1) + \lambda T_{D_2} B_2 &= 0 \\ 2 T_{D_3}^2 (K_3 - 1) + \lambda T_{D_3} B_3 &= 0 \\ T_{D_1} B_1 K_1 + T_{D_2} B_2 K_2 + T_{D_3} B_3 K_3 &= 0 \end{aligned} \quad (2-18)$$

where λ is the Lagrange multiplier.

Solving for K_1 , K_2 , K_3 , and λ from Equation (2-18) yields

$$\begin{aligned}
 K_1 &= 1 - \frac{\left(\frac{a}{b}\right)^2 B_1 \vec{T}_D \cdot \vec{B}}{T_{D1} \vec{B}' \cdot \vec{B}} \\
 K_2 &= 1 - \frac{B_2 \vec{T}_D \cdot \vec{B}}{T_{D2} \vec{B}' \cdot \vec{B}} \\
 K_3 &= 1 - \frac{B_3 \vec{T}_D \cdot \vec{B}}{T_{D3} \vec{B}' \cdot \vec{B}} \\
 \lambda &= \frac{2 \vec{T}_D \cdot \vec{B}}{\vec{B}' \cdot \vec{B}}
 \end{aligned} \tag{2-19}$$

where

$$\vec{B}' = \left[\left(\frac{a}{b}\right)^2 B_1, B_2, B_3 \right]^T$$

Substituting Equation (2-19) into Equation (2-13) gives

$$\begin{aligned}
 \vec{T}_M &= \vec{T}_D - \frac{\vec{T}_D \cdot \vec{B}}{\vec{B}' \cdot \vec{B}} \vec{B}' \\
 &= \frac{(\vec{B}' \times \vec{T}_D) \times \vec{B}}{\vec{B}' \cdot \vec{B}}
 \end{aligned} \tag{2-20}$$

Hence, by comparing Equation (2-20) with Equation (2-2),

$$\vec{\mu}_M = \frac{\vec{B}' \times \vec{T}_D}{\vec{B}' \cdot \vec{B}} \quad (2-21)$$

Substituting Equation (2-15) into Equation (2-1) results in

$$M \vec{\mu}_T = \frac{\vec{B}' \times \vec{T}_D}{\vec{B}' \cdot \vec{B}} \quad (2-22)$$

According to the pseudo-inverse law, the power loss in the magnetic coil will be minimal if the magnetic moment is distributed among the four electromagnets by the following:

$$\vec{\mu}_T = M^T (MM^T)^{-1} \frac{\vec{B}' \times \vec{T}_D}{\vec{B}' \cdot \vec{B}} \quad (2-23)$$

Thus, the basic CP law for both observations and maneuvers is obtained by substituting Equation (2-12) into Equation (2-23).

$$\vec{\mu}_T = -M^T (MM^T)^{-1} \frac{\vec{B}' \times [\vec{T}_{GG} + K_M (W I_{RW} \vec{\omega}_{RW} + I_V \vec{\omega}_V)]}{\vec{B}' \cdot \vec{B}} \quad (2-24)$$

where \vec{T}_{GG} = calculated vehicle gravitational gradient torque

$\vec{\omega}_{RW}$ = sensed reaction wheel speeds

$\vec{\omega}_V$ = sensed vehicle rate

\vec{B} = sensed Earth magnetic field

I_V = vehicle inertia matrix

I_{RW} = reaction wheel inertia matrix

Computer studies show that $K_M = 2 \Omega_o$ (Ω_o = orbital rate) minimizes the reaction wheel speed swings during an observation.

The CP law given in Equation (2-24) is further modified by incorporating the reaction wheel center speed control loops to keep the reaction wheel center speeds at zero. This results in (Reference 2-2) adding two additional terms in \vec{T}_D . That is,

$$\vec{T}_D = -\vec{T}_{GG} - K_M (\vec{H}_T + K_P \vec{H}_{CSD} + K_\Sigma \vec{\Sigma}) \quad (2-25)$$

where \vec{H}_{CSD} is the RW center speed momentum with dead zone, $\vec{\Sigma}$ is the sum of the RW center speed momenta with limits (\vec{H}_{CSL}) for all passes through the CP law, and K_P and K_Σ are constants. The momentum vectors \vec{H}_{CSD} and $\vec{\Sigma}$ are defined in the following:

$$\begin{aligned} (H_{CSD})_1 &= 0 & \text{if } |(H_{CS})_1| \leq H_{NL1} \\ &= (H_{CS})_1 - H_{NL1} & \text{if } (H_{CS})_1 > H_{NL1} \\ &= (H_{CS})_1 + H_{NL1} & \text{if } (H_{CS})_1 < -H_{NL1} \\ \\ (H_{CSD})_i &= 0 & \text{if } |(H_{CS})_i| \leq H_{NL2} \\ &= (H_{CS})_i - H_{NL2} & \text{if } (H_{CS})_i > H_{NL2} \\ &= (H_{CS})_i + H_{NL2} & \text{if } (H_{CS})_i < -H_{NL2} \end{aligned} \quad (i = 2, 3) \quad (2-26)$$

$$\begin{aligned} (H_{CSL})_1 &= (H_{CS})_1 & \text{if } |(H_{CS})_1| \leq H_{NL1} \\ &= H_{NL1} & \text{if } (H_{CS})_1 > H_{NL1} \\ &= -H_{NL1} & \text{if } (H_{CS})_1 < -H_{NL1} \end{aligned}$$

$$\begin{aligned}
(H_{CSL})_i &= (H_{CS})_i && \text{if } |(H_{CS})_i| \leq H_{NL2} \\
&= H_{NL2} && \text{if } (H_{CS})_i > H_{NL2} \\
&= -H_{NL2} && \text{if } (H_{CS})_i < -H_{NL2}
\end{aligned} \quad (i = 2, 3)$$

$$\vec{\Sigma} = \sum \vec{H}_{CSL} \quad (\text{sum over all passes through the CP law})$$

where

$$\begin{aligned}
\vec{H}_{CS} &= \text{total system momentum due to RW center speeds} \\
&= W I_{RW} \vec{\omega}_{CS} \\
\vec{\omega}_{CS} &= 1/2 (\vec{\omega}_{RW_{MAX}} + \vec{\omega}_{RW_{MIN}}) \\
\vec{\omega}_{RW_{MAX}} &= \text{maximum RW speed over last half orbit} \\
\vec{\omega}_{RW_{MIN}} &= \text{minimum RW speed over last half orbit} \\
H_{NL1} &= \text{RW center speed control loop first axis nonlinearities breakpoint} \\
H_{NL2} &= \text{RW center speed control loop second and third axes nonlinearities breakpoint}
\end{aligned}$$

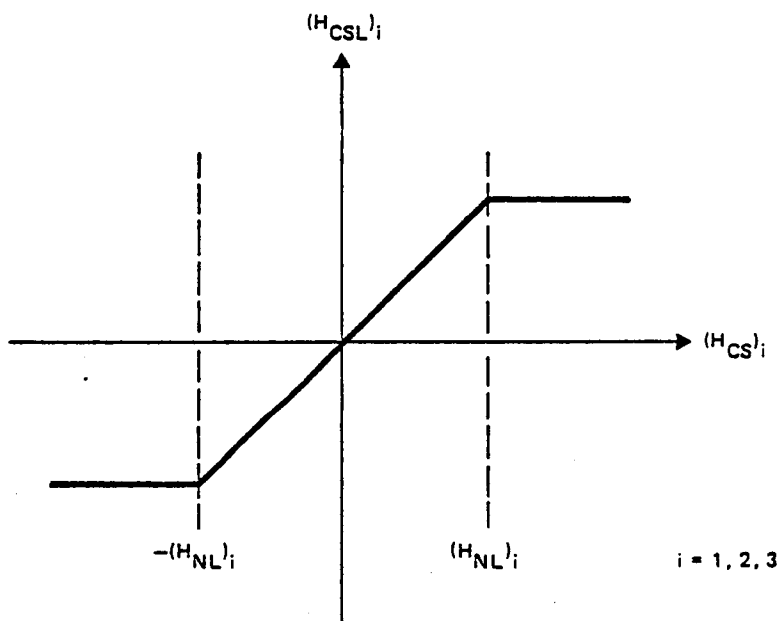
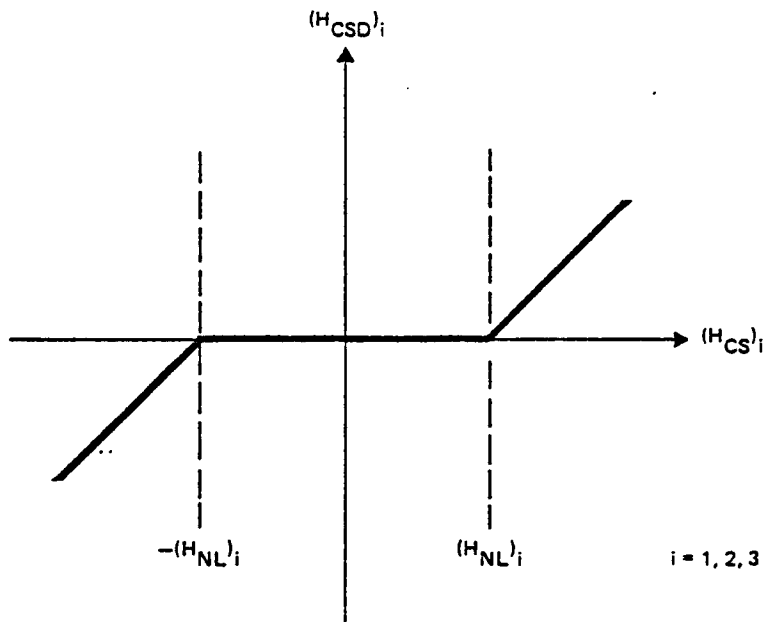
The relations between \vec{H}_{CSD} , \vec{H}_{CSL} , and \vec{H}_{CS} given in Equation (2-26) are shown in Figure (2-2). The nominal values for H_{NL1} , H_{NL2} , K_P and K_Σ are determined to be:

$$\begin{aligned}
H_{NL1} &= 10.2 \\
H_{NL2} &= 19.8 \\
K_P &= 2.828 \\
K_\Sigma &= 0.06659
\end{aligned} \quad (2-27)$$

with all quantities expressed in MKS units.

2.2.1 Description of Onboard Implementation

The ST onboard software requirements are described in References 2-3 and 2-4. The onboard implementation of the CP desaturation law is summarized in Figure 2-3. A RW center speed computation module and a gravity-gradient model



$$(H_{NL})_1 = H_{NL1}$$

$$(H_{NL})_2 = (H_{NL})_3 = H_{NL2}$$

7081/79

Figure 2-2. Definition of RW Center Speed Momentum Vectors

must be implemented onboard to compute the desired torque \vec{T}_D . The RW center speed computation module computes the vectors \vec{H}_{CSD} and $\vec{\Sigma}$ necessary for the RW center speed control based on the RW speed measurements $\vec{\omega}_{RW}$ sensed by the RW tachometer over the last half-orbit period. With \vec{H}_{CSD} and $\vec{\Sigma}$ computed, the desired torque \vec{T}_D is then calculated using the gravity-gradient torque \vec{T}_{GG} obtained from the gravity-gradient model and the RW speed and vehicle speed sensed by the RW tachometer and the rate gyro assembly (RGA), respectively. After \vec{T}_D is computed, the magnetic dipole moment command $\vec{\mu}_T$ is then calculated, using the geomagnetic field sensed by the magnetometer, and sent to the magnetic coils to generate the magnetic torque necessary for the momentum desaturation.

2.2.2 Required Support by the Ground System

As shown in Figure 2-3, the implementation of the CP law requires essentially no support from the ground system. However, because of the finite possibility that the RWA speed may exceed the 10-hertz limit¹ using the CP law, a simulator on the ground may be necessary for target screening and control law selection. This will not only increase the amount of ground software support, but also cause some operational impact. Therefore, it is recommended that further studies be performed to define the cases where the CP law is not applicable so that the necessity of the simulator can be removed. More discussion regarding this subject is given in Section 4.

¹Limiting reaction wheel speeds to 10 hertz is no longer a requirement of ST momentum management. Simulations for this purpose are not necessary.

2.3 MINIMUM ENERGY CONTROL LAW

2.3.1 Derivation of Minimum Energy Control Law

The ME control law is designed to minimize the energy required by the magnetic torquers to dump a given amount of angular momentum during a specified time interval called the desaturation period. The equations derived in this subsection are limited to the cases of inertial attitudes. For the cases of slew maneuvers, proper coordinate transformations from momentary spacecraft coordinates to inertial coordinates are required (Reference 2-5).

The energy lost in the magnetic coils within a desaturation period of t_o to t_f is given by

$$E = \frac{k}{2} \int_{t_o}^{t_f} \vec{\mu}_T^T \vec{\mu}_T dt \quad (2-28)$$

where k is a constant.

From Equations (2-1) to (2-3), the magnetic dipole moment $\vec{\mu}_T$ is subject to the following differential equation constraint:

$$\tilde{B} M \vec{\mu}_T - \vec{T}_{GG} + \dot{\vec{H}}_{RW} = \vec{0} \quad (2-29)$$

where

$$\tilde{B} = \begin{bmatrix} 0 & -B_3 & B_2 \\ B_3 & 0 & -B_1 \\ -B_2 & B_1 & 0 \end{bmatrix} \quad (2-30)$$

Thus, the ME law is to determine the magnetic dipole moment vector $\vec{\mu}_T$ by minimizing the quantity E given by Equation (2-28) subject to the constraint of Equation (2-29). Applying the method of Lagrange multipliers, Equation (2-11) gives

$$g_a = k \left[\frac{1}{2} \vec{\mu}_T^T \vec{\mu}_T + \vec{P}^T (\tilde{B} M \vec{\mu}_T - \vec{T}_{GG} + \dot{\vec{H}}_{RW}) \right] \quad (2-31)$$

Then, from Equations (2-8) and (2-9), the following necessary conditions are derived:

$$\frac{d}{dt} (\vec{P}) = 0 \quad (2-32)$$

$$\vec{\mu}_T + M^T \tilde{B}^T \vec{P} = 0 \quad (2-33)$$

Equation (2-32) implies that \vec{P} , the vector of Lagrange multipliers or the costate vector, is constant. Solving for $\vec{\mu}_T$ from Equation (2-33) gives

$$\begin{aligned} \vec{\mu}_T &= - M^T \tilde{B}^T \vec{P} \\ &= M^T \tilde{B} \vec{P} \\ &= M^T \vec{B} \times \vec{P} \end{aligned} \quad (2-34)$$

Substituting Equation (2-34) into Equation (2-29) and integrating over the desaturation period yields

$$\begin{aligned} \vec{H}_{RW}(t_f) - \vec{H}_{RW}(t_o) = & \int_{t_o}^{t_f} \tilde{B} M M^T \tilde{B}^T dt \vec{P} \\ & + \int_{t_o}^{t_f} \vec{T}_{GG} dt \end{aligned} \quad (2-35)$$

Solving for \vec{P} from Equation (2-35) gives

$$\vec{P} = \left[\int_{t_o}^{t_f} \tilde{B} M M^T \tilde{B}^T dt \right]^{-1} \vec{H}_D \quad (2-36)$$

where

$$\vec{H}_D = \vec{H}_{RW}(t_f) - \vec{H}_{RW}(t_o) - \int_{t_o}^{t_f} \vec{T}_{GG} dt \quad (2-37)$$

The ME desaturation law is presented by Equations (2-34), (2,36), and (2-37). The momentum \vec{H}_D defined in Equation (2-37) is the total momentum to be dumped during the desaturation interval t_o to t_f .

2.3.2 Description of Onboard Implementation

2.3.2.1 Implementation of the ME Law

The ME law was originally developed by Dr. John Glaese et al. (Reference 2-6). The conventional implementation of the ME law is to use a half-orbit period as the desaturation interval and to update the costate vector \vec{P} at the end of each desaturation period. The RW system momentum at the end of each desaturation interval, $\vec{H}_{RW}(t_f)$, is constant and is selected to center the positive and negative RW speed excursions. This implementation is schematically shown in Figure 2-4(a). The desaturation period is set at half an orbit period to include the major variations in the geomagnetic field and to be compatible with the period of gravity-gradient disturbances. The result is that only the nonperiodic portion of the accumulated gravity-gradient momentum is dumped, and no attempt is made to counteract the periodic portion.

Since the ME desaturation law is open-loop in nature (that is, the RW system momentum \vec{H}_{RW} couples into the desaturation law only at the beginning of a desaturation period), a desaturation interval of as long as half an orbit period can allow \vec{H}_{RW} to drift to large values in the presence of offnominal conditions such as coil or RW failures. Thus, the conventional ME law only performs satisfactorily if either no failure conditions are present or if only detected failure conditions are present. To resolve this problem, it is necessary to modify the implementation of the conventional ME law.

The purpose of the modification is to reduce the drawback of the open-loop process by shortening the desaturation period and increasing the updating frequency of the costate vector computation, while at the same time keeping the advantages of using the half-orbit period as the desaturation interval by replacing the $\vec{H}_{RW}(t_f)$ in Equation (2-37) with a nominal RW system momentum $\vec{H}_{NOM}(t_f)$. This nominal momentum profile $\vec{H}_{NOM}(t)$ is the RW system momentum time history obtained from the conventional ME law with a half-orbit desaturation period and updating interval. $\vec{H}_{NOM}(t)$ can be approximated by a first-order

Fourier expansion. Originally, the Fourier coefficients were to be computed on the ground and uplinked to the ST. Ground computation of $\vec{H}_{\text{NOM}}(t)$ is discussed in detail in Section 3. The current procedure of onboard computation is presented in Section 2.3.4.

Based on a parametric study performed by LMSC (Reference 2-1), the values of the desaturation period and the costate vector updating interval for the modified ME control law have been recommended to be 600 seconds and 200 seconds, respectively.

The equations used in the modified ME control law are summarized below:

$$\begin{aligned}\vec{\mu}_T &= M^T \tilde{B} \vec{P} \\ \vec{P} &= \left[\int_{t_0}^{t_f} \tilde{B} M M^T \tilde{B}^T dt \right]^{-1} \vec{H}_D \\ \vec{H}_D &= \vec{H}_{\text{NOM}}(t_f) - \vec{H}_{\text{RW}}(t_0) - \int_{t_0}^{t_f} \vec{T}_{\text{GG}} dt \\ t_f &= t_0 + 600 \text{ seconds}\end{aligned}\tag{2-38}$$

where t_0 is incremented in steps of 200 seconds and $\vec{H}_{\text{NOM}}(t)$ is the nominal RW system momentum obtained with a half-orbit desaturation period. The implementation of this modified ME control law is shown in Figure 2-4(b). It is much closer to a closed-loop process than the conventional ME law. However, the resulting RW system momentum is identical with what would have been obtained under the nominal situation if the conventional implementation of the ME law were used.

The implementation of the ME law discussed above is limited to the case of inertial attitudes. For the case of slew maneuvers, the implementation is

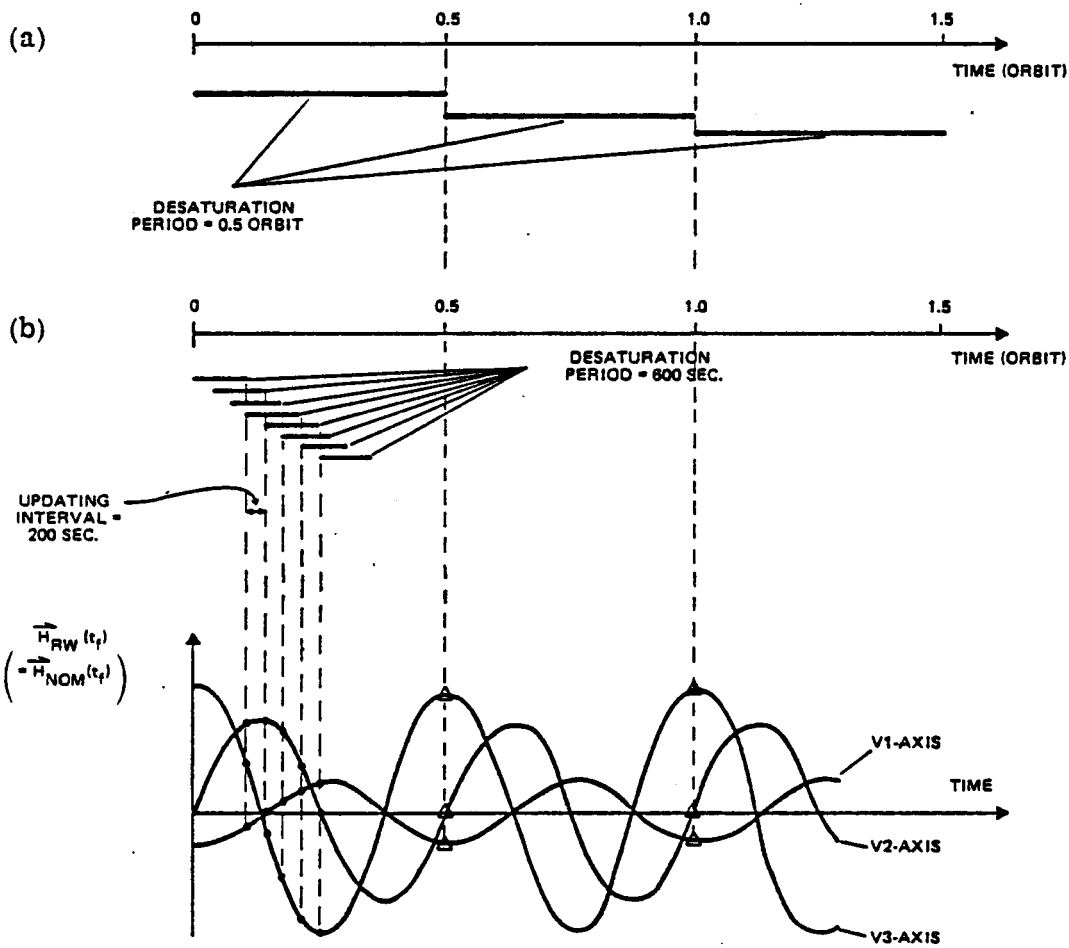
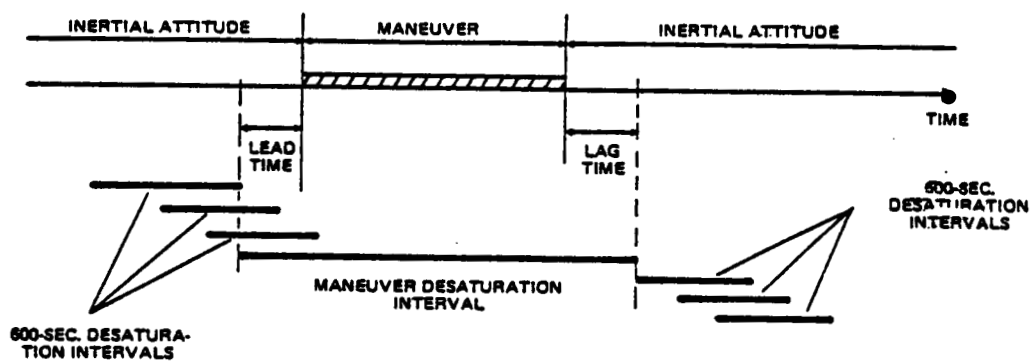


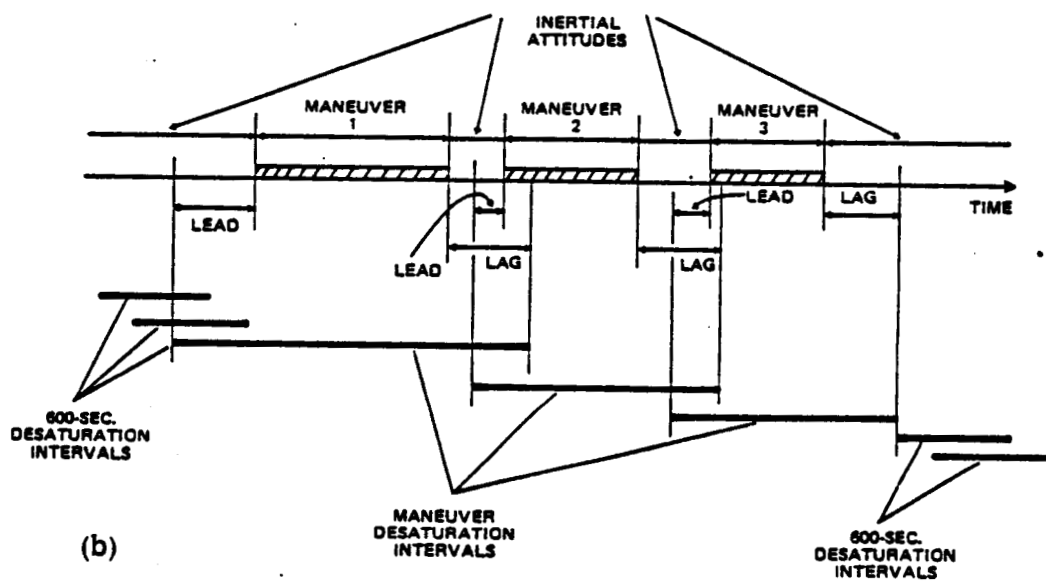
Figure 2-4. Implementation of ME Control Law
 (a) Conventional Implementation
 (b) Modified Implementation

somewhat different (Reference 2-5). A short time before the start of a slew maneuver (called the lead time), the normal mode of the ME process is interrupted and a separate maneuver desaturation interval is initiated. This maneuver desaturation interval spans the entire maneuver and ends a short time after the end of the maneuver (called the lag time). At the termination of the maneuver desaturation interval, the ME law continues with its normal mode of 600-second intervals and 200-second updates. This mechanization is schematically shown in Figure 2-5(a). When two slew maneuvers are closely spaced, the lag time at the end of one maneuver may overlap the lead time of the next maneuver. In this case, the first maneuver desaturation interval is set up in the same way as for a single maneuver, whereas the second maneuver desaturation interval starts halfway between the two maneuvers. This is schematically shown in Figure 2-5(b). When the end of one desaturation interval occurs within a maneuver, that maneuver is ignored in computing the ME law and it is assumed that the ST attitude is still that of the inertial attitude prior to the maneuver. The advantage of this technique of implementing the ME law during maneuvers is that the end of a desaturation interval never falls within a slew maneuver and therefore there is no need of computing the nominal momentum for a time-varying attitude. This significantly simplifies the nominal momentum computations because the nominal momentum can be represented by a sinusoidal function when the ST is in an inertial attitude.

The required lengths of the lead and lag times have been studied by LMSC. It was found that the minimum required lengths for worst case maneuvers do not vary much with slew angle for values above 30 degrees. They are about 500 seconds for the orbit tracks that are favorable for momentum dumping and about 900 seconds for the unfavorable orbit tracks. For slew angles below 30 degrees, the lead and lag times can be linearly decreased with slew angle. For most of the maneuvers to be executed by the ST, the minimum required lead and lag times will be shorter than that stated above. However, it was



(a)



(b)

7081/79

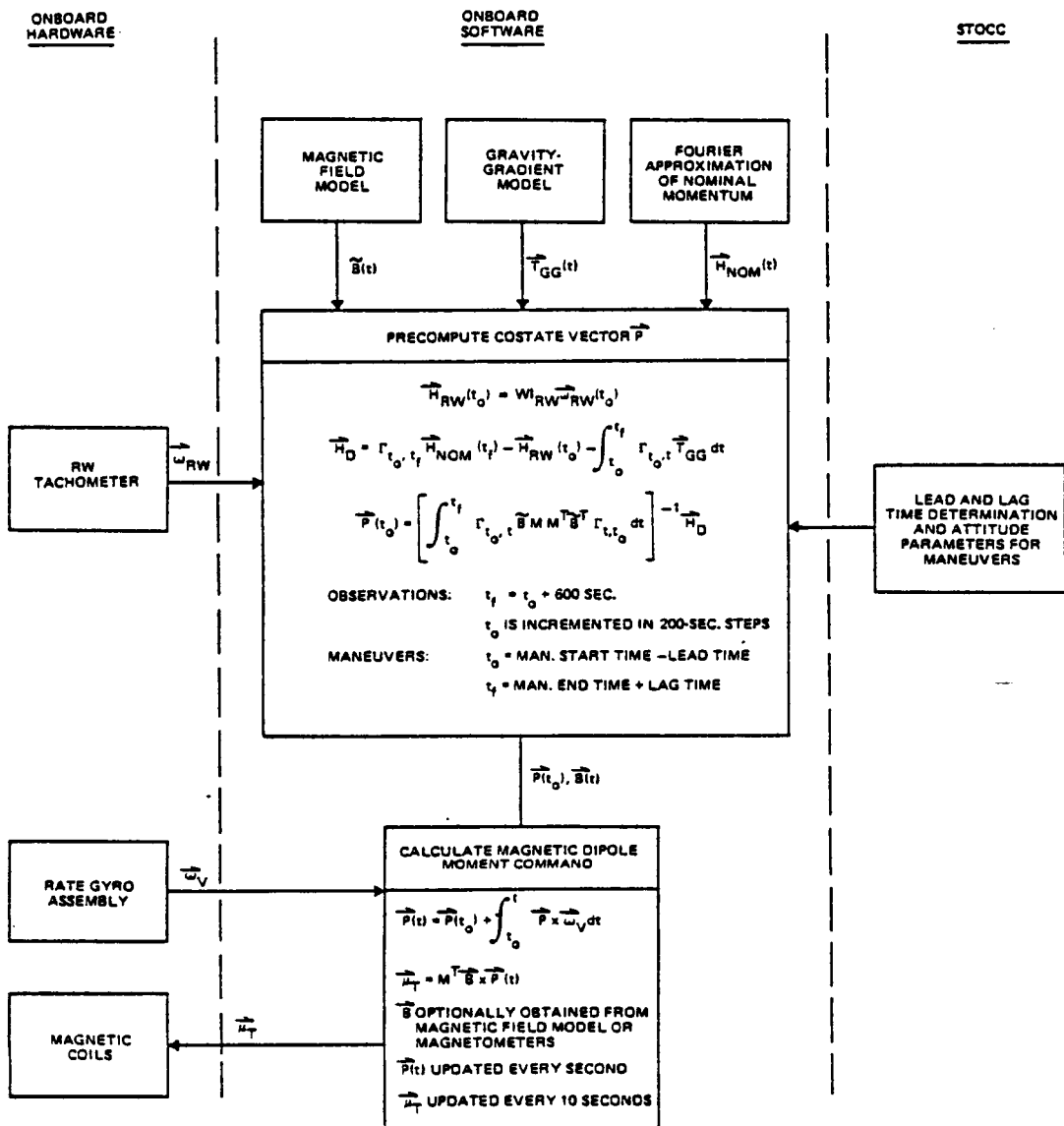
Figure 2-5. Desaturation Intervals
 (a) For a Single Maneuver
 (b) For a Series of Closely Spaced Maneuvers

found that the peak RWA speeds are not sensitive to the lengths of the lead and lag times and therefore no real benefit would result from using the minimum required lengths of the lead and lag times for each maneuver. The procedure for selecting the lead and lag times will be implemented at the STOCC and the lead and lag times will be made part of the maneuver command list.

2.3.2.2 System Baseline

Figure 2-6 is a baseline diagram of the onboard implementation of the ME desaturation law. In the figure, the coordinate transformation matrix $\Gamma_{t,t'}$, which is computed onboard by a command generator, is included in the equations to cover the cases of maneuvers. In the case of inertial attitude, $\Gamma_{t,t'}$ equals identity. The geomagnetic field model, the gravity-gradient model, and the Fourier expansion of the nominal RW system momentum must be stored onboard for the purpose of computing the costate vector \vec{P} . The RW momentum at the start of each desaturation period, $\vec{H}_{RW}(t_0)$, is obtained from the $\vec{\omega}_{RW}$ measurement sensed by the RW tachometer. During an observation, \vec{P} is computed with desaturation periods, $t_f - t_0$, of 600 seconds and updated every 200 seconds. For the case of maneuvers, \vec{P} is computed for a desaturation interval from maneuver start time minus lead time to maneuver end time plus lag time with no updates. The lead and lag times of each maneuver are predetermined by the STOCC and sent to the ST as part of the maneuver commands.

After \vec{P} is computed, the magnetic dipole moment command $\vec{\mu}_T$ is then calculated using the sensed or calculated magnetic field and sent to the magnetic coils to generate the desired magnetic torque. The updating frequency of $\vec{\mu}_T$ is every 10 seconds. For the case of maneuvers, the inertially fixed \vec{P} must be transformed to the instantaneous body coordinates before $\vec{\mu}_T$ is computed. This coordinate transformation is performed by using the vehicle angular velocity measured by the rate gyro assembly.



7081/79

Figure 2-6. Baseline Diagrams of Onboard ME Law Implementation

2.3.3 Required Support by the Ground System

Ground support required for implementation of the ME control law has been reduced because (1) computation of the nominal momentum profile is now to be performed onboard ST and (2) limiting reaction wheel speeds to 10 hertz is no longer a requirement of ST momentum management. The requirements discussed in this section were necessary for support of an earlier implementation plan for the ME control law and are superseded by those reviewed in Section 2.3.4.

The required support by the ground system (STOCC) for the momentum management using the ME control law can be categorized into three items: (1) the computation of the Fourier coefficients for the nominal momentum profile \vec{H}_{NOM} for all the inertial attitudes covering the 24-hour period; (2) the determination of the lengths of the lead and lag times for each of the slew maneuvers; and (3) the screening of targets based on the requirement that the reaction wheel speeds have to remain below approximately 10 hertz while the ST is in the fine pointing mode.

The Fourier coefficients for the nominal momentum profile are needed because of the modification to the conventional ME law as discussed in Section 2.3.2.1. The analytical considerations necessary for this implementation are given in detail in Section 3. The determination of the lead and lag times for maneuvers is required by the way the desaturation period is defined for the maneuvers (see Section 2.3.2.1 and Figure 2-5). The screening of targets is necessary because, based on the simulation studies performed by LMSC (Reference 2-5), finite chances (~5 percent if all RWA are operational and ~15 percent when one RWA failed) exist in having the RWA speed exceed the 10-hertz limit during the lead and lag time of a maneuver.

Both the determination of the lead and lag times and the screening of targets can be achieved by implementing a simulation for the ME control law. This problem is further discussed in Section 4.

2.3.4 Revisions of Onboard Implementation and Ground Support

The ME control law is now self-contained onboard the ST in the SSM computer. (References 2-7, 2-8, and 2-9). Specifically, computation of the nominal momentum profile and its Fourier approximation are now performed onboard the ST. Figure 2-7 is a baseline diagram of this computation. The magnetic field and gravity-gradient torque are integrated over an interval of half an orbit starting at T_0 , the end of the desaturation interval that is currently being processed. The integrals are used to compute an estimated Lagrange multiplier for the half orbit, which is then used to compute the nominal momentum time history, $\vec{H}_{\text{NOM}}(t)$, the amplitude, \bar{A} , and the time of maximum, t_{MAX} , for the Fourier approximation of $\vec{H}_{\text{NOM}}(t)$. The equation

$$\left[\vec{H}_{\text{NOM}}(t) \right]_j = A_j \cos \frac{2\pi}{T} \left[t - (t_{\text{MAX}})_j \right] ; j = 1, 2, 3 \quad (2-39)$$

is used to calculate the nominal momentum at the end of each 600-second desaturation period.

Because of the revisions in the implementation of the ME control, the STOCC is no longer required to compute nominal momentum profiles and Fourier representations to be uplinked to the ST. Another requirement, screening of targets to prevent reaction wheel speeds in excess of 10 hertz, also is no longer required.

The ST is being designed now to meet its requirements regardless of reaction wheel speed (Reference 2-7). In particular, both the reaction wheel moment of inertia and the maximum available magnetic torque have been increased by more than a factor of 2. The current values are $I_{\text{RW}} = 0.83 \text{ kilogram-meters}^2$ and torquer capacity = $4000 \text{ ampere-meters}^2$ (Reference 2-10). LMSC has made vibration measurements on the reaction wheel engineering model and has found that the most significant source of vibration is not wheel imbalance, which occurs at wheel speed, but other phenomena that have frequency components at

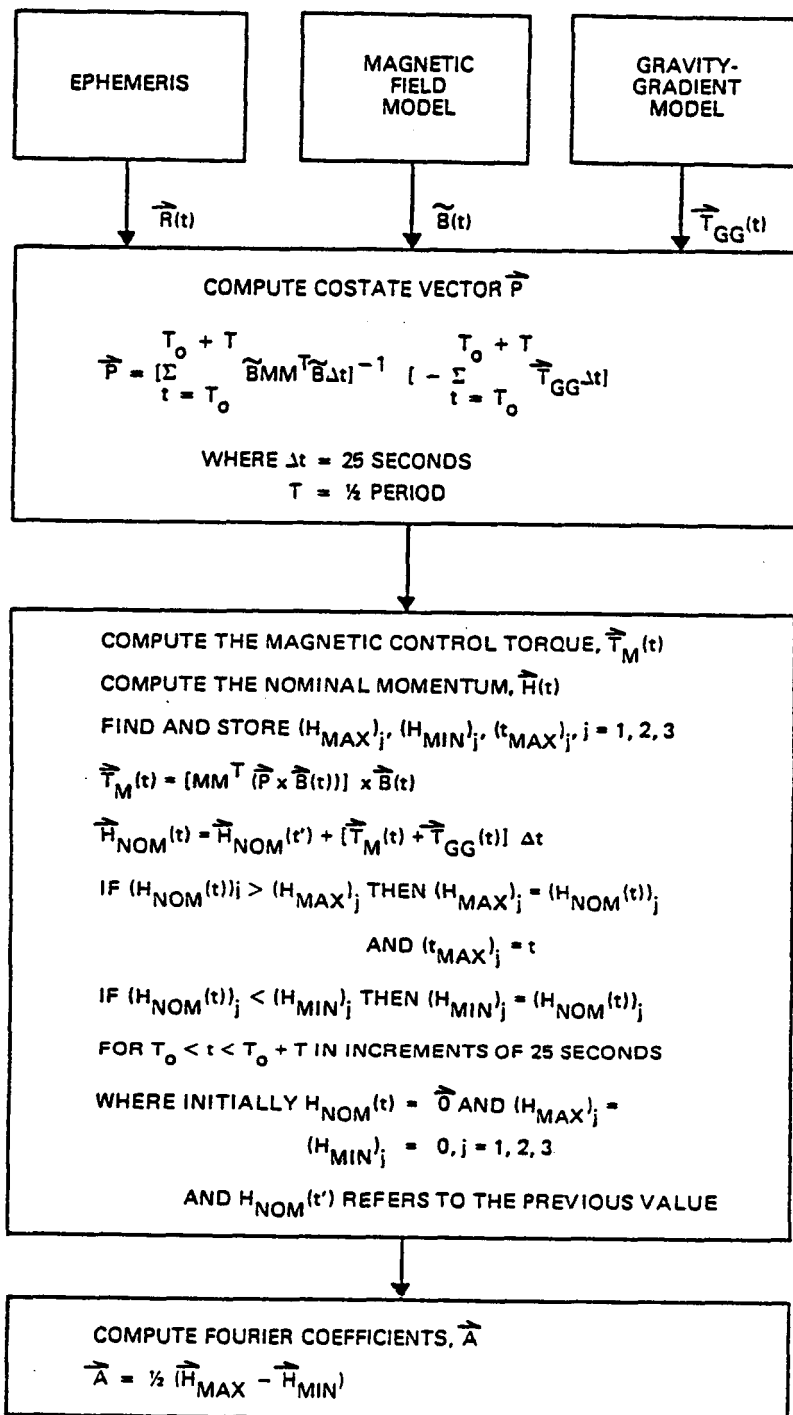


Figure 2-7. Baseline Diagram of Onboard Calculation of Fourier Approximation of Nominal Momentum

multiples of wheel speed. Hence, the wheels are being designed and built so that at all speeds the levels of structural interactions are tolerable and error budgets associated with wheel vibrations are met.

For support of momentum management using the ME control law, the STOCC is currently required to provide information specifying the start and length of maneuver intervals and parameters necessary to estimate an attitude during a long maneuver. The specific parameters include the maneuver start time, t_0 ; the lead and lag times; the maneuver magnitude; the eigenvector; the jerk pulse width, δ ; the length of the acceleration-limited region of the command profile, ϵ ; and the length of the velocity-limited region of the command profile, t_r . The nominal lead/lag time is 500 seconds. For operation over the South Atlantic Anomaly, this time is increased to 1000 seconds. The STOCC must ensure that the momentum updates do not overlap in time based on the lead/lag times provided in the uplinked data load. The parameters δ , ϵ , and t_r are computed from knowledge of the maneuver and specified parameters including the maximum angular rate, maximum angular acceleration, and jerk amplitude when the maneuver is not jerk limited.

REFERENCES

- 2-1. Lockheed Missiles and Space Company, LMSC-HREC TM D 496086, Reaction Wheel Speed Minimization through Magnetic Desaturation, A. Wernli, November 1976
- 2-2. --, SE-03, Section H, "Space Telescope Project Support Systems Module, Appendix 5, Cross-product Momentum Management," April 1979
- 2-3. --, LMSC 4171856A, Space Telescope Flight Software Requirements, R. H. Jones, W. F. Wright, W. H. Whittier, October 1979
- 2-4. --, LMSC 4172682, ST PCS Flight Software Algorithms, R. H. Jones, W. F. Wright, W. H. Whittier, October 1979
- 2-5. --, SE-03, Section H, "Space Telescope Project Support Systems Module, Appendix 6, Minimum-Energy Momentum Management," April 1979
- 2-6. J. R. Glaese, et al., "Low-Cost Space Telescope Pointing Control System," J. Spacecraft, vol. 13, no. 7, July 1976
- 2-7. EE61-109-80, letter from D. W. Justice to P. B. Davenport, April 7, 1980
- 2-8. Bendix Corporation, ST-2003 Rev. E, PCS Equations Document, K. Tompetrini, April 1980
- 2-9. Lockheed Missiles and Space Company, Minimum Energy Law Design for Momentum Management of Space Telescope PDL Document, J. Robison, June 1980
- 2-10. T. Griffin (GSFC), private communication, August 1980

SECTION 3 - ANALYTICAL CONSIDERATION FOR GROUND SUPPORT OF THE ME CONTROL LAW

As described in Section 2.3.4, computation of the nominal angular momentum profile, $\vec{H}_{\text{NOM}}(t)$, for use in the ME control law is now performed onboard the ST. This section on ground computation of $\vec{H}_{\text{NOM}}(t)$ is retained for analytical purposes.

$\vec{H}_{\text{NOM}}(t)$ is the momentum time history of a nominally operating spacecraft driven by the ME control law with a half-orbit desaturation period. The values of $\vec{H}_{\text{NOM}}(t)$ will be used onboard as the target momentum toward which the reaction wheel system momentum will be continuously driven under the modified ME control law, which has a 600-second desaturation period and a 200-second updating interval. The significance of the half-orbit desaturation period used in determining $\vec{H}_{\text{NOM}}(t)$ is to provide a sufficiently long period so that a sizable variation in the direction of the geomagnetic field will occur to make the desired momentum unloading possible and to take advantage of the half-orbit period of the cyclic gravity-gradient torque components. The much shorter desaturation period and updating interval to be used onboard will shorten the open-loop desaturation process to prevent the reaction wheel momentum from drifting to very large values in the presence of off-nominal conditions.

The manner in which momentum unloading is performed during slew maneuvers does not require a nominal momentum profile for the duration of the maneuver. The nominal momentum profile is only required for inertial attitudes.

3.1 OVERVIEW OF COMPUTATION SEQUENCE

Since the nominal momentum profile is periodic with one-half orbit, it can be approximated by a sinusoidal function of the following form:

$$\vec{H}_{\text{NOM}}(t) = \vec{a} \cos \frac{2\pi}{T} t + \vec{b} \sin \frac{2\pi}{T} t$$

where T is the half-orbit period and the components of a and b are the Fourier coefficients to be computed at the STOC and uplinked to the ST. One set of coefficients is required for each inertial attitude.

The computation sequence for the Fourier coefficients at a given inertial attitude is illustrated in Figure 3-1. In the figure, T_0 is the time at the end of the last slew maneuver, h and N are the integration step size and the number of integration steps, respectively, to be used in computing the Fourier coefficients. All other parameters are as defined in Section 2. The computational sequence can be generally divided into three major steps: (1) the computation of the costate vector \vec{P} corresponding to a half-orbit desaturation period; (2) the computation of the nominal momentum time history $\vec{H}_{\text{NOM}}(t)$; and (3) the transformation of $\vec{H}_{\text{NOM}}(t)$ to the Fourier coefficients \vec{a} and \vec{b} .

In each of the three steps, a numerical integration technique is required. The most commonly used numerical integration technique is the fourth-order Runge-Kutta method, which will be discussed in Section 3.2. The integration steps referred to in Figure 3-1 are based on this method. The accuracies of the results depend on the step sizes used. On the basis of simulations using the fourth-order Runge-Kutta method, LMSC has recommended (Reference 3-1) a step size of 600 seconds or less to achieve the 2-percent accuracy requirement on \vec{H}_{NOM} . This suggests a value of $N = 5$ for the number of integration steps defined in Figure 3-1.

Besides the integration technique, two areas have to be addressed to carry out the computations outlined in Figure 3-1: the computation of the gravitational gradient torque $\vec{T}_{\text{GG}}(t)$ and the computation of the geomagnetic field $\vec{B}(t)$, both represented in the ST body-fixed coordinate system. These are given in Sections 3.3 and 3.4, respectively.

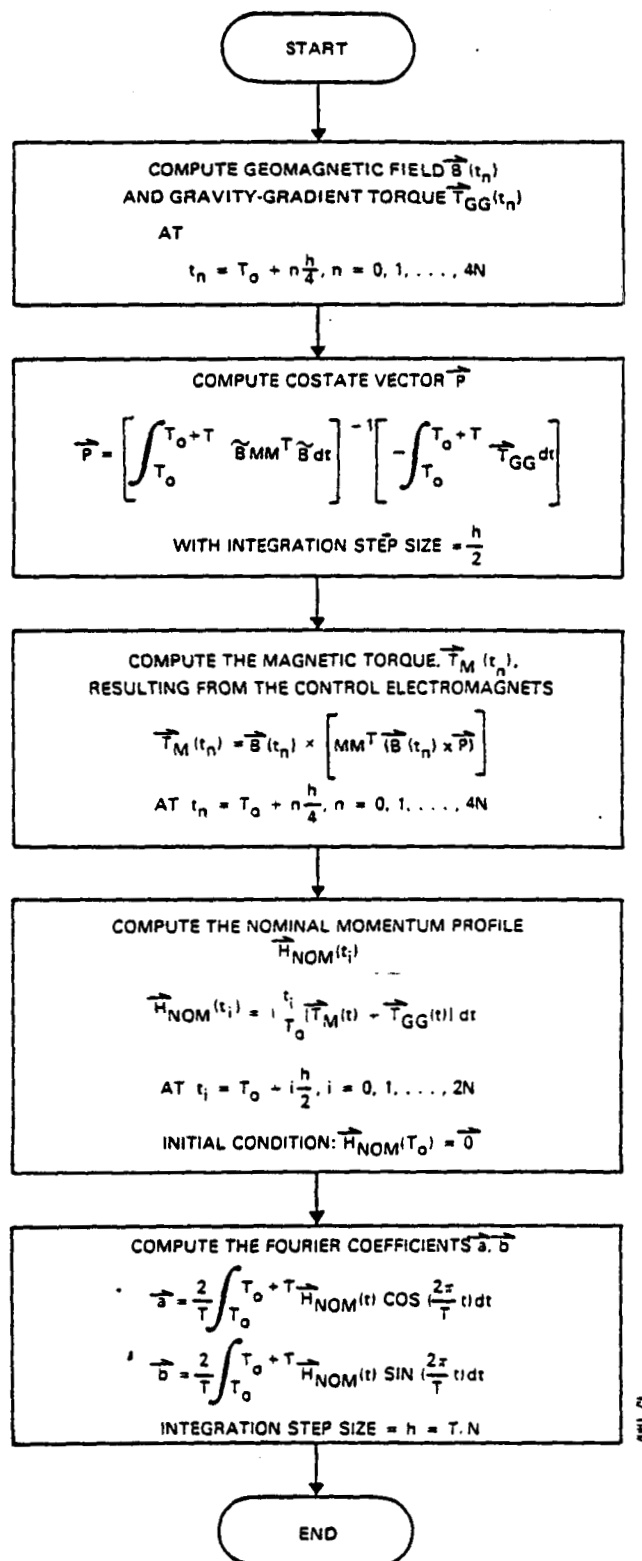


Figure 3-1. Computation Flow for the Fourier Coefficients of the Nominal Momentum Profile

3.2 NUMERICAL INTEGRATION TECHNIQUE--FOURTH-ORDER RUNGE-KUTTA METHOD

To integrate a differential equation of the form

$$\frac{dy}{dt} = f(t, y) \quad (3-1)$$

and to obtain an exact close-formed solution for y is usually difficult and most of the time impossible. Techniques to provide numerical approximations are therefore important.

Among the many techniques available in evaluating numerical integrations (e.g., Reference 3-2), the fourth-order Runge-Kutta method is most often used because of its accuracy and simplicity. Therefore, this method is recommended for use by the STOCC to generate the nominal momentum profile. The equations to be used in this method to compute function y are given below without derivations:

$$y_{n+1} = y_n + \frac{h}{6} (k_1 + 2k_2 + 2k_3 + k_4)$$

$$k_1 = f(t_n, y_n)$$

$$k_2 = f\left(t_n + \frac{h}{2}, y_n + \frac{1}{2}hk_1\right)$$

$$k_3 = f\left(t_n + \frac{h}{2}, y_n + \frac{1}{2}hk_2\right)$$

$$k_4 = f(t_n + h, y_n + hk_3)$$

(3-2)

where $t_n = t_0 + nh$, $y_n = y(t_n)$, and h is the step size of the integration.

In the case that f is independent of y , Equation (3-1) becomes

$$y(t) = \int_{t_0}^t f(\tau) d\tau \quad (3-3)$$

and Equation (3-2) reduces to Simpson's rule of numerical integration:

$$y_{n+1} = y_n + \frac{h}{6} \left[f_n + 4f_{n+h/2} + f_{n+h} \right] \quad (3-4)$$

This simplification is appropriate for each of the numerical integrations required in Figure 3-1.

With Equation (3-4), $y(t)$ can be evaluated at any time t by a proper choice of the integration step h . Notice in Equation (3-4) that for a given value of h , the function f is to be computed at both ends of the interval as well as the midpoint between the two ends. Therefore, the actual step size required in computing f is $h/2$. As shown in Figure 3-1, to obtain the Fourier coefficients \bar{a} and \bar{b} at an integration step size h , the nominal momentum time history $\vec{H}_{\text{NOM}}(t)$ must be evaluated at $h/2$ steps and this requires the computation of \vec{T}_M , \vec{T}_{GG} , and \vec{B} at $h/4$ steps.

3.3 COMPUTATION OF GRAVITY-GRADIENT TORQUES

The gravity-gradient torque for computing the nominal momentum profile (Reference 3-1) is given by

$$\vec{T}_{\text{GG}} = 3\Omega_o^2 \left[\hat{R}_V \times (I\hat{R}_V) \right] \quad (3-5)$$

where Ω_o = spacecraft angular rate

$= \pi/T$, where T = half-orbit period

I = ST inertia matrix

$$\begin{aligned}\hat{R}_V &= \text{unit ST position vector in spacecraft body-fixed coordinate system} \\ &\quad \text{(V-frame)} \\ &= [VE] \hat{R}_E\end{aligned}\tag{3-6}$$

$$\hat{R}_E = \text{unit ST position vector in equatorial inertial coordinates (E-frame)}$$

$$[VE] = \text{coordinate transformation matrix from the E-frame to the V-frame}$$

$$= \begin{bmatrix} (q_1^2 - q_2^2 - q_3^2 + q_4^2) & 2(q_1q_2 + q_3q_4) & 2(q_1q_3 - q_2q_4) \\ 2(q_1q_2 - q_3q_4) & (-q_1^2 + q_2^2 - q_3^2 + q_4^2) & 2(q_3q_4 + q_1q_4) \\ 2(q_1q_3 + q_2q_4) & 2(q_2q_3 - q_1q_4) & (-q_1^2 - q_2^2 + q_3^2 + q_4^2) \end{bmatrix}\tag{3-7}$$

In Equation (3-7), q_1 , q_2 , q_3 , and q_4 are the components of the inertial reference quaternion \vec{q} .

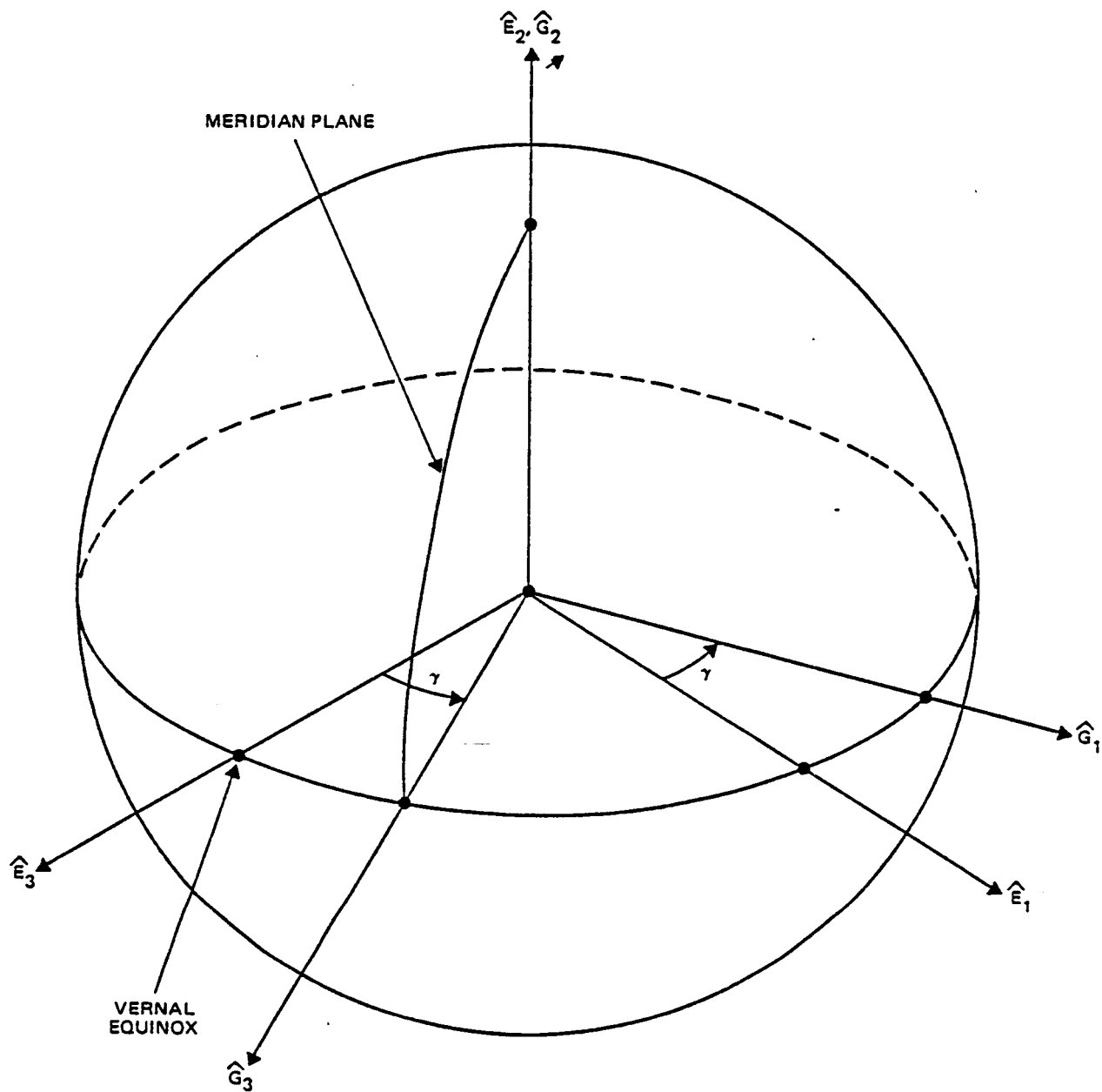
3.4 CALCULATION OF GEOMAGNETIC FIELD

The geomagnetic field to be computed by the ST OCC can be modeled either by spherical harmonic expansions or by magnetic dipoles. The equations necessary for both models are presented in this subsection. A more complete discussion of the spherical harmonic expansion model can be found in Reference 3-3 and that of the magnetic dipole model, which is the model to be used onboard the ST, is given in References 3-1 and 3-4.

3.4.1 Spherical Harmonic Model

The geomagnetic field in the spacecraft body coordinate \vec{B} can be obtained through the following transformation:

$$\vec{B} = [VE] [GE]^T \vec{B}_G\tag{3-8}$$



E-FRAME: EQUATORIAL INERTIAL COORDINATE
 G-FRAME: EQUATORIAL EARTH-FIXED COORDINATE

Figure 3-2. Coordinate System Definitions

where [VE] = transformation matrix from the equatorial inertial coordinate to the body-fixed coordinate as given by Equation (3-7)

[GE] = transformation matrix from the E-frame to the Earth-fixed coordinate system (G-frame) (see Figure 3-2)

$$= \begin{bmatrix} \cos \gamma & 0 & -\sin \gamma \\ 0 & 1 & 0 \\ \sin \gamma & 0 & \cos \gamma \end{bmatrix} \quad (3-9)$$

$$\gamma = \gamma_0 + \Omega_E t$$

γ_0 = angle from vernal equinox to prime meridian at time $t = 0$

Ω_E = Earth rotation rate

B_G = geomagnetic field vector expressed in G-frame

The magnetic field vector \vec{B}_G can be expressed in terms of spherical harmonics by the following:

$$\begin{aligned} B_r &= \sum_{n=1}^k \left(\frac{a}{r} \right)^{n+2} (n+1) \sum_{m=0}^n (g^{n,m} \cos m\phi + h^{n,m} \sin m\phi) P^{n,m}(\theta) \\ B_\theta &= - \sum_{n=1}^k \left(\frac{a}{r} \right)^{n+2} \sum_{m=0}^n (g^{n,m} \cos m\phi + h^{n,m} \sin m\phi) \frac{\partial P^{n,m}(\theta)}{\partial \theta} \quad (3-10) \\ B_\phi &= \frac{-1}{\sin \theta} \sum_{n=1}^k \left(\frac{a}{r} \right)^{n+2} \sum_{m=0}^n m (-g^{n,m} \sin m\phi + h^{n,m} \cos m\phi) P^{n,m}(\theta) \end{aligned}$$

Here, B_r , B_θ , and B_ϕ are the radial (outward positive), coelevation (South positive), and azimuth (East positive) components of B_G , respectively. a is the equatorial radius of the Earth. r , θ , and ϕ are the geocentric distance, coelevation, and East longitude from Greenwich of the spacecraft position. $P^{n,m}$ are the Gauss-normalized associated Legendre polynomials, which can be obtained from the following recursion relations:

$$\begin{aligned}
 P^{0,0} &= 1 \\
 P^{n,n} &= \sin \theta P^{n-1, n-1} \\
 P^{n,m} &= \cos \theta P^{n-1, m} - K^{n,m} P^{n-2, m} \\
 K^{n,m} &\equiv \frac{(n-1)^2 - m^2}{(2n-1)(2n-3)}, \quad n > 1 \\
 K^{n,m} &\equiv 0, \quad n = 1
 \end{aligned} \tag{3-11}$$

The recursion relations for the partial derivatives of $P^{n,m}$ are given by

$$\begin{aligned}
 \frac{\partial P^{0,0}}{\partial \theta} &= 0 \\
 \frac{\partial P^{n,n}}{\partial \theta} &= (\sin \theta) \frac{\partial P^{n-1, n-1}}{\partial \theta} + (\cos \theta) P^{n-1, n-1} \\
 \frac{\partial P^{n,m}}{\partial \theta} &= (\cos \theta) \frac{\partial P^{n-1, m}}{\partial \theta} - (\sin \theta) P^{n-1, m} \\
 &\quad - K^{n,m} \frac{\partial P^{n-2, m}}{\partial \theta}
 \end{aligned} \tag{3-12}$$

To reduce the computation time, the following recursion relations should be used for $\cos m\phi$ and $\sin m\phi$:

$$\begin{aligned}\cos m\phi &= \cos [(m-1)\phi] \cos\phi - \sin\phi \sin [(m-1)\phi] \\ \sin m\phi &= \sin [(m-1)\phi] \cos\phi + \sin\phi \cos [(m-1)\phi]\end{aligned}\quad (3-13)$$

The constants $g^{n,m}$ and $h^{n,m}$ in Equation (3-10) are related to the Gaussian coefficients g_n^m and h_n^m by the following relations:

$$\begin{aligned}g^{n,m} &\equiv S_{n,m} g_n^m \\ h^{n,m} &\equiv S_{n,m} h_n^m\end{aligned}\quad (3-14)$$

where $S_{n,m}$ can be calculated from the following recursion relations:

$$\begin{aligned}S_{0,0} &= 1 \\ S_{n,0} &= S_{n-1,0} \left[\frac{2n-1}{n} \right], \quad n \geq 1 \\ S_{n,m} &= S_{n,m-1} \sqrt{\frac{(n-m+1)(\delta_m^1 + 1)}{n+m}}, \quad m \geq 1\end{aligned}\quad (3-15)$$

In Equation (3-15), δ_m^1 is the Kronecker delta defined as $\delta_j^i = 1$ if $i = j$ and 0 otherwise.

The Gaussian coefficients g_n^m and h_n^m are determined empirically by a least-squares fit to measurements of the field. The coefficients for the International Geomagnetic Reference Field (IGRF) for epoch 1975 are given in Reference 3-3.

3.4.2 Magnetic Dipole Model

The magnetic dipole model used onboard the ST represents the geomagnetic field in the Earth-fixed coordinate frame, \vec{B}_G , by six magnetic dipoles. That is,

$$\vec{B}_G = \sum_{i=1}^6 \frac{1}{|\vec{R}_i|^3} \left\{ -\vec{E}_{mi} + \frac{3}{|\vec{R}_i|^2} (\vec{R}_i \cdot \vec{E}_{mi}) \vec{R}_i \right\} \quad (3-16)$$

where $\vec{R}_i = \vec{R}_G - \vec{R}_{oi}$
 $\vec{R}_G = [GE] RE$
 \vec{R}_E = ST position vector in equatorial inertial coordinates
 \vec{R}_{oi} = position vector of the i th dipole
 \vec{E}_{mi} = dipole moment vectors of the i th dipole

In Equation (3-16), \vec{R}_E is obtained from the spacecraft ephemeris computation. $[GE]$ is the transformation matrix given in Equation (3-9), and \vec{R}_{oi} and \vec{E}_{mi} were determined by LMSC (Reference 3-4) to minimize the root-mean-square (rms) error in the magnetic field. It was concluded (Reference 3-1) that with this modeling, no update of the dipole data is necessary within the 15-year lifetime of the ST.

After \vec{B}_G is obtained from Equation (3-16), the geomagnetic field in the ST body-fixed coordinate can be computed using Equation (3-8).

REFERENCES

- 3-1. Lockheed Missiles and Space Company, SE EM No. PCS-205, Momentum Management Computations Performed by STOCC, A. Wernli, July 1978
- 3-2. F. B. Hildebrand, Introduction to Numerical Analysis. New York: McGraw-Hill, Inc., 1956
- 3-3. Michael Plett, "Magnetic Field Models," Spacecraft Attitude Determination and Control. Dordrecht, Holland: D. Reidel, 1978
- 3-4. Lockheed Missiles and Space Company, PCS-102, Onboard Implementation of the Space Telescope Momentum Management System, A. Wernli, January 1978

SECTION 4 - OPERATIONAL IMPACT OF ONBOARD CONTROL LAWS

Onboard computation of nominal momentum profiles and elimination of reaction wheel speed limits (Section 2.3.4) have significantly reduced the operational impact of onboard control laws. Section 4.1 reviews early studies that evaluated control law performance in terms of whether the 10-hertz reaction wheel speed limit was exceeded. The 10-hertz speed limit is no longer a requirement. Furthermore, the reaction wheel moment of inertia has been increased from 0.382 to 0.83 kilogram-meters² and the wheel speeds reported in Section 4.1 should be reduced by the ratio $.382/.83 = 0.46$. Sections 4.2 through 4.4 discuss the impact of momentum management procedures on routine operations and scientific programs and also estimate required resources. Ground calculations of nominal momentum profiles and computer simulations are no longer needed for operational support; however, such software may be required for diagnostic purposes. New analytical software is described in Section 7.

4.1 APPLICABILITY OF THE CP AND ME CONTROL LAWS

The primary requirement of the momentum management control law is to maintain speeds of the reaction wheels below 10 hertz (References 4-1, 4-2, and 4-3). The performance of three control laws, including both the CP and ME laws, has been evaluated for various inertially fixed attitudes in a series of 24-hour simulations (Reference 4-2). In another study (Reference 4-4), the ME control law was evaluated during simulated slew maneuvers. A comparison of the ME law and the modified CP law during maneuvers is given in Reference 4-5. The results of these studies are summarized below.

In the first investigation, gravity-gradient torques were calculated assuming that the ST maintained an inertially fixed attitude. Nominal ST orbital elements and a simple dipole model of the geomagnetic field were used. Table 4-1 lists peak wheel speeds for the "worst case" condition, i. e., the V1-axis pointing 45 degrees out of the orbit plane.¹ These data were obtained with a magnetic dipole moment limit of 1800 ampere-meters² (A-m²) per coil. For the ME simulations, a desaturation period of 600 seconds and an update period of 200 seconds were used.

In the second investigation, slew maneuvers were simulated to evaluate the performance of the ME law. Slew rates of 0.15 degree per second were assumed. For each maneuver a single desaturation period, consisting of a lead time, the maneuver, and a lag time, was employed. Conclusions were reached about two functions: the minimum lead and lag time required to achieve the desired angular momentum and peak reaction wheel speeds during the lead and lag times.

¹These data do not necessarily represent the worst cases. Increases in reaction wheel speed of up to 20 percent were noted for smaller angles.

Table 4-1. Comparison of Peak Reaction Wheel Speeds for
the CP and ME Control Laws (Reference 4-2)

<u>Control Law</u>	<u>Peak Reaction Wheel Speed (Hz)</u>	
	<u>CP</u>	<u>ME</u>
Normal Operation	10.3	7.8
Detected Coil Failure	11	8.6
Undetected Coil Failure	14.8	10.3
Undetected Tachometer Failure	27	21
Detected RW Failure	18	13.5
Undetected RW Failure	11	13.5

It was found that the minimum required lead and lag times vary from zero to some maximum value depending on the initial attitude and the direction of the slew. The maximum value is nearly independent of the size of the slew angle for slews larger than 30 degrees. Worst case maneuvers, i.e., those requiring the longest lead and lag times, were confined to a set of unfavorable orbital track segments within the following approximate ranges: longitudes between 150 and 300 degrees when the spacecraft latitude is decreasing or longitudes between 240 and 340 degrees when the spacecraft latitude is increasing. Table 4-2 compares the maximum lead and lag times required for favorable and unfavorable orbital track segments for different magnetic torquer conditions. Only a small percentage of the cases studied required the maximum times noted in Table 4-2.

Peak reaction wheel speeds during each lead and lag time were noted. The peak reaction wheel speed appears to be insensitive to the length of the lead and lag time, but does depend on the following parameters: the amount of angular momentum required to be dumped, \vec{H}_D ; the relative directions of \vec{H}_D and the geomagnetic field as seen by the ST, \vec{B} ; and the change in \vec{B} during the maneuver. The reaction wheel speed limit of 10 hertz was exceeded in 5 percent of the maneuvers when four reaction wheels were operational and in 15 percent of the maneuvers when only three reaction wheels were operational. When all four reaction wheels were available, excessive speeds were confined to the unfavorable orbit track segments defined above; however, only a small fraction of the maneuvers in the unfavorable regions result in excessive speeds. No suitable parameters were found in Reference 4-4 for predicting which maneuvers would yield excessive reaction wheel speeds, and it was concluded that simulations were required to identify such maneuvers.

The performances of the modified CP law (Section 2.2.1) and the ME law (with and without lead and lag times) are directly compared in Reference 4-5. Each

Table 4-2. Maximum Lead and Lag Times

Orbit Track Segment	Lead and Lag Times			
	<u>2800 A-m² Mag. Dipole Limit</u>		<u>4000 A-m² Mag. Dipole Limit</u>	
	<u>4 Torquers</u>	<u>3 Torquers</u>	<u>4 Torquers</u>	<u>3 Torquers</u>
Favorable	500 sec	700 sec	350 sec	500 sec
Unfavorable	900 sec	1200 sec	700 sec	900 sec

of 14 maneuvers was simulated using each of the three laws. Slew angles varied from 30 to 180 degrees. More than half of these maneuvers were designated as "difficult" cases based on the type of maneuver and orbit track segment. The performance of the ME law without lead and lag times was generally inferior to that of the other methods and will not be discussed here.

Performance of the control laws was evaluated on the basis of two criteria: the number of cases in which the reaction wheel speeds exceeded 10 hertz outside of the maneuver period and the maximum time required to settle below the 10-hertz limit. Maneuvers were simulated both assuming that all four reaction wheels were operational and assuming that one RWA was disabled. Also, the tests were repeated with estimation errors, i.e., a mismatch between environmental and model representations of the gravity-gradient torque and geomagnetic field. (\vec{T}_{GG} was overestimated by 10 percent and \vec{B} allowed to vary up to 40 percent.) The results of the study are presented in Table 4-3.

For tests in which all the RWAs are operational, the performance of the ME law appears to be superior. ME law failures, i.e., maneuvers resulting in excessive reaction wheel speeds, were a subset of the CP law failures. In four of these cases the SAA was encountered during the maneuver. Momentum management is difficult during SAA passage because the geomagnetic field has a low magnitude and only small variations in direction. Introduction of estimation errors had a greater effect on the performance of the ME law than on that of the CP law; however, use of the ME law still resulted in fewer failures and significantly shorter times required to settle below the reaction wheel speed limit.

For tests in which only three RWAs were operational, more failures were observed for both laws and the ME law failed nearly as often as the CP law. The CP law, however, requires considerably more time to settle below the 10-hertz limit without estimation errors. The introduction of estimation errors resulted in cases where the maximum reaction wheel speed never dropped below this limit. While the ME law failed as often as the CP law under these conditions, the

Table 4-3. Performance of the Modified CP Law and the ME Law
With Lead and Lag Times for 14 Identical Maneuvers

Conditions	Number of Cases Exceeding 10-hertz Reaction Wheel Speed		Maximum Time Required to Settle Below 10-hertz Reaction Wheel Speed (seconds)	
	<u>CP</u>	<u>ME</u>	<u>CP</u>	<u>ME</u>
Four RWAs Operational				
No Estimation Errors	6	3	2500	1300
With Estimation Errors	6	5	2500	1450
Three RWAs Operational				
No Estimation Errors	9	7 ^a	5600	1400
With Estimation Errors	9	9	^a b	^a b

^a This includes cases where the 10-hertz limit was exceeded during lead time.

^b A steady-state condition of reaction wheel speed greater than 10-hertz was obtained.

CP law resulted in higher maximum reaction wheel speeds. During the maneuver, the maximum speed exceeded 50 hertz in three CP law cases and two ME law cases. Because 50 hertz is the maximum speed that a reaction wheel can achieve and still produce maximum torque output, these maneuvers are unattainable.

Tentative conclusions may be drawn from the results of the three studies reviewed above. They include the following:

- For inertially fixed attitudes, both the CP and ME laws appear to be adequate for maintaining reaction wheel speeds below the 10-hertz limit during normal operation. Both laws fail or are only marginally successful in various cases of onboard hardware failure. In all but one case the ME control law is superior.
- Both laws result in excessive wheel speeds following certain difficult maneuvers. (The ME law can also fail in the lead time before a maneuver.) The ME law fails in approximately 5 percent of maneuvers during normal operation and 10 percent of maneuvers with a reaction wheel failure. The CP law fails more frequently. Difficult maneuvers occur in a limited range of orbit track segments; however, many maneuvers in these ranges are satisfactory. At present, the only method known to distinguish the difficult maneuvers is computer simulation of the maneuvers.
- Difficult maneuvers require settling times of up to 1400 seconds for the ME law and 5600 seconds for the CP law with onboard hardware failure; if estimation errors are included in the simulation, steady-state reaction wheel speeds greater than 10 hertz sometimes result for both laws. Under extreme conditions, some maneuvers are impossible because reaction wheel speeds in excess of 50 hertz are reached.

In general, the performance of the ME law is superior. If the CP law were implemented onboard the ST, the ME law (or an equivalent technique) would still be required for some worst case targets, difficult maneuvers, and in the event of hardware failure. It would be necessary to identify such targets and maneuvers at the STOCC prior to uplink to the ST and to inform the onboard computer as to which control law to use at each target. In a few cases the ME law is inadequate also. Such situations must be identified and avoided.

4.2 IMPACT ON ROUTINE OPERATIONS

The CP control law can be entirely implemented onboard the ST. No computation at the STOCC is required to support the CP law, except the generation of commands to disable a reaction wheel or magnetic torquing coil and to turn the control law on and off.

The ME control law requires considerably more software to support its implementation. As explained in Section 3, ME ground support hardware must generate a set of Fourier coefficients representing the nominal momentum profile for each inertial target. The Fourier coefficients are calculated by numerical integration of the magnetic and gravity-gradient torques over half an orbit in N steps where the recommended value of N is 5. The numerical integration requires the calculation of \vec{T}_M , \vec{T}_{GG} , and \vec{B} at $4N$ (20) points. The calculation of \vec{T}_M involves two additional numerical integrations. Computer storage and execution time required for ground support of the ME control law can be estimated from execution of the Profile program (Reference 4-6). The Profile program has been used to study momentum management for the Solar Maximum Mission (SMM). Profile calculates \vec{B} and several disturbance torques, including \vec{T}_{GG} . Execution requires 230K bytes of storage on the GSFC IBM S/360-95 computer. Calculation of all parameters for a 2-day interval in steps of 3 minutes (a total of 960 steps) requires approximately 0.4 minute of CPU time on the same computer. It is estimated that the numerical integrations required for the ST application would take no longer to perform

than the calculation of the additional disturbance torques now performed by Profile.

Therefore, it is estimated that the 20 steps required for each ST target could be performed in approximately 0.01 minute on the same computer. Processing 20 targets per day would require 0.2 minute of CPU time on the S/360-95 computer or 1 to 2 minutes in the high-speed core of the GSFC IBM S/360-65 computer. These estimates are confirmed by execution of the HNOM utility program described in Section 7.1.

Guide star selection and target sequencing by the STOCC are expected to require significantly more computational support than momentum management. For the High Energy Astronomy Observatory-2, guide star selection and target sequencing are performed by the Detailed Observing Program (DOP) (Reference 4-7). The DOP is executed in the high-speed core of the GSFC IBM S/360-65 computer and requires 10 to 20 minutes of CPU daily. Therefore, guide star selection and target sequencing are expected to require an order of magnitude more CPU time than computation of the Fourier coefficients for the nominal momentum profiles.

The lengths of the lead and lag times also must be supplied to the onboard computer (see Section 2.3.2.1). Computation of the minimum lead and lag times would require simulation of every maneuver. Alternatively, maximum times could be determined for various types of maneuvers as done in Tables 4-2 and 4-3. The type of maneuver could then be determined and lead and lag times could be assigned with negligible impact to STOCC operations. Peak reaction wheel speeds are not affected by lead and lag time lengths; however, assignment of maximum lead and lag times might require longer dwell times at targets and thus have scientific impact.

As noted in Section 4.1, the CP law fails and, less frequently, the ME law fails for some targets, maneuvers, and hardware failures. Presently, simulations are required to identify such cases. It is hoped that continued study will result

in parameterization of these events so that simulations will not be necessary for identifications. Simulation of maneuvers can be expected to have much larger computational impact than the calculation of nominal momentum profiles discussed above. Because ME failures appear to be a subset of CP failures, perhaps the ME law should be implemented for all sequences with a high probability of failure. Then only simulation of the ME law would be required to identify unfeasible sequences.

4.3 IMPACT ON SCIENTIFIC PROGRAM

The primary impact of momentum management on the ST scientific program is that some targets, maneuvers, or situations may not be feasible because of failure of the control law chosen to limit reaction wheel speeds. This subsection reviews momentum management constraints on the scheduling of normal targets as well as targets of opportunity, serendipity targets, and target branching. (See Reference 4-8 for descriptions of these special types of targets.)

For inertial pointing during normal operation, the CP law appears to be adequate for most targets and the ME law appears to be feasible for all targets. Thus, there are no areas of the celestial sphere which are inaccessible during normal operations. For various onboard hardware failures, both control laws fail for some targets and orbit track segments. If vibrations in the ST resulting from excessive reaction wheel speed fail to damp out quickly, it is possible that certain regions of the sky (perhaps bands parallel to the ST orbital plane) would be permanently unobservable by the ST.

The ME control law also fails in approximately 5 percent of normal maneuvers and in approximately 15 percent of maneuvers with only three operational RWAs. If it is necessary to avoid such maneuvers, then certain target sequences would be impossible. When combined with other restrictions because of bright object avoidance, occultations, etc., momentum management restrictions on target sequences may cause delays in completing observing programs, especially those requiring observations at specific times such as variable star studies.

Targets of opportunity are those which pertain to unpredictable, short-lived astronomical events such as novae or transient solar system phenomena. The STOCC should be able to schedule such targets within a few hours of notification of the discovery. The scheduling system should be capable of processing approximately one target of opportunity per week.

Scheduling targets of opportunity will be complicated by momentum management considerations. The STOCC must generate a new target sequence, which includes the target of opportunity, to replace the target sequence in effect. If the ME control law is implemented, lead and lag times must be determined for the new maneuvers and nominal momentum profiles must be calculated for the targets. For either control law it may be necessary to screen the new maneuvers against the control law failures discussed above. Maneuver to the target might be delayed until a favorable orbit track segment occurs. If determination of lead and lag times and screening of maneuvers require computer simulations, generation of the target sequence may be slowed, causing additional scheduling delays. Because of the transient nature of targets of opportunity, any delay in observation may have major scientific impact. Also, for some types of hardware failure, inertial pointing at the target may violate the reaction wheel speed limit. Such a control law failure may make observation of the event impossible.

Serendipity targets are those that happen to be available to a second scientific instrument (SI) during observation of a normal target by the primary SI. In particular, the wide field camera (WFC) frequently can be utilized while the normal observations proceed. The observer of serendipity targets has no control over attitude or exposure time. The principal constraint on serendipity mode observations is availability of power. Because serendipity targets are observed simultaneously with normal targets, momentum management procedures impose no additional constraints on their execution.

Branching refers to an option in real-time operations whereby alternative observing sequences are scheduled and the experimenter chooses between them

prior to the time of observation. One sequence of targets is uplinked to the ST and that sequence is executed unless the experimenter chooses the alternative sequence. The experimenter must make his/her choice in time to uplink the new commands before the maneuver. Both series of commands must be generated in advance. Thus, any calculations required for momentum management must be repeated for each sequence. These calculations include screening of targets and maneuvers and, for the ME control law, computation of the nominal momentum profile and determination of lead and lag times. If simulations are required, the amount of computation may limit the use of the branching technique.

4.4 ESTIMATION OF REQUIRED RESOURCES

Required ground support for implementation of the ME control law includes generation of the nominal momentum profile and lengths of the lead and lag times. Screening of targets and maneuvers appears to be necessary for the implementation of either the CP law or the ME law. Because the CP law can be implemented entirely onboard the ST, no additional software and hardware resources are required on the ground for its support.

Calculation of nominal momentum profiles would require computer resources similar to those needed to execute program Profile, which is described in Reference 4-6. Many of the Profile subprograms, which are written in FORTRAN, are standard utilities in use at GSFC.

Computer simulations may be required for the calculation of ME law lead and lag times and the screening of targets and maneuvers. A rough estimate of the resources required for such simulations may be obtained from a comparison with the High Energy Astronomy Observatory-2 (HEAO-2) Attitude Control Simulator (HACS) (Reference 4-9). HEAO-2 and ST both employ onboard computers, gyros, star trackers, and reaction wheels for attitude control. The HEAO-2 HACS simulates the operation of all onboard hardware necessary for

attitude control and generates corresponding output telemetry. Much of the code in HACS, which is written in FORTRAN, is unique to the HEAO application.

When HACS is executed on the GSFC IBM S/360-95 computer with the least time-consuming option (i.e., no star trackers and minimal output), HACS can perform 60 integration steps per CPU second. For HEAO applications, the step size is 0.32 second. Because the step size required for ST momentum management applications is unknown, no estimate of the total time requirement is possible.

Execution of HACS nominally requires 410K bytes of storage at the GSFC IBM S/360-95 computer. Reduction of the program to perform only functions of the type required for ST momentum management could significantly reduce this core requirement.

Analysis of the descriptions of Profile and HACS in References 4-6 and 4-9 indicates that development and operation of a simulator of ST momentum management may require considerably more resources than development and operation of a program to calculate only nominal momentum profiles.

New analytical software, including an ST Onboard Control Law Simulator (STOCLS), is described in Section 7.1. STOCLS is executed on the GSFC IBM S/360-95 computer and requires 135K bytes of storage. Typical execution times are 0.2 minute per orbit for the CP control law and 0.3 minute per orbit for the ME law.

REFERENCES

- 4-1. A. Wernli, "Minimization of Reaction Wheel Momentum Storage with Magnetic Torquers," J. Astronautical Sciences, vol. 26, no. 3, p. 257, July-September 1978
- 4-2. Lockheed Missiles and Space Company, LMSC-HREC TM D496086, Reaction Wheel Speed Minimization through Magnetic Desaturation, A. Wernli, November 1976
- 4-3. --, SE-03, Section H, Space Telescope Project, Support Systems Module, Appendix 3, April 1979
- 4-4. --, SE EM No. PCS-105A, Momentum Management with ME Law during Slew Maneuvers, A. Wernli, August 1978
- 4-5. Bendix Corporation, ST-2044 Rev A, Comparison Study of the Minimum Energy and Cross-Product Momentum Desaturation Laws, A. K. Nakashima, November 1978
- 4-6. Computer Sciences Corporation, CSC/SD-79/6080, Solar Maximum Mission (SMM) Truth Model Attitude Simulator Algorithm Description and Operating Guide, F. E. Baginski et al., June 1979
- 4-7. --, CSC/TM-79/6125, Program Overview and Functional Description of High Energy Astronomy Observatory Satellite-2 (HEAO-2) Detailed Observing Program (DOP) Target Sequencer, A. N. Suri, October 1979
- 4-8. Lockheed Missiles and Space Company, LMSC 4171847A, ST Mission Operations Requirements, DR OP-01, volume III, August 1979
- 4-9. Computer Sciences Corporation, CSC/TM-78/6115, High Energy Astronomy Observatory-B (HEAO-B) Attitude Control Simulator (HACS) User's Guide, C. R. Sturch, July 1978

SECTION 5 - PHYSICAL INTERPRETATION OF CONTROL LAWS AND ALTERNATIVE TECHNIQUES

5.1 INTRODUCTION

The purpose of this section is to provide physical interpretation of the control laws to better understand and compare their performance, to help improve the current techniques, and to develop new techniques. In general, a desaturation control law is a method of reducing the build-up of spacecraft momentum due to external environmental torques by generating a magnetic torque resulting from the interaction between the geomagnetic field and the commanded magnetic torquers situated on the spacecraft.

Each control law can in general be put into one of two main categories, depending on its type of control--closed loop or open loop. In a closed-loop control law, the magnetic dipole command is updated using instantaneous measurements with the intent to achieve a desired torque at each update time. In an open-loop control law, the magnetic dipole command is updated using predicted information with the intent to achieve a desired momentum at the end of each update period. Within each control type, control laws can be further characterized by their special criteria or constraints. These criteria or constraints are independent of the control type. That is, every control law can be either closed loop or open loop regardless of which quantity is minimized or which constraint is undertaken. Thus, to specify a control law clearly, it is necessary to specify not only criteria or constraints but also the control type.

In principle, a "minimum energy" law can be either a closed-loop law or an open-loop law depending on how the magnetic dipole command is generated. The traditional way of using "CP law" to represent a closed-loop law and "ME

law" to represent an open-loop law is confusing from a physical point of view. Open-loop laws, for example, can be derived based on simplicity. Either the magnetic moment or the torquer commands could be held constant during the desaturation intervals to produce the same end momentum conditions as an open-loop minimum energy law which keeps the direction of the desired torque constant. Actually, the ME law implemented for ST is an open-loop control law that minimizes the total energy consumed by the magnetic torquers during the desaturation period. The CP law implemented for ST is a closed-loop control law that minimizes the magnitude of the instantaneous reaction wheel speed.

In the remainder of this section, these two ST control laws will be referred to as the "current ME law" and the "current CP law" to distinguish them from other alternative control laws that carry similar minimization criteria.

Section 5.2 describes the control laws in general. Emphasis is given to the physical interpretations of the control laws, their similarities, differences, merits, and drawbacks. Section 5.3 summarizes the current control laws implemented for ST and discusses their problem areas. Section 5.4 presents alternative techniques for both inertial targets and maneuvers based on our physical understanding of the control laws. The new techniques are believed to have some advantages over the current ST implementations and may resolve several of the problems associated with the current laws.

5.2 PHYSICAL INTERPRETATION AND GENERAL DISCUSSION

5.2.1 PHYSICAL INTERPRETATION

With some rearrangement, the current control laws can be described by a simple set of equations given in Table 5-1. In the table, all quantities are put into comparable forms to enable an easy comparison between a closed-loop and an open-loop control law and between control laws with different minimization criteria. The physical meaning of each of the quantities listed in Table 5-1 is described below.

In the table, \vec{T}_D is a desired torque, which is the torque a closed-loop control law is attempting to achieve momentarily through the interaction between the magnetic torquers and the geomagnetic field. Here \vec{H}_D , which is defined for open-loop control laws only, is the integration of a desired torque over a period of time (called the desaturation period). Physically, \vec{H}_D is the desired momentum an open-loop control law attempts to achieve over the desaturation period through the interaction between the magnetic torquers and the geomagnetic field. Thus, the fundamental difference between the open-loop and the closed-loop control laws is that the former attempts to achieve \vec{T}_D momentarily, whereas the latter attempts to achieve \vec{H}_D over a desaturation period. The determination of \vec{T}_D and \vec{H}_D is briefly discussed below. For all control laws based on Equation (2-4), \vec{T}_D is obtained by replacing \vec{T}_M with \vec{T}_D in the equation. That is,

$$\vec{T}_D = \vec{H}_T - \vec{T}_{GG} \quad (5-1)$$

where \vec{H}_T is the total system momentum that equals the reaction wheel momentum \vec{H}_{RW} at inertial attitudes. For a

Table 5-1. Summary of Equations for Current Control Laws

	CURRENT CP LAW (CLOSED-LOOP MINIMUM WHEEL SPEED LAW)	CURRENT ME LAW (OPEN-LOOP MINIMUM ENERGY LAW)
DESIRED TORQUE	\vec{T}_D	
DESIRED MOMENTUM	NOT APPLICABLE	$\vec{H}_D = \int_{t_i}^{t_f} \vec{T}_D dt$
WEIGHTING MATRIX		A
COSTATE VECTOR	$\vec{P} = (B^T A A^T B)^{-1} \vec{T}_D$	$\vec{P} = \left[\int_{t_i}^{t_f} \tilde{B}^T A A^T \tilde{B} dt \right]^{-1} \vec{H}_D$
SYSTEM MAGNETIC DIPOLE MOMENT	$\vec{\mu}_M = A A^T B \vec{P}$	$\vec{\mu}_M = A A^T B \vec{P}$
MAGNETIC TORQUE	$\vec{T}_M = \vec{\mu}_M \times \vec{B}$	
COMMANDED MAGNETIC DIPOLE MOMENT	$\vec{\mu}_T = M^T (M M^T)^{-1} \vec{\mu}_M$	

7081/80

closed-loop control law, \vec{H}_T in Equation (5-1) is usually replaced by $-K_M(\vec{H}_T + \vec{H}_B)$, where K_M is a positive constant called the magnetic gain and \vec{H}_B is a bias vector that is added to \vec{H}_T to keep the reaction wheel center speed at zero. For an open-loop control law, Equation (5-1) is integrated over the desaturation period to give the desired momentum, \vec{H}_D . That is,

$$\begin{aligned}\vec{H}_D &= \int_{t_i}^{t_f} \vec{T}_D dt \\ &= \vec{H}_T(t_f) - \vec{H}_T(t_i) - \int_{t_i}^{t_f} \vec{T}_{GG} dt\end{aligned}\tag{5-2}$$

where $\vec{H}_T(t_f)$ is the desired total momentum at the end of the desaturation period and $\vec{H}_T(t_i)$ is the measured total momentum at the start of the desaturation period. The length of the desaturation period controls the magnitude and direction of \vec{H}_D . Nominally, the desaturation period is set at half an orbital period to include the major variations in the geomagnetic field and to be compatible with the period of the gravity-gradient disturbances so that only the nonperiodic portion of the accumulated gravity-gradient momentum is dumped.

The weighting matrix A of Table 5-1 is determined by the minimization criteria. A is the magnetic coil mounting matrix, M , in the current ME law to minimize the energy consumption and is the wheel mounting matrix, W , in the current CP law to minimize the reaction wheel speed. In the following discussion, to simplify the physical interpretations, an orthogonal system with A equal to the identity matrix will be assumed.

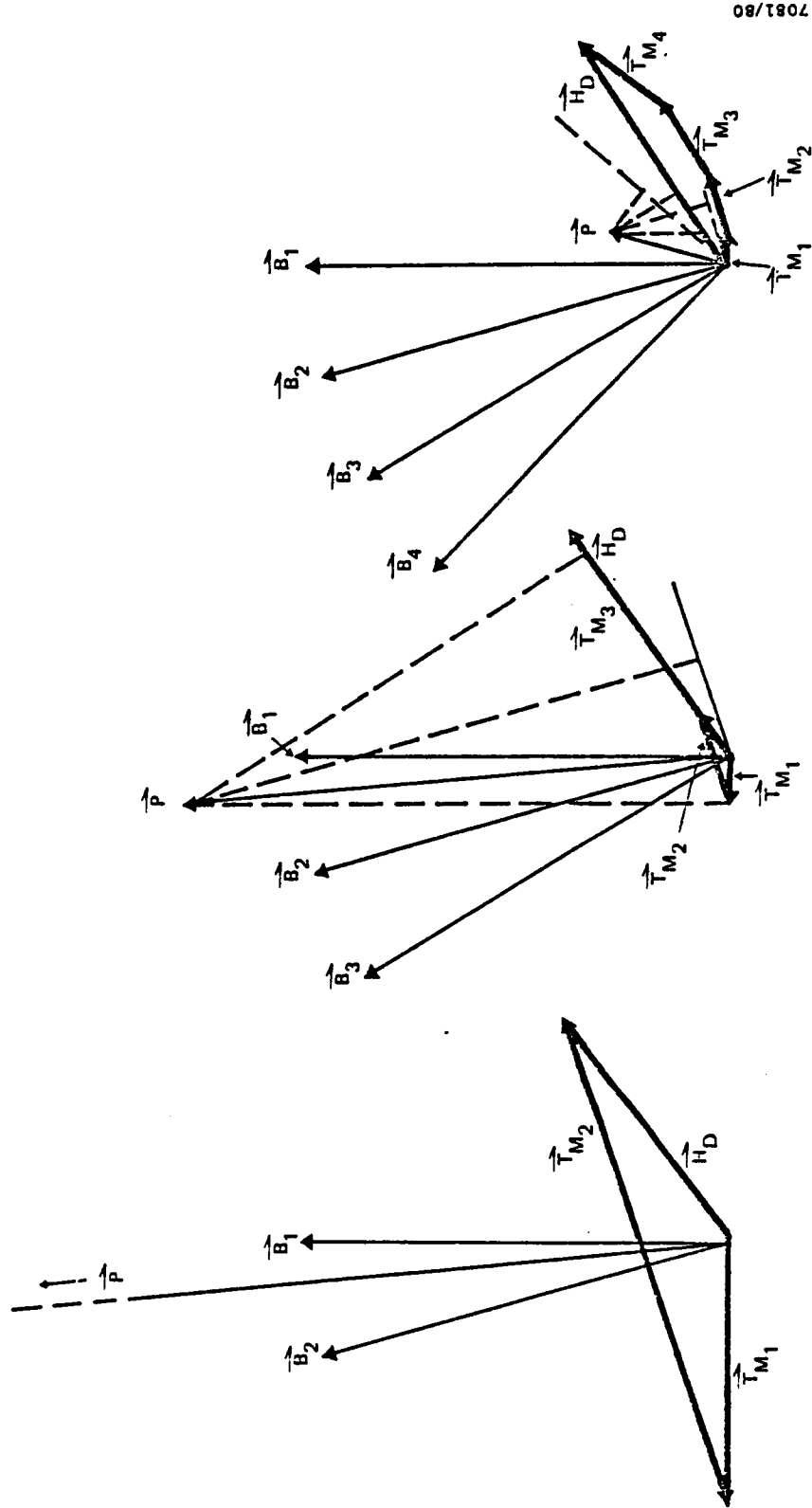
The costate vector \vec{P} is defined differently for the two control laws due to the different control types.¹ For a closed-loop control law, \vec{P} is the desired torque weighted by $|\vec{B}|^{-2}$, where \vec{B} is the geomagnetic field. For an open-loop control law, \vec{P} is the desired momentum weighted by both the magnitude and the direction of the geomagnetic field over the desaturation period. The physical meaning of \vec{P} for an open-loop control law is illustrated in Figure 5-1 with the assumption that the magnitude of \vec{B} is constant in time. As shown in Figure 5-1, \vec{P} is a fictitious torque whose component along the direction normal to the instantaneous geomagnetic field is the instantaneous magnetic torque, \vec{T}_M , generated by the torquers. The integration of \vec{T}_M over the desaturation period is equal to \vec{H}_D . The costate vector \vec{P} in an open-loop control law is analogous to the desired torque \vec{T}_D in a closed-loop control law after being properly weighted. Figure 5-1 also illustrates the significance of the desaturation period for an open-loop control law. Three cases covering different desaturation periods are shown in Figure 5-1. When the desaturation period is very short, as illustrated in Figure 5-1(a), \vec{P} approaches infinity due to the near-singular condition. In this case, the magnetic torquers are given poorly defined commands with the result that the magnetic torques generated may go through an undesirable path before the desired momentum is achieved.

¹In the derivations of the original CP and ME laws in Section 2, the costate vector, \vec{P} , was defined only for the ME law. However, an analogous definition, stated in Table 5-1, may be introduced for the CP law. Use of this definition of \vec{P} clarifies the similarities between the two laws and facilitates the physical understanding of the \vec{P} defined in the ME law.

(a) $t_1 + t_2$

(b) $t_1 + t_2 + t_3$

(c) $t_1 + t_2 + t_3 + t_4$



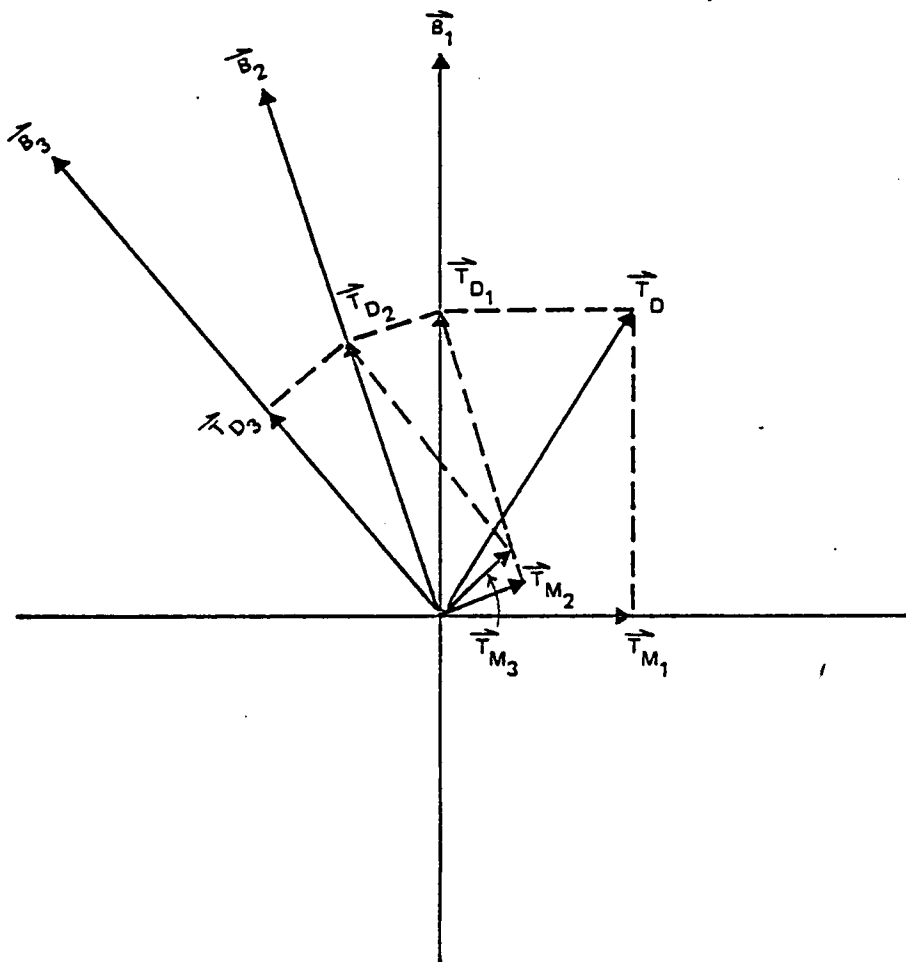
7081/80

Figure 5-1. Physical Interpretation of the Costate Vector in an Open-Loop Control Law

This is shown in Figure 5-1(a), where the magnetic torque \vec{T}_M is along a direction almost opposite to the direction of the desired momentum \vec{H}_D . This can cause a very high reaction wheel speed at the end of t_1 , which is certainly undesirable. Thus, an open-loop control law operated under very short desaturation periods can sometimes lead to serious consequences. As the desaturation period increases as shown in Figure 5-1(b) and (c), the costate vector \vec{P} becomes better defined and the path of the magnetic torques becomes closer to the desired momentum.

The system magnetic dipole moment, $\vec{\mu}_M$, is the magnetic dipole moment (defined in the spacecraft body coordinate system) that is required to generate the desired magnetic torques. The magnetic torque \vec{T}_M is the actual instantaneous magnetic torque generated from the interaction between the magnetic torquers and the geomagnetic field. The magnitude and direction of \vec{T}_M are as follows. For a closed-loop control law, \vec{T}_M is the component of \vec{T}_D which is normal to \vec{B} . This component is the best torque that can be achieved under the condition that \vec{T}_M must be perpendicular to \vec{B} , although ideally it would be desirable to generate a \vec{T}_M that equals \vec{T}_D . When the weighting matrix A is different from the identity, the magnitude and direction of \vec{T}_M differ slightly from those described above. For an open-loop control law, \vec{T}_M is also perpendicular to \vec{B} at any moment. However, \vec{T}_M also satisfies the condition that its integrated effect over the desaturation period equals the desired momentum, \vec{H}_D . That is, \vec{T}_M satisfies the condition that

$$\int_{t_i}^{t_f} \vec{T}_M dt = \vec{H}_D \quad (5-3)$$



7081/80

Figure 5-2. Geometrical Variations of the Desired Torque for a Closed-Loop Control Law

This indicates that although the desired torques cannot always be generated momentarily, the desired momentum can usually be generated over a period of time, taking advantage of the variations in the geomagnetic field. This forms one major advantage of an open-loop control law over the closed-loop control law.

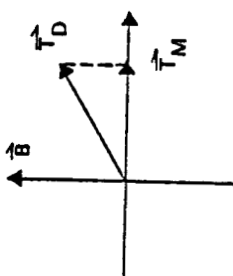
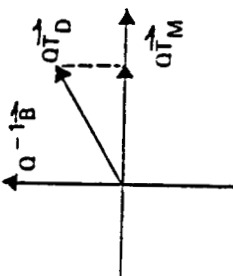
The last item in Table 5-1 is the commanded magnetic dipole moment $\vec{\mu}_T$. The components of $\vec{\mu}_T$ give the actual dipole moment required by each of the magnetic torquers to generate the magnetic torque \vec{T}_M , and $\vec{\mu}_T$ is the final output of a control law sent to the magnetic torquers.

The weighting matrix A defined in Table 5-1 is controlled by the minimization criteria of the control laws. The simplest control law minimizes the deviation between \vec{T}_D and \vec{T}_M in the body coordinates (MTD). The current CP law provides minimization of reaction wheel speeds (MWS) through use of reaction wheel mounting matrix W. The physical interpretations of \vec{T}_M for these two laws are compared in Table 5-2.

5.2.2 COMPARISONS AND MODIFICATIONS

Both the closed-loop and the open-loop control laws have their merits and drawbacks. The greatest problem of a closed-loop law is that it attempts to achieve a desired torque momentarily, which is for all practical purposes impossible. As a result, it produces a magnetic torque that is the component of \vec{T}_D normal to the geomagnetic field, which may be a small fraction of the total. This process also effectively projects the resultant torque into the direction of the geomagnetic field, which is an unfavorable direction for further reduction of the momentum. This situation is illustrated in Figure 5-2. Apparently a great deal of energy is wasted in changing the direction rather than reducing the magnitude of the momentum. Furthermore, the

Table 5-2. Physical Interpretation of \vec{T}_M for Different Minimization Criteria

MINIMIZATION CRITERION	WEIGHTING MATRIX A	PHYSICAL INTERPRETATION OF \vec{T}_M
MINIMUM TORQUE DEVIATION (MTD)	$A = I$	 <p>\vec{T}_M = THE COMPONENT OF \vec{T}_D NORMAL TO \vec{B}</p>
MINIMUM WHEEL SPEED (MWS)	$A = W = \begin{bmatrix} a & -a & a & -a \\ -b & -b & b & b \\ -b & -b & -b & -b \end{bmatrix}$ WHERE $a = \sin 20^\circ$ $b = \frac{1}{\sqrt{2}} \cos 20^\circ$	 <p>$\vec{Q T}_M$ = THE COMPONENT OF $\vec{Q T}_D$ NORMAL TO $\vec{Q}^{-1} \vec{B}$</p> <p>WHERE</p> $Q^2 = \begin{bmatrix} \frac{b^2}{a^2} & 0 & 0 \\ 0 & 1 & 0 \\ 0 & 0 & 1 \end{bmatrix} = 4b^2 (WW^T)^{-1}$

7081/80

closed-loop control law attempts to always reduce the same fraction of the total momentum as controlled by the magnetic gain K_M , regardless of the variation in geometry. This is not efficient, because the law should attempt to dump more momentum when the geometry is favorable and less momentum at an unfavorable geometry. In addition, the closed-loop control laws attempt to dump both the periodic and the nonperiodic gravity-gradient momenta, while only the nonperiodic portion needs to be dumped in many applications. These problems associated with the closed-loop control laws are eliminated in the open-loop control laws, because the open-loop control laws look at the situation ahead of time to take advantage of the variations in geometry to dump the proper amount of momentum at the proper time. Thus, at the end of the desaturation period, the desired amount of momentum will be generated from the torquers.

The open-loop control laws are ideal if actual performance is exactly as predicted. However, in case of modeling errors or undetected failure conditions, reality can be very different from the prediction. This difference will not be known until the end of the desaturation period, which may be too late for correction. To resolve this potential problem, a "modified open-loop control law" was suggested for ST that uses the half-orbit desaturation period to compute the nominal momentum profile \vec{H}_{NOM} (refer to Section 3) and then uses \vec{H}_{NOM} as the targeting momentum, $\vec{H}_T(t_f)$ of Equation (5-2), in computing \vec{H}_D when a much shorter desaturation period is used. With this modification, the advantages of the open-loop control laws are kept by forcing the system momentum to follow the same time variation it would follow if a half-orbit desaturation period were used under nominal situations. At the same time, the disadvantage of the open-loop control laws is reduced by decreasing the duration

of the desaturation period and increasing the updating frequency so that the actual system momentum can be measured at a much higher frequency, and the deviation between the reality and the prediction can be included in \vec{H}_D and corrected for at this new frequency.

In principle, with a precomputed \vec{H}_{NOM} , the shorter the update period the better, if undetected failure conditions exist. However, as discussed in Section 5.2.1, making the desaturation period of an open-loop control law arbitrarily short may cause the costate vector \vec{P} to be ill defined and result in very undesirable momentum before the desired momentum is achieved. For this reason, a 600-second desaturation period with a 200-second updating frequency was recommended in the current momentum management implementation for ST. However, if instead of using an open-loop control law at a reduced desaturation period, a closed-loop control law is used with the precomputed \vec{H}_{NOM} , the problem of determining \vec{P} will no longer exist. In this "mixed-mode control law," the updating frequency of commanding the magnetic torquers can be reduced to the frequency of the closed-loop control laws, which is approximately 50 seconds for ST. The fundamental concept of a mixed-mode law is to generate an instantaneous desired torque as in a closed-loop law, but to derive this torque from the expected momentum profile of an open-loop law. An approximation of Equation (5-1), which is a basic relationship of the current laws, can be used to generate such a desired torque, i.e.,

$$\vec{T}_D = \frac{1}{\Delta t} [\vec{H}_{NOM}(t + \Delta t) - \vec{H}_T(t)] - \vec{T}_{GG}(t) \quad (5-4)$$

where Δt is a small time interval¹ during which \vec{T}_{GG} does not change significantly and \vec{H}_{NOM} is the nominal momentum profile computed previously based upon an open-loop control law with a half-orbit desaturation period. The desired torque so determined is always nearly perpendicular to the instantaneous geomagnetic field because \vec{H}_{NOM} is computed from the nominal magnetic torques, which are momentarily perpendicular to \vec{B} . This mixed-mode control law, which is a closed-loop control law operated with an open-loop \vec{H}_{NOM} , seems to retain the advantages of both the open-loop and the closed-loop control laws and is believed to be superior to the current control laws. This mixed-mode control law is further described in Section 5.4.

Another mixed-mode law that has a simpler implementation can be derived from the original "simple cross product law," i.e.,

$$\vec{T}_D = \vec{T}_M(t) + \Delta\vec{T}(t) \quad (5-5)$$

where

$$\Delta\vec{T}(t) = K [\vec{H}_{NOM}(t) - \vec{H}(t)] / \Delta t \quad (5-6)$$

and

$$\vec{T}_M(t) = \tilde{B}(t) W W^T \tilde{B}^T(t) \vec{P} \quad (5-7)$$

¹It is shown from the simulation results that, in the case of ST, the optimal value for Δt is about 200 seconds. The updating frequency--i.e., the frequency at which \vec{T}_D is calculated--is independent of Δt . To keep the advantages of the closed-loop aspects of this technique, the updating frequency can remain at 50 seconds.

The costate vector, \vec{P} , and the representation of $\vec{H}_{\text{NOM}}(t)$ are both precomputed.

5.3 DISCUSSION OF CURRENT CONTROL LAWS

Table 5-3 summarizes the equations used for the original and current control laws implemented for ST. Two alternative control laws (numbers 3 and 5) are also included in the table for comparison. Control law 1 is the original CP law, which is a closed-loop control law that minimizes the difference between the magnetic torque \vec{T}_M and the desired torque \vec{T}_D . In the determination of \vec{T}_D , the original CP law ignores the gravity-gradient torque, \vec{T}_{GG} , and replaces the system momentum \vec{H}_T by \vec{H}_{RW} , which is inefficient for attitude maneuvers. Control law 2 is the current CP law implemented onboard ST, which is a modified version of the original CP law. The current CP law is a closed-loop control law that minimizes the reaction wheel speed. It improves the determination of \vec{T}_D by including the gravity-gradient torque, \vec{T}_{GG} , and replacing \vec{H}_{RW} by \vec{H}_T to cover the case of maneuvers. It also provides a center speed control loop to constantly update the value of \vec{H}_B instead of fixing \vec{H}_B at a predetermined value. Control law 3 is an alternative closed-loop control law that is similar to the current CP law except that it minimizes the energy consumption while keeping the projection of \vec{T}_M on \vec{T}_D as large as possible. Control law 4 is the current MF law implemented onboard ST, which is a modified open-loop control law that minimizes the energy. In control law 4, a nominal momentum profile \vec{H}_{NOM} is computed for each of the inertial attitudes using a half-orbit as the desaturation period. This \vec{H}_{NOM} is then used in the determination of \vec{H}_D when a shorter desaturation period (600 seconds) and updating frequency (200 seconds) are used. As discussed in Section 5.2.2, the purpose of this modification is to reduce the error made in an open-loop control law in case undetected failure conditions exist. Control law 5 is an alternative open-loop control law that is similar to the

Table 5-3. Summary of Control Law Equations

CONTROL LAW ID	DESCRIPTION	DESIRED TORQUE \vec{T}_D	DESIRED MOMENTUM $\vec{H}_D = \int_{t_i}^{t_f} \vec{T}_D$	COSTATE VECTOR \vec{p}	SYSTEM MAGNETIC DIPOLE MOMENT $\vec{\mu}_M$	MAGNETIC TORQUE $\vec{T}_M = \vec{\mu}_M \times \vec{B}$	COMMANDED MAGNETIC DIPOLE MOMENT $\vec{\mu}_T = M^T (MM^T)^{-1} \vec{\mu}_M$
1	ORIGINAL CP LAW	$-K_M (\vec{H}_{RW} + \vec{H}_B)$	NOT APPLICABLE	$(\vec{B}^T \vec{B})^{-1} \vec{T}_D$	$\vec{B}^T \vec{p}$	$\vec{B}^T \vec{p}$	$M^T (MM^T)^{-1} \vec{B}^T \vec{p}$
2 ^a	CURRENT CP LAW	$-K_M (\vec{H}_T + \vec{H}_B) - \vec{T}_{GG}$	NOT APPLICABLE	$(\vec{B}^T WW^T \vec{B})^{-1} \vec{T}_D$	$WW^T \vec{B}^T \vec{p}$	$\vec{B}^T (WW^T \vec{B})^{-1} \vec{T}_D$	$M^T (MM^T)^{-1} WW^T \vec{B}^T \vec{p}$
3	ALTERNATIVE CLOSED-LOOP CONTROL LAW	$-K_M (\vec{H}_T + \vec{H}_B) - \vec{T}_{GG}$	NOT APPLICABLE	$(\vec{B}^T MM^T \vec{B})^{-1} \vec{T}_D$	$MM^T \vec{B}^T \vec{p}$	$\vec{B}^T MM^T \vec{B}^T \vec{p}$	$M^T \vec{B}^T \vec{p}$
4 ^a	CURRENT ME LAW	$\dot{\vec{H}}_{RW} - \vec{T}_{GG}$	$\vec{H}_{NOM}(t_f) - \vec{H}_{RW}(t_i) - \int_{t_i}^{t_f} \vec{T}_{GG}$	$\left[\int_{t_i}^{t_f} \vec{B}^T MM^T \vec{B} \right]^{-1} \vec{H}_D$	$MM^T \vec{B}^T \vec{p}$	$\vec{B}^T MM^T \vec{B}^T \vec{p}$	$M^T \vec{B}^T \vec{p}$
5	ALTERNATIVE OPEN-LOOP CONTROL LAW	$\dot{\vec{H}}_{RW} - \vec{T}_{GG}$	$\vec{H}_{NOM}(t_f) - \vec{H}_{RW}(t_i) - \int_{t_i}^{t_f} \vec{T}_{GG}$	$\left[\int_{t_i}^{t_f} \vec{B}^T WW^T \vec{B} \right]^{-1} \vec{H}_D$	$WW^T \vec{B}^T \vec{p}$	$\vec{B}^T (WW^T \vec{B})^{-1} \vec{T}_D$	$M^T (MM^T)^{-1} WW^T \vec{B}^T \vec{p}$

^aCONTROL LAW CURRENTLY IMPLEMENTED ONBOARD ST.

7081/80

current ME law except that it minimizes the reaction wheel speed caused by the secular term of \vec{T}_{GG} . \vec{H}_{NOM} should also be computed under the same criteria.

Notice that in the determination of \vec{T}_D and \vec{H}_D for the current ME law, the total momentum \vec{H}_T given in Equations (5-1) and (5-2) has been replaced by the reaction wheel momentum \vec{H}_{RW} . This is due to the special way the current ME law is implemented (refer to Section 2.3.2.1), which does not require knowledge of the system momentum during maneuvers. In the case of maneuvers, the normal mode of operation of the current ME law with a 600-second desaturation period and 200-second updating frequency is terminated. It is replaced by a single maneuver desaturation period which includes a lead time before the start of the maneuver and a lag time after the end of the maneuver. Thus, the length of the maneuver desaturation period depends on the lengths of the maneuver and the lead/lag times. In the current onboard implementation, each maneuver has a single lead/lag time that will be determined by the STOCC and uplinked to the spacecraft with the maneuver commands.

The drawbacks of the current ST momentum management implementation are summarized below.

1. The current CP law is not an ideal control law because of the general problems associated with all the closed-loop control laws (refer to Section 5.2.2). In summary, it does not take advantage of the variations in geometry and therefore does not dump the right amount of momentum at the right time. As a result, a great deal of energy is wasted in changing the direction of the momentum and dumping the momentum generated by the periodic portion of the gravity-gradient torque.

2. The current ME law uses the energy minimization criterion, which may not be the best choice for ST momentum management. Minimizing the wheel speed may be more important than minimizing the energy. In other words, the ST requirements may be better met if the current ME law is replaced by control law 5 in Table 5-3.

3. At inertial attitudes, the current ME law uses 600-second desaturations periods with 200-second updating frequencies to reduce the possible error introduced by undetected failure conditions. However, this choice of desaturation period and updating frequency is still not optimal. The updating frequency of the control law can be further improved if the "mixed-mode control law" described in Section 5.2.2 is used; this is a closed-loop control law operated with the precomputed open-loop \hat{H}_{NOM} . Details of this control law are given in Section 5.4.

4. Another drawback of the current ME law is excessive wheel speed after slew maneuvers, especially under undetected failure conditions (see Section 4). This problem with maneuvers is caused by the special way the maneuvers are handled in the current ME law. Depending on the length and geometry of the maneuver and the length of the lead/lag time used, the maneuver desaturation period may be too short to provide enough geometrical variation, while on the other hand, it may also be too long to recover an error caused by undetected failure conditions because the magnetic dipole command is not updated throughout the maneuver desaturation period. It is very difficult to define the maneuver desaturation period so that both requirements can be met at the same time.

Because of the drawbacks with the current implementation, alternative techniques are suggested for both inertial and maneuver cases to improve the current situation. These

techniques require minor modifications to the onboard implementation and are described in the following subsection.

5.4 ALTERNATIVE TECHNIQUES

Because of the problems associated with the current control laws as discussed in Section 5.3, a new technique called the "mixed-mode MWS law" is suggested to replace the current ME law. This mixed-mode MWS¹ law has already been introduced in Section 5.2.2 and is given in more detail in this subsection. In addition, to resolve the current problems with maneuvers, a technique of implementing the mixed-mode MWS law during maneuvers also is presented.

5.4.1 ALTERNATIVE TECHNIQUE AT INERTIAL ATTITUDES

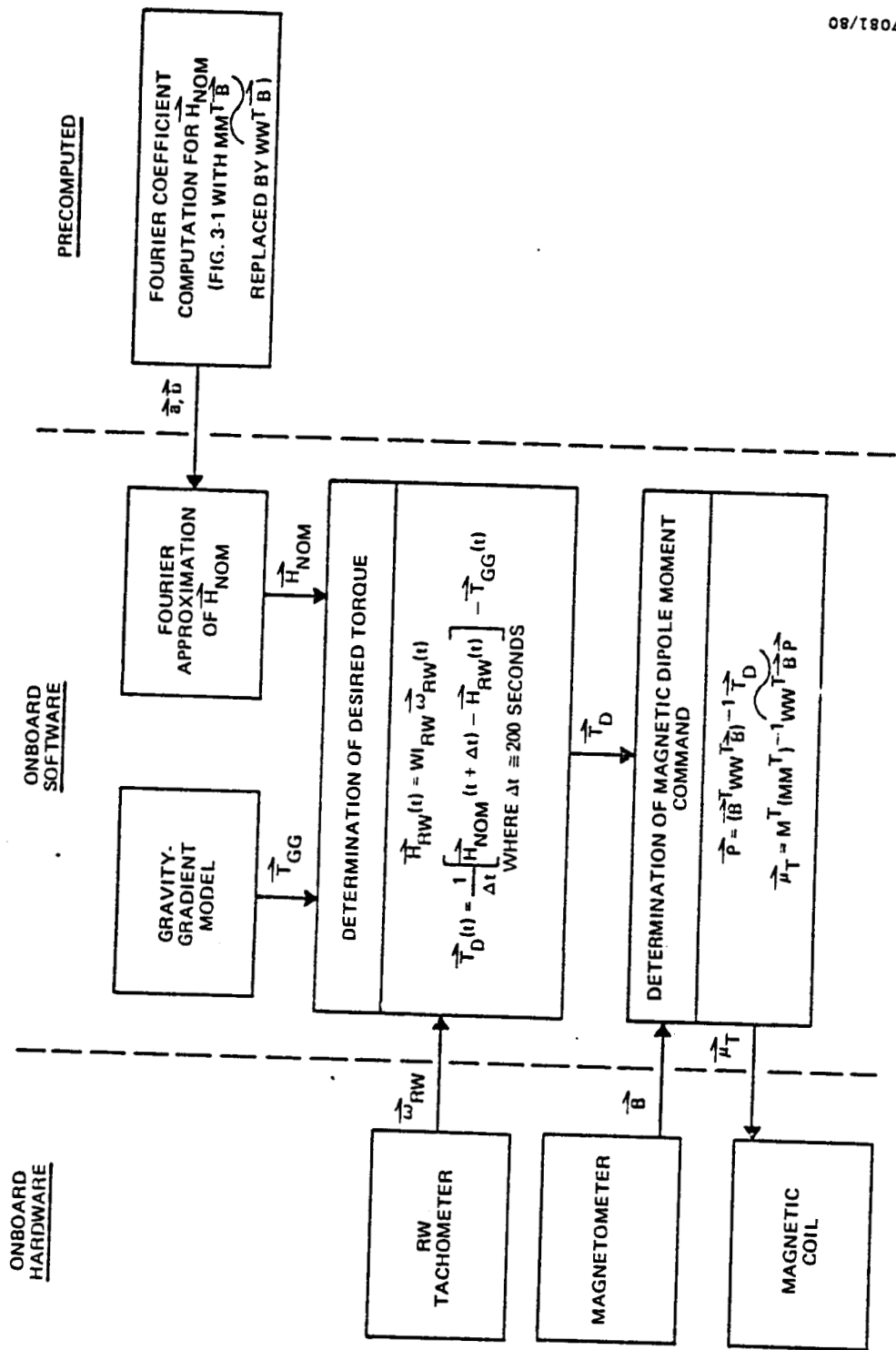
The mixed-mode MWS law is a closed-loop minimum wheel speed control law operated with an open-loop \vec{H}_{NOM} . For the case of inertial attitude, \vec{H}_{NOM} is obtained as in Figure 3-1 except that in the computations of \vec{P} and \vec{T}_M , the operator $MM^T \vec{B}$ is replaced by $WW^T \vec{B}$. Once \vec{H}_{NOM} is obtained, a closed-loop MWS law will be used onboard that computes \vec{T}_D through Equation (5-4), with $\vec{H}_T(t)$ replaced by $\vec{H}_{RW}(t)$. This technique at inertial attitudes is summarized in Figure 5-3. The advantages of this new technique over the current control laws are given below.

5.4.1.1 Advantages Over the Current CP Law

The mixed-mode MWS law is better than the current CP law because it computes the desired torque based on the nominal momentum profile precomputed using an open-loop control law with half-orbit desaturation period. The desired torque so determined has the following advantages:

1. It takes advantage of future geometrical variations so that the proper amount of momentum will be dumped at the proper time.

¹The MWS criterion is used for historical reasons in ST momentum management. The ME criterion could also be used in other applications.



7081/80

Figure 5-3. Baseline Diagram of Mixed-Mode MWS Control Law at Inertial Attitudes

2. Only the nonperiodic portion of the gravity-gradient momentum will be dumped by the magnetic torquers.
3. The desired torque is always nearly perpendicular to the geomagnetic field so that very little energy will be wasted in changing the direction rather than reducing the magnitude of the momentum.
4. The reaction wheel center speed control loop is no longer needed because the targeting momentum \vec{H}_{NOM} automatically keeps the reaction wheel center speed at zero. This greatly simplifies the onboard computation, as can be seen by comparing Figure 5-3 with Figure 2-3.

5.4.1.2 Advantages Over the Current ME Law

The mixed-mode MWS control law has the following advantages over the current ME law:

1. It reduces the updating frequency of the magnetic coil commands from 200 seconds to approximately 50 seconds. This will reduce the deviation between the actual and the predicted results when undetected failure conditions exist.
2. It uses the MWS instead of the ME minimization criterion, which may be advantageous if large wheel speeds should be avoided.
3. There is no need of defining a desaturation period onboard. This eliminates the possibility of having a near-singularity condition in computing the co-state vector \vec{P} .
4. The required onboard computation for inertial pointing is much simplified because it does not require the predicted geomagnetic field computation, and no

integration is involved. This can be seen by comparing Figure 5-3 with Figure 2-6.

5.4.2 ALTERNATIVE TECHNIQUE FOR MANEUVERS

The mixed-mode MWS law can be slightly modified to cover the case of maneuvers so that the current drawback with maneuvers (number 4 given in Section 5.3) can be resolved. Two fundamental factors complicate the situation during maneuvers: (1) the spacecraft body coordinate is no longer fixed in inertial space and (2) the nominal momentum profile \vec{H}_{NOM} can no longer be represented by a simple first-order Fourier expansion. To overcome the first complication, a command generator (currently implemented onboard) is required to compute $\Gamma_{t,t'}$, the coordinate transformation between the body coordinates at two different times. To overcome the second complication, instead of storing the Fourier coefficients, the costate vector P that is precomputed using a half-orbit desaturation period can be stored onboard for computing \vec{H}_{NOM} . Since P remains constant for the entire desaturation period, the value of \vec{H}_{NOM} at any time within the desaturation period can always be computed from P using the equation for \vec{T}_M and integrating Equation (2-4) once P is obtained. The implementation of the mixed-mode MWS control law for maneuvers is shown in Figure 5-4. With this implementation, in addition to the Fourier coefficients, computed for each of the inertial attitudes, a costate vector for each of the maneuvers also is required. The maneuver desaturation period is chosen to cover the period from a half-orbit before the end of the maneuver to the end of the maneuver to ensure large geometrical variations.¹ This eliminates the necessity of

¹While a shorter period may be desirable, long desaturation periods are not of concern because the mixed-mode control law updates commanded torques frequently, eliminating problems due to failure conditions.

determining the lead/lag time for each of the maneuvers. In case the start time of the maneuver desaturation period so determined falls within another maneuver, then the end time of the maneuver should be used instead. This start time of the maneuver desaturation period should also be kept onboard for each of the maneuvers in addition to the costate vector \vec{P} . The control law given in Figure 5-3 will be used onboard at an inertial attitude until the start time of a maneuver desaturation period is reached. Then the control law will be switched to that given in Figure 5-4 until the end of the maneuver.

In Figure 5-4, the times in the superscripts indicate the times associated with the body coordinate systems in which the quantities are represented, while the times in the parentheses give the times at which the quantities are evaluated or measured. When there is no superscript, the two times will be the same; that is, the instantaneous body coordinate system is used. Figure 5-4 is similar to Figure 5-3 except that more onboard computation is required to compute the nominal momentum profile and the coordinate transformations. Actually the capability of computing the coordinate transformation during maneuvers already exists in the current implementation onboard ST. It is done by a simplified command generator that is turned on whenever the maneuver exceeds 10 degrees (Reference 5-1). Thus, no additional computational module is required onboard for this purpose. The computation of \vec{H}_{NOM} at a given time can be done by propagating \vec{H}_{NOM} from a previous time as shown in Figure 5-4, which involves very simple and straightforward processing.

The mixed-mode MWS technique for maneuvers given in Figure 5-4 overcomes current drawbacks with maneuvers because it updates the magnetic dipole commands at a closed-loop frequency throughout the maneuvers so that much better

control over the reaction wheel speed is expected after each maneuver, especially when undetected failure conditions exist.

In summary, with minor modifications to the current control laws implemented for ST, the alternative techniques shown in Figures 5-3 and 5-4 for the inertial and maneuver cases, respectively, seem to provide many advantages over the current control laws. Thus, these new techniques should be seriously considered as possible replacements for the current control laws. Simulation results are shown in Section 7 to compare the performance of this mixed-mode control law with the performance of the current control laws.

REFERENCE

- 5-1. Lockheed Missiles and Space Company, LMSC 4172682, ST
PCS Flight Software Algorithms, R. H. Jones, W. F.
Wright, and W. H. Whittier, October 1979

SECTION 6 - MATHEMATICAL MODEL ACCURACIES

This section discusses published accuracy requirements for the mathematical models used in the implementation of the CP and ME laws, which were presented in Sections 2 and 3.

6.1 MATHEMATICAL MODELS

The onboard implementation of the CP and ME control laws is summarized in Figures 2-3 and 2-6. The ultimate output from either law is the magnetic dipole moment command given by

$$\vec{\mu}_T = M^T \left(M M^T \right)^{-1} \frac{\vec{B}' \times \vec{T}_D}{\vec{B}' \cdot \vec{B}} \quad (6-1)$$

for the CP law and by

$$\vec{\mu}_T = \vec{M}^T \vec{B}_c \times \vec{P} \quad (6-2)$$

for the ME law. M is the magnetic coil mounting matrix. \vec{B} is the geomagnetic field measured by two redundant three-axis magnetometers and \vec{B}_c is that calculated from the onboard geomagnetic field model.¹ (Optionally, μ_T can be calculated from \vec{B} .)

Onboard implementation of the CP law requires determination of the desired torque, \vec{T}_D , which is calculated from

$$\vec{T}_D = -\vec{T}_{GG} - K_M \left(\vec{H}_T + K_P \vec{H}_{CSD} + K_\Sigma \vec{\Sigma} \right) \quad (6-3)$$

¹Note that in Section 6 the subscript "c" is used to denote calculated values.

Parameters in the second term on the right of Equation (6-3) are determined from RW tachometer and RGA data. The gravity-gradient torque, \vec{T}_{GG} , is calculated from

$$\vec{T}_{GG} = 3\Omega_o^2 \left[\hat{R}_V \times (I \hat{R}_V) \right]$$

where I is the ST inertia matrix, Ω_o is the vehicle orbital rate, and \hat{R}_V is the unit ST position vector in the spacecraft body-fixed coordinate system.

The costate vector, \vec{P} , required for implementation of the ME law at inertial attitudes is given by

$$\vec{P} = \left[\int_{t_o}^{t_f} \tilde{B}_c^T M M^T \tilde{B}_c^T dt \right]^{-1} \vec{H}_D \quad (6-5)$$

where

$$\vec{H}_D = \vec{H}_{NOM}(t_f) - \vec{H}_{RW}(t_o) - \int_{t_o}^{t_f} \vec{T}_{GG} dt \quad (6-6)$$

New parameters introduced in Equations (6-5) and (6-6) are defined as follows:

- $t_f = t_o + 600$ seconds and t_o is incremented in steps of 200 seconds.
- \tilde{B}_c is the dyadic representation of the magnetic field (Equation (2-30)) calculated from the onboard geomagnetic field model.
- \vec{H}_{NOM} is the approximation of the nominal momentum calculated from Fourier coefficients.
- \vec{H}_{RW} is the RW system momentum derived from RW tachometer measurements.

The computation of the Fourier coefficients of the nominal momentum profile by the STOCC is summarized in Figure 3-1.¹ The Fourier coefficients are computed from the equations

$$\vec{a} = \frac{2}{T} \int_{T_0}^{T_0+T} \vec{H}_{\text{NOM}}(t) \cos\left(\frac{2\pi}{T} t\right) dt \quad (6-7)$$

$$\vec{b} = \frac{2}{T} \int_{T_0}^{T_0+T} \vec{H}_{\text{NOM}}(t) \sin\left(\frac{2\pi}{T} t\right) dt$$

The nominal momentum profile is given by

$$\vec{H}_{\text{NOM}}(t_i) = \int_{T_0}^{t_i} (\vec{T}_M(t) + \vec{T}_{\text{GG}}(t)) dt \quad (6-8)$$

where

$$\vec{T}_M(t) = \vec{B}_c(t) \times \left[\text{MM}^T(\vec{B}_c(t) \times \vec{P}) \right] \quad (6-9)$$

$$\vec{P} = \left[\int_{T_0}^{T_0+T} \vec{B}_c \text{MM}^T \vec{B}_c^T dt \right]^{-1} \left[- \int_{T_0}^{T_0+T} \vec{T}_{\text{GG}} dt \right] \quad (6-10)$$

\vec{B}_c and \vec{B}_c are calculated from a geomagnetic field model, and \vec{T}_{GG} is calculated from Equation (6-4) using the ST ephemeris available to the STOCC.

¹Fourier coefficients are now computed onboard ST (Section 2.3.4).

T_0 is the time at the end of the last slew maneuver and T is the half-orbit period. Complete details of numerical integrations used in Equations (6-7) through (6-10) are given in Section 3.

6.2 ACCURACY REQUIREMENTS AND ESTIMATES

The accuracies of the calculations reviewed in Section 6.1 depend on the accuracies of sensor observations, alignment estimates of sensors and magnetic coils, and mathematical models, including the integration techniques used. Estimates of the magnetic coil mounting matrix, M , and the alignment matrices for the RWs and RGAs can be refined from an evaluation of the in-flight performance of the system. Biases in the measurement of \vec{B} can also be determined from postlaunch analysis. Requirements to estimate alignments and biases of magnetic coils, magnetometers, and other sensors and corresponding accuracy requirements for such determinations have not yet been published in Space Telescope Mission Operations Requirements (Reference 6-1). The remainder of this section discusses published accuracy requirements and estimates for the mathematical models.

The accuracy of calculations formerly performed by the STOCC is discussed by Wernli in Reference 6-2. Two accuracy requirements stated in that documented are

1. The accuracy of the magnetic field model should be such that the peak vector error is less than 10 percent.
2. The error in \vec{H}_{NOM} referenced to the peak value of $|\vec{H}_{NOM}|$ should not exceed 2 percent.

The latter requirement is repeated in Reference 6-3.

Wernli states that a six-dipole representation of the geomagnetic field can be used to fulfill requirements for both STOCC and onboard processing. The peak vector error in this representation is approximately 6 percent, with a root-mean-square error of about 2 percent. Wernli also states that a

30-kilometer position error in the ST ephemeris results in a gravity-gradient torque error of about 1 percent and a geomagnetic field error of about 2 percent. Presumably the geomagnetic field error due to ST position error is in addition to any error in the magnetic field model. The effects of errors in \vec{B}_c and \vec{T}_{GG} on the accuracy of \vec{H}_{NOM} are not discussed in Reference 6-2. The results of an analysis of integration techniques were presented, however. To achieve an accuracy of 2 percent in \vec{H}_{NOM} , Wernli recommends a maximum step size of 600 seconds when a fourth-order Runge-Kutta integration technique is used.

Specific requirements for the ephemeris accuracies necessary to perform mission planning and scheduling are given in Table 3-1 of Reference 6-1. In this table the accuracy requirement for the geomagnetic field strength (used for purposes of momentum management) is listed as 4 percent. The computed in-track ephemeris accuracy needed to realize this requirement is listed as 60 kilometers. It is further stated that orbit determinations are required to have an approximate prediction limit of 1 week. The relation in Reference 6-1 between ephemeris and magnetic field errors (60 kilometers versus 4 percent) is consistent with the statement in Reference 6-2 that a 30-kilometer position error causes a 2-percent error in the magnetic field determination. Neither reference defines the type of error (e.g., peak or root-mean-square) that is used. Therefore, it is unclear how to combine the magnetic field error due to ephemeris inaccuracy with error due to the magnetic field mode. Note that the 4-percent error due to ephemeris inaccuracy plus the 6-percent peak error (Reference 6-2) due to model inaccuracy equals the 10-percent accuracy requirement for \vec{B}_c specified in Reference 6-2.

In addition to the ephemeris required for mission planning and scheduling, ephemeris information for onboard processing must be supplied. Reference 6-3 specifies that the state vector used onboard for the calculation of the ST orbital position "... shall be update(d) at a frequency of 72 hours or less, and shall be specified with precision sufficient to maintain a 25 Km in-track accuracy over the 72 hours." The state vector contains Keplerian orbital elements from which the position is calculated using the equivalent of the standard expansion in terms of the eccentricity and mean anomaly (Reference 6-4). The effects of atmospheric drag are incorporated in the state vector itself (Reference 6-5).

Unofficial information (Reference 6-5) indicates that the accuracy requirement for the ST ephemerides may be relaxed to 120 kilometers for both ground and onboard processing with update frequencies of 8 to 10 days for the ground processing and 3 days for onboard.

A summary of available mathematical model accuracies and requirements is provided in Table 6-1. The first column of Table 6-1 gives the parameter. The second column gives specified accuracy requirements, when available. The ST position requirement is the one stated in Reference 6-1, which is necessary to maintain the desired magnetic field accuracy. The requirement for \vec{B}_C is taken from Reference 6-2 and appears to include allowance for errors from both the model and the ST position. The third and fourth columns give the estimated accuracies of \vec{T}_{GG} and \vec{B}_C for ST position accuracies of 30 kilometers and 120 kilometers, respectively. Errors in \vec{B}_C due to the model and ST position errors are stated, but no attempt is made to combine these errors. The accuracy of \vec{H}_{NOM} as a function of \vec{T}_{GG} and \vec{B}_C is unavailable.

This review of available documents reveals several deficiencies in the accuracy requirements for ST momentum management. These include the following:

- Requirements to estimate alignments and biases of magnetic coils, magnetometers, and other sensors and corresponding

Table 6-1. Mathematical Model Accuracies
and Requirements

<u>Parameter</u>	<u>Requirement</u>	<u>Accuracy Estimates</u>	
ST position	60 kilometers ¹	30 kilometers	120 kilometers
\vec{T}_{GG}	-	1 percent	4 percent
\vec{B}_C	10 percent ²	(6 percent + 2 percent) ³	(6 percent + 8 percent) ³
\vec{H}_{NOM}	2 percent	-	-

¹Reference 6-1.

²Reference 6-2.

³Includes the peak vector error due to the geomagnetic field model and the error due to ephemeris inaccuracy.

accuracy requirements for such determinations have not yet been published in Space Telescope Mission Operations Requirements (Reference 6-1).

- No accuracy requirement for the calculation of \vec{T}_{GG} is available in the documents reviewed.
- The accuracy requirement for the calculated geomagnetic field in Reference 6-1 appears not to include allowance for the errors due to the field model.
- No analysis of the combination of geomagnetic field errors due to field models and ST ephemerides is available in the documents reviewed.
- No analysis of the effect on \vec{H}_{NOM} of errors in the ST ephemeris, \vec{T}_{GG} , and \vec{B}_c is available in the documents reviewed.

It is recommended that investigation of these deficiencies be initiated to establish confidence in the ability of the ST momentum management techniques to perform their required functions.

REFERENCES

- 6-1. Lockheed Missiles and Space Company, LMSC 4171847F, ST Mission Operations Requirements, OP-01, Volume III, November 1980
- 6-2. --, SE EM No. PCS-205, Momentum Management Computations Performed by STOCC, A. Wernli, July 1978
- 6-3. --, LMSC 4171874B, ST Mission Operations Requirements (Appendix A - Ground Computational Support Requirements), October 1979
- 6-4. --, LMSC 4172682, ST PCS Flight Software Algorithms, R. H. Jones, W. F. Wright, and W. H. Whittier, October 1979
- 6-5. J. Hennessy (GSFC), private communication, 1980

SECTION 7 - COMPUTER STUDIES OF MOMENTUM MANAGEMENT PROCEDURES

7.1 ANALYTICAL SOFTWARE

CSC, in collaboration with General Software Corporation (GSC), has developed analytical software for GSFC to study ST momentum management. This software consists of a utility program for generation of nominal momentum profiles (HNOM) and the ST Onboard Control Law Simulator (STOCLS). The programs are written in FORTRAN and have been executed on GSFC's IBM S/360-95 computer.

The HNOM program follows the computation flow presented in Figure 3-1. It computes the geomagnetic field and gravity-gradient torque for up to 121 points distributed over one or more half-orbits for a given attitude. These data are used to calculate the costate vector, the resulting control torques, the history of momentum, and the Fourier coefficients representing \vec{H}_{NOM} . A standard program, employing Simpson's rule together with Newton's 3/8 rule, is used for all integrations.

STOCLS calculates angular momentum, reaction wheel speeds, and energy usage in the presence of gravity-gradient torques in time steps as fine as 1 second. STOCLS simulates the performance of the five different control laws given in Table 5-3 plus the mixed-mode law and simplified mixed-mode law described in Sections 5.2 and 5.4. Maneuvers, from one input attitude to another, can be simulated. The eigenaxis rotation is calculated from quaternions representing the attitudes. The maneuver consists of a constant acceleration for a specified time to a specified maximum angular velocity that is maintained as long as necessary, followed by constant deceleration. Diagnostic capabilities include:

- (1) the optional addition of random noise and/or bias to most observational and computed parameters in the control

law; (2) simulation of detected or undetected reaction wheel or torquer failure; (3) optional inclusion of perturbations due to the second harmonic in the expansion of the Earth's gravitational potential in the calculation of the orbital position vector; (4) several levels of diagnostic output with variable sampling rates; and (5) printer plots of reaction wheel speeds and angular momenta.

Both STOCLS and the HNOM utility program use the MAGFLD routine (Reference 7-1) to calculate the Earth's magnetic field from the International Geomagnetic Reference Field (1975). The order of the spherical harmonic model used can be varied from 1 to 8. Input attitudes for both programs are in the form of a 3-2-1 Euler angle rotation defined relative to the orbit. Details of all input parameters are given in the NAMELIST descriptions in Appendix B.

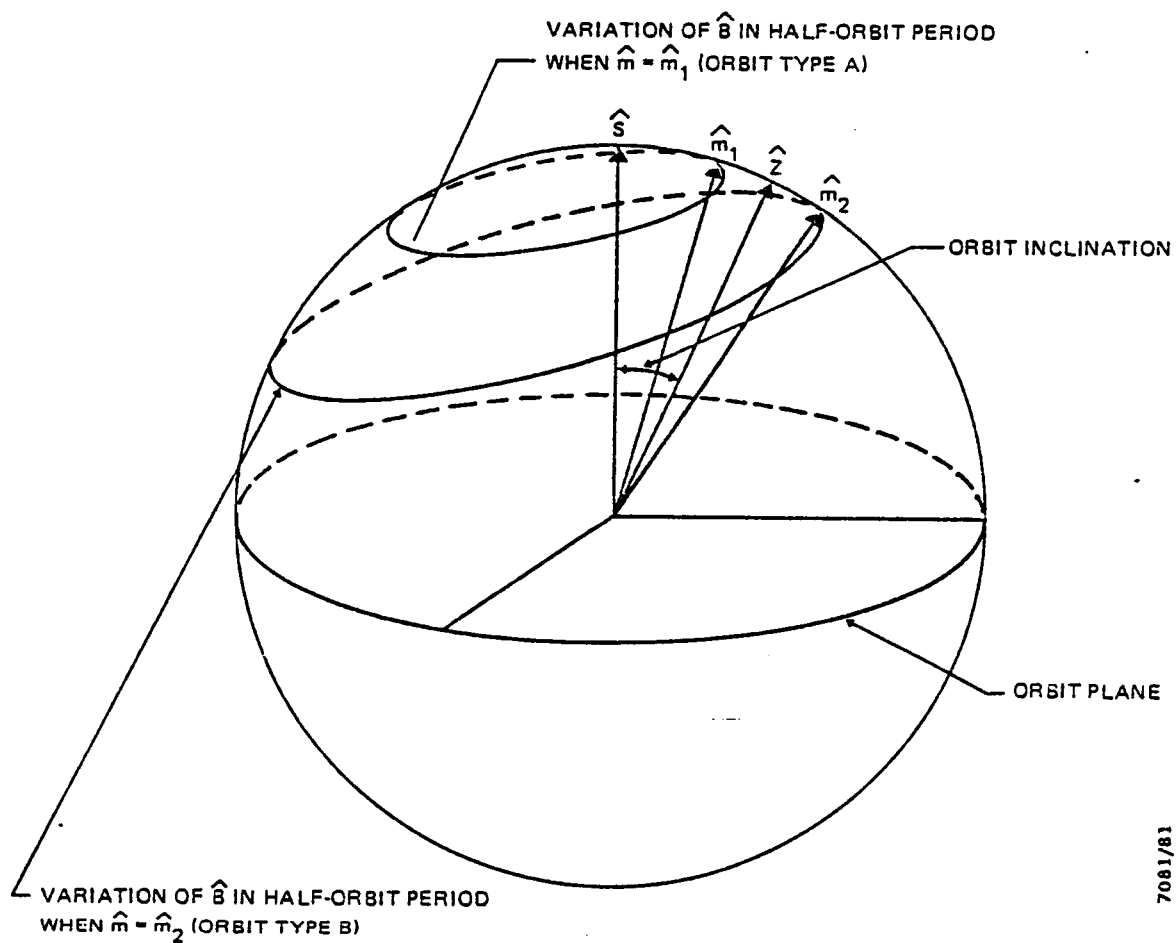
7.2 COMPUTER STUDIES

CSC and GSC, using the analytical software described in Section 7.1, have conducted computer studies of ST momentum management. A series of studies was designed to be representative of a large range of conditions. Extreme cases of the geometrical relation between the ST orbit and the geomagnetic field were defined, and the relations between attitude and gravity-gradient torques were established. The basis for the relations stated below is given in Appendix C, where analytical approximations to momentum management expressions are developed. The effects of the geomagnetic field were investigated for the following cases: (1) when the separation between the orbital pole and the Earth's north magnetic pole is minimum and (2) when this separation is maximum. These two cases are represented by orbits A and B, respectively, given in Table 7-1. The relationship between the geomagnetic field and the orbit for the two orbit types is shown in Figure 7-1. The attitude is specified by a 3-2-1 Euler rotation relative to the orbital reference frame. The rotation about Z, λ , controls the direction of the secular torque. The rotation about Y, β , controls the magnitude of the secular torque (with a maximum effect at a rotation of 45 degrees), and the magnitude and direction of the periodic torque. (The maximum of the combined periodic and secular torques occurs at $\beta = 35.3$ degrees.) The rotation about X, ϕ , has negligible effect for ST. Figure 7-2 shows the definition of the rotation angles λ and β , and Table 7-2 specifies the actual attitudes used in the computer studies.

The objectives and results of the computer studies are presented in the following subsections. Section 7.2.1 discusses fundamental properties of the physical quantities involved and the resulting accuracy of \vec{H}_{NOM} computations at inertial attitudes. Section 7.2.2 examines the

Table 7-1. Orbital Parameters Used in Studies

<u>Parameter</u>	<u>Orbit A</u>	<u>Orbit B</u>
Epoch	March 11, 1984 0 UT	March 11, 1984 0 UT
Semimajor axis	6878.165 kilometers	6878.165 kilometers
Eccentricity	0.0	0.0
Inclination	28.8 degrees	28.8 degrees
Right ascension of ascending node	188.14 degrees	8.14 degrees
Argument of perigee	0.0 degrees	0.0 degrees
Mean anomaly at epoch	0.0 degrees	0.0 degrees



7081/81

- \hat{S} = ORBIT POLE
- \hat{Z} = EARTH POLE
- \hat{m} = GEOMAGNETIC DIPOLE MOMENT

Figure 7-1. Sample Orbit Geometries

performance of closed-loop, open-loop, and mixed-mode control laws at inertial attitudes. Section 7.2.3 compares the performance of these control laws during maneuvers.

Table 7-2. Attitudes Used in Computer Studies

<u>Attitude</u>	<u>λ (Degrees)</u>	<u>β (Degrees)</u>
A	0	0
B	90	0
C	180	0
D	0	35.3
E	90	35.3
F	180	35.3
G	0	45
H	90	45
I	180	45

7.2.1 PROPERTIES OF PHYSICAL QUANTITIES AND ACCURACY OF \vec{H}_{NOM} COMPUTATIONS

The purposes of this study were to examine the properties of geomagnetic field models, to confirm expectations concerning gravity-gradient torques, and to determine the accuracy of the computation of \vec{H}_{NOM} profiles. In particular, second- and eighth-order spherical harmonic expansions of the field were compared with a simple dipole model. Expected properties of the gravity-gradient torque, \vec{T}_{GG} , for different attitudes include the following:

- \vec{T}_{GG} lies mainly in the YZ plane of the body coordinate system.
- The secular term of \vec{T}_{GG} lies mainly in the orbit plane (along the intersection of the body YZ plane and the orbit plane). It has maximum magnitude when $\beta = 45$ degrees and is nearly zero when $\beta = 0$ degrees or 90 degrees.
- T_{GG} is essentially independent of ϕ .
- The mean magnitude of \vec{T}_{GG} , including both the periodic and the nonperiodic terms, is maximum when $\alpha \approx 35.3$ degrees.

Appendix C develops the relations upon which these assertions are based.

The accuracy of \vec{H}_{NOM} calculations was assessed by computing the "true" \vec{H}_{NOM} for several orbits through a series of half-orbit runs with very fine step size (up to 121 steps) and fitting the profile with a fifth-order Fourier series. The effects of larger integration steps, lower order Fourier representation, and costate vector updates were then investigated.

Conclusions from these studies are summarized below.

1. The eighth-order geomagnetic field model has the correct general characteristics as predicted by the simple dipole model.¹ However, a large variation exists between the first and the second halves of an orbit period. The variation from one orbit to the next is relatively small. From the sample cases studied, the variation between orbits (maximum deviation versus maximum magnitude) is about 18 percent per orbit (Figures 7-3 and 7-4), whereas the variation between half-orbits is about 39 percent (Figure 7-5) for orbit type A and 32 percent (Figure 7-6) for orbit type B.

2. The second-order geomagnetic field behaves more like the simple dipole model. However, the variations between orbits and half-orbits remain at approximately the same level as those in the eighth-order model. The variation between the second- and the eighth-order models is relatively moderate, with a maximum deviation versus maximum magnitude ratio of about 15 percent (Figure 7-7).

3. The properties of the gravity-gradient torque are as predicted. Figure 7-8 shows a sample case where the secular term is expected to be along the Y direction.

NOTE: The attitude in this case and for the remaining cases discussed in this section is defined with $\beta = 45$ degrees.

4. Because of the variations in geomagnetic field between half-orbits, the costate vector required to unload the momentum due to the secular term of the gravity-gradient

¹The values of $|\vec{B}|$ from the eighth-order geomagnetic field model are consistent with those obtained from a map of $|\vec{B}|$ at a 500-kilometer altitude based on the 99-term Hendricks and Cain field expansion extrapolated to the year 1965 (Reference 7-2).

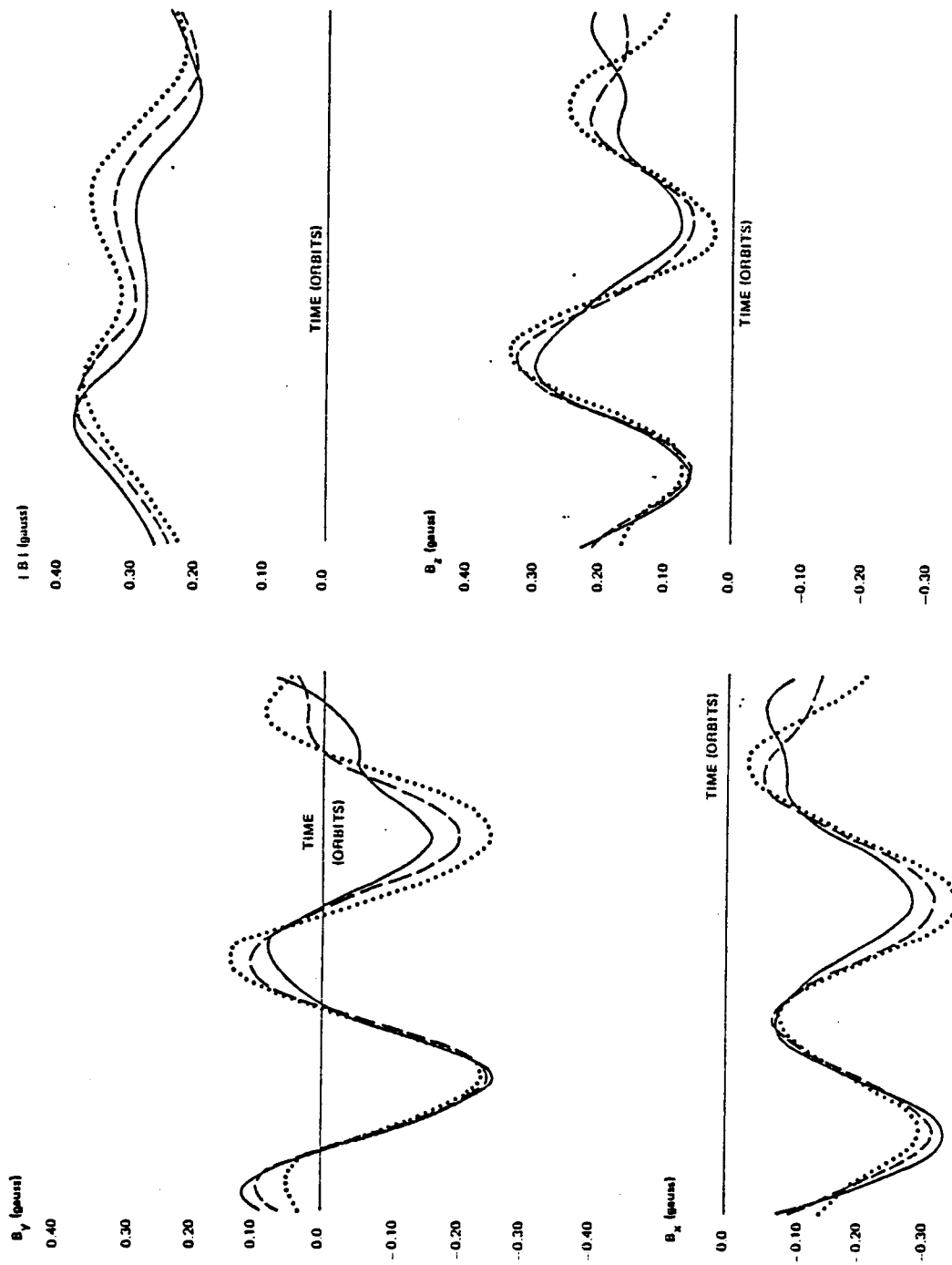


Figure 7-3. Variation of Eighth-Order Geomagnetic Field for Three Orbits, Orbit A (B_x , 16-percent deviation; B_y , 18-percent deviation; B_z , 16-percent deviation, $|B|$, 11-percent deviation.)

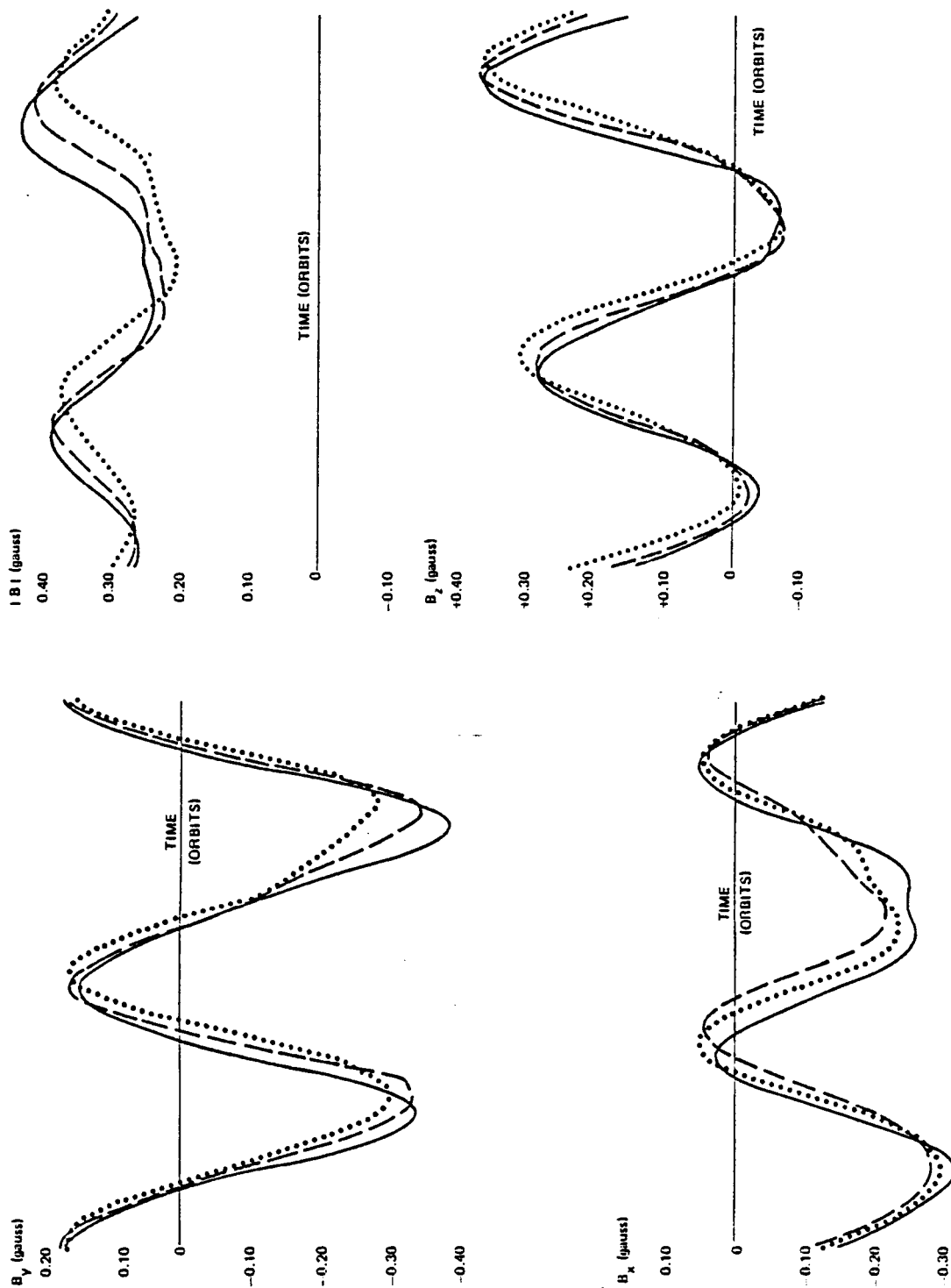


Figure 7-4. Variation of Eighth-Order Geomagnetic Field for Three Orbits, Orbit B (B_x , 14-percent deviation; B_y , 16-percent deviation; B_z , 14-percent deviation; $|B|$, 18-percent deviation.)

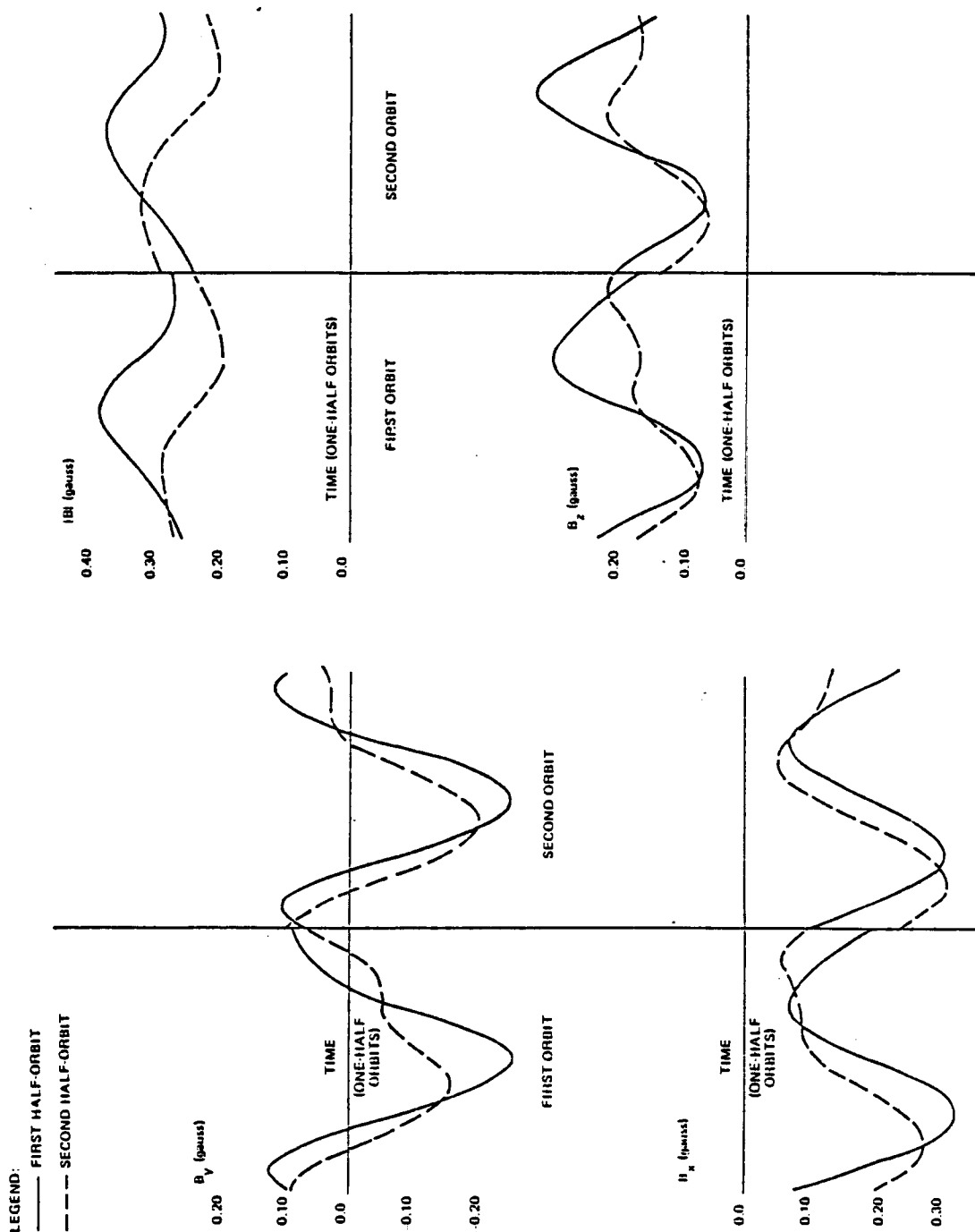


Figure 7-5. Comparison of Eighth-Order Geomagnetic Field Over Half-Orbit Intervals, Orbit A (B_x , 34-percent deviation; B_y , 37-percent deviation; B_z , 34-percent deviation, $|B|$, 39-percent deviation.)

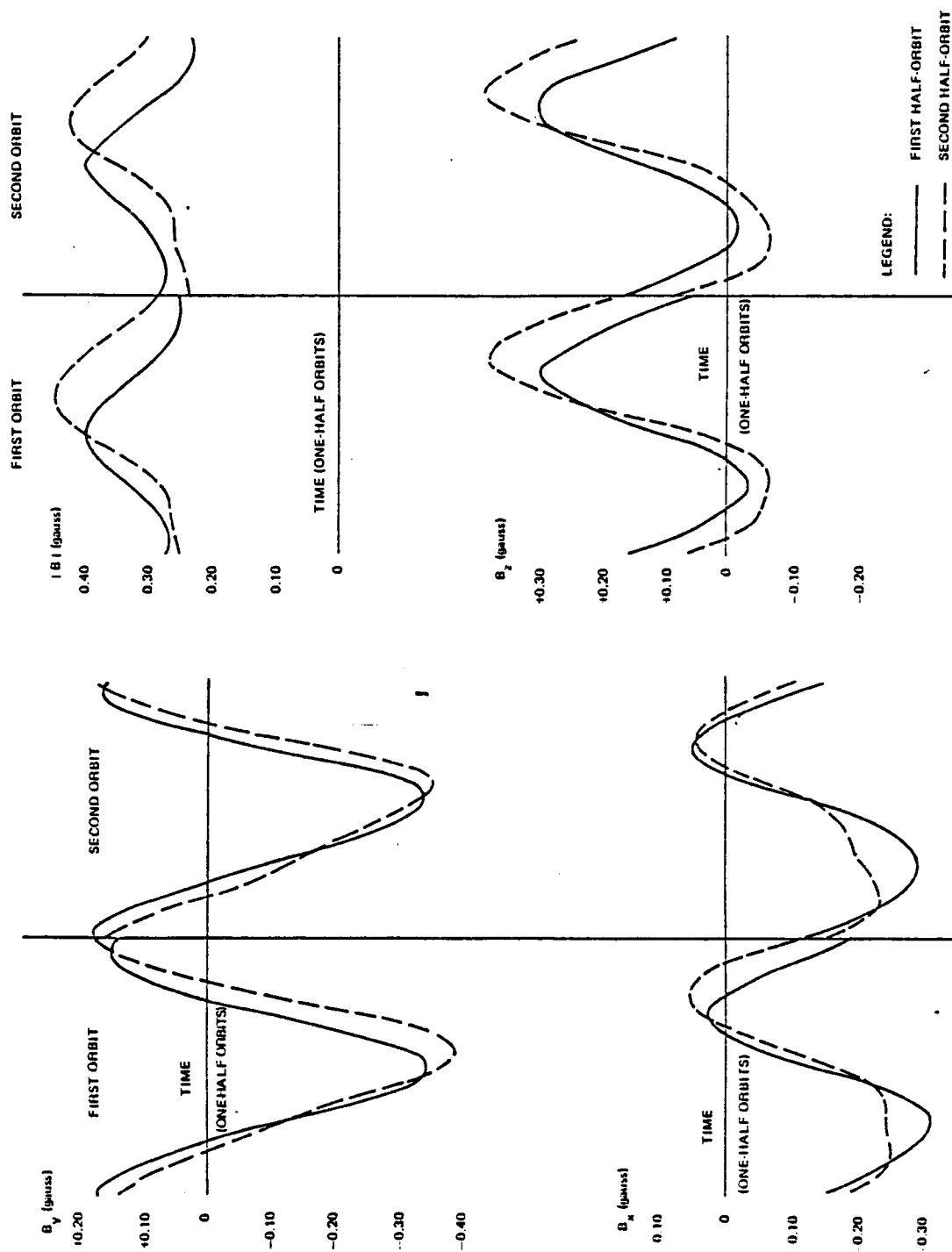


Figure 7-6. Comparison of Eighth-Order Geomagnetic Field Over Half-Orbit Intervals, Orbit B (B_x , 20-percent deviation; B_y , 32-percent deviation; B_z , 32-percent deviation; $|B|$, 27-percent deviation.)

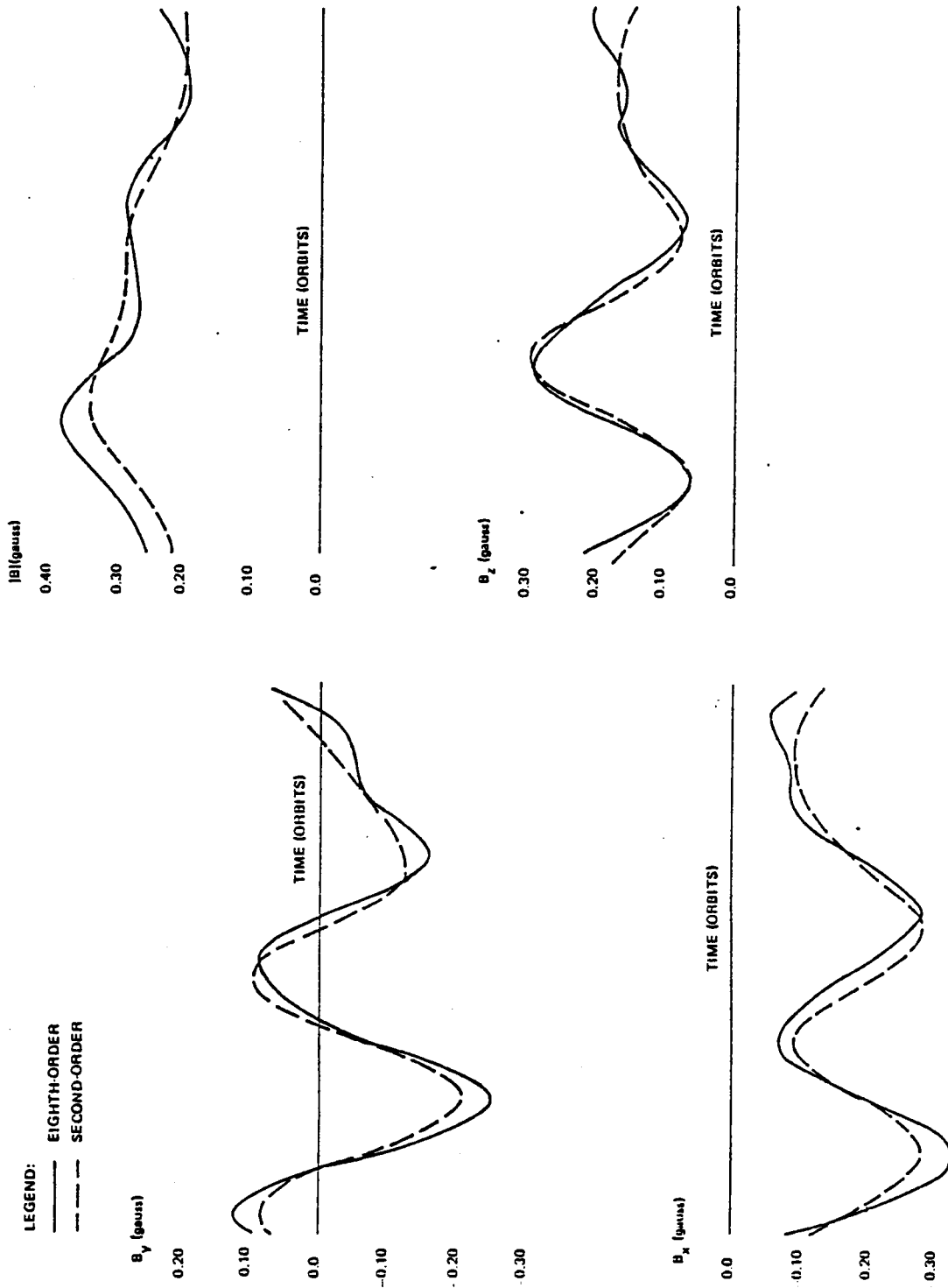


Figure 7-7. Comparison of Second- and Eighth-Order
Geomagnetic Fields, Orbit A

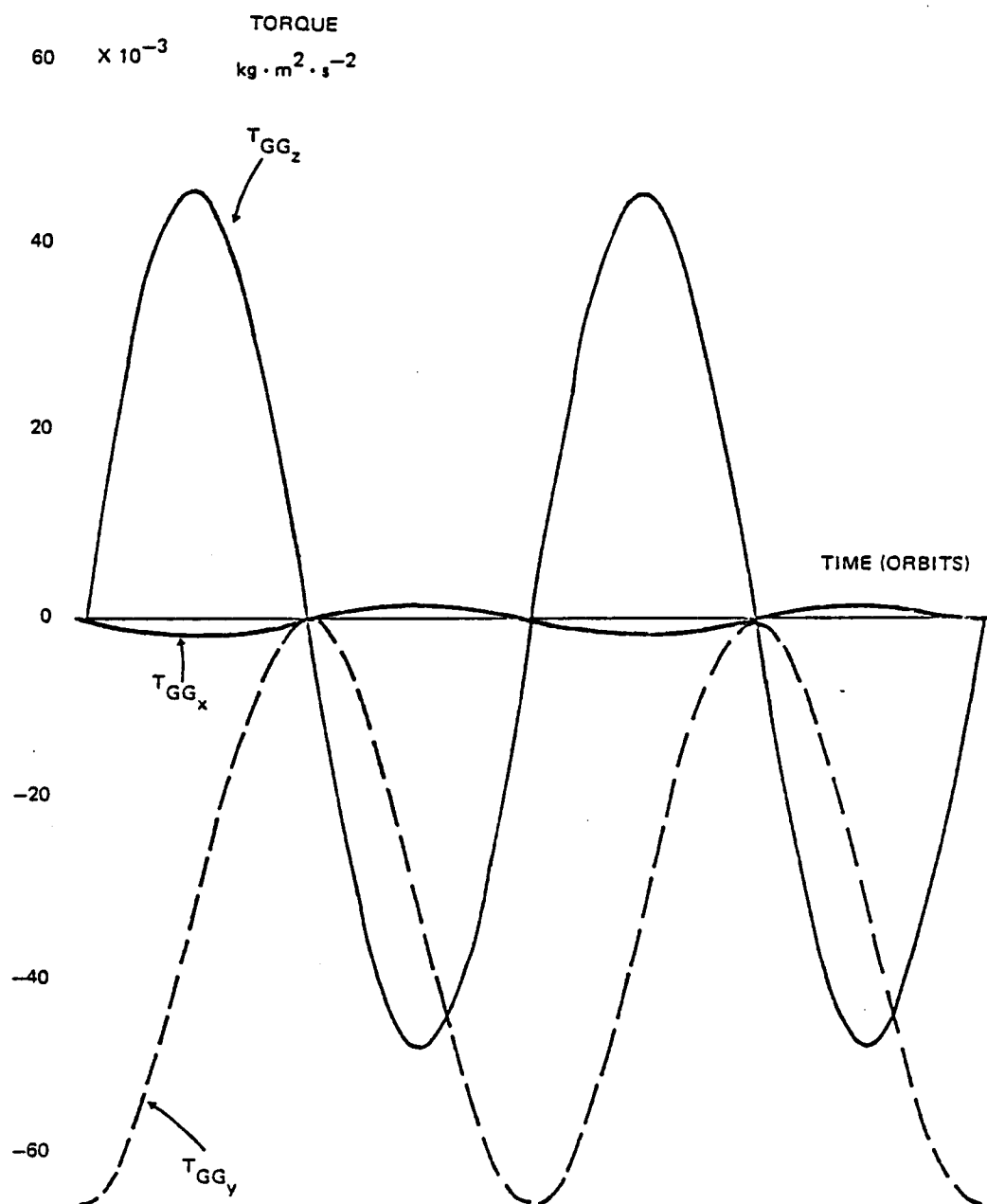


Figure 7-8. Gravity-Gradient Torque With Secular Term in Y Direction

torque is different for each half-orbit. If the same costate vector is used to obtain \vec{H}_{NOM} for the entire inertial period, a build-up in \vec{H}_{NOM} results. This is shown in Figure 7-9 for a period of three orbits. The build-up rate is approximately 28 percent per orbit. This shows that if the Fourier coefficients for \vec{H}_{NOM} are determined from a period longer than a half-orbit, the costate vector has to be updated every half-orbit.

5. The accuracy of \vec{H}_{NOM} representation depends on the following factors:

- a. The cycling time of the Fourier expansion, i.e., the period over which the Fourier representation repeats itself
- b. The length of duration included in the integrations for Fourier coefficient computations
- c. The order of the Fourier coefficients

Because of the large variations in \vec{H}_{NOM} between orbits and half-orbits (Figure 7-10), the accuracy of the \vec{H}_{NOM} representation is in general dominated by the cycling time selected for the Fourier expansion. To improve the accuracy, one of the following two conditions has to be met:

- a. Select the entire inertial period as the cycling time and include very high order Fourier coefficients.
- b. Use half-orbit or one-orbit cycling time with low-order Fourier coefficients but with frequent updates to the coefficients.

The accuracy of the \vec{H}_{NOM} representation for different orders of Fourier coefficients and different cycling times is shown in Figures 7-11 and 7-12. The percent errors of $|\Delta \vec{H}|_{\text{max}}/|\vec{H}|_{\text{max}}$ are 7.5, 1.1, and 0.1 for the first-,

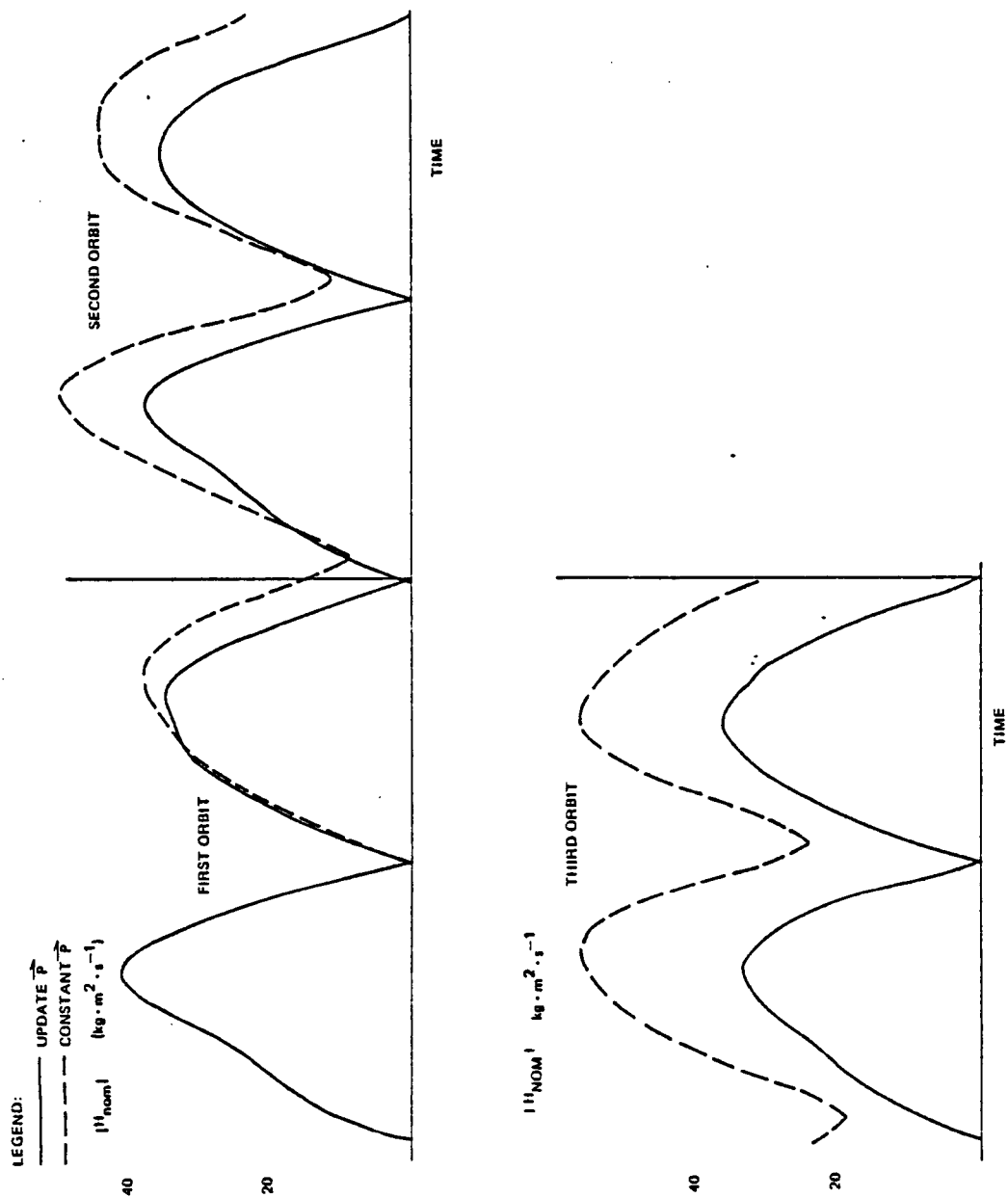


Figure 7-9. $|\vec{u}_{\text{nom}}|$ Profiles With Constant and Updated Costate Vectors, Orbit B

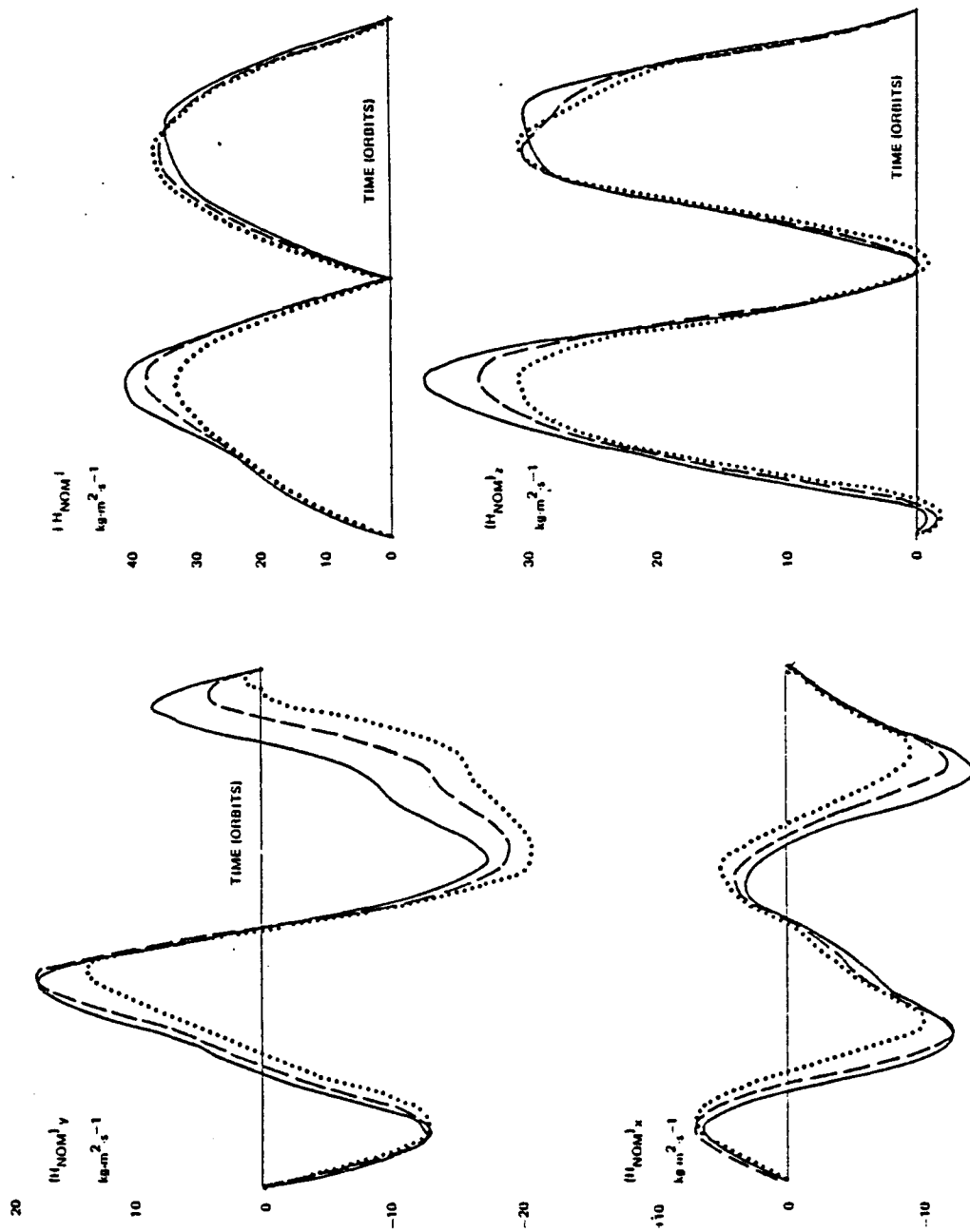


Figure 7-10. Variation in \vec{v}_{NOM} for Three Orbits, Orbit B

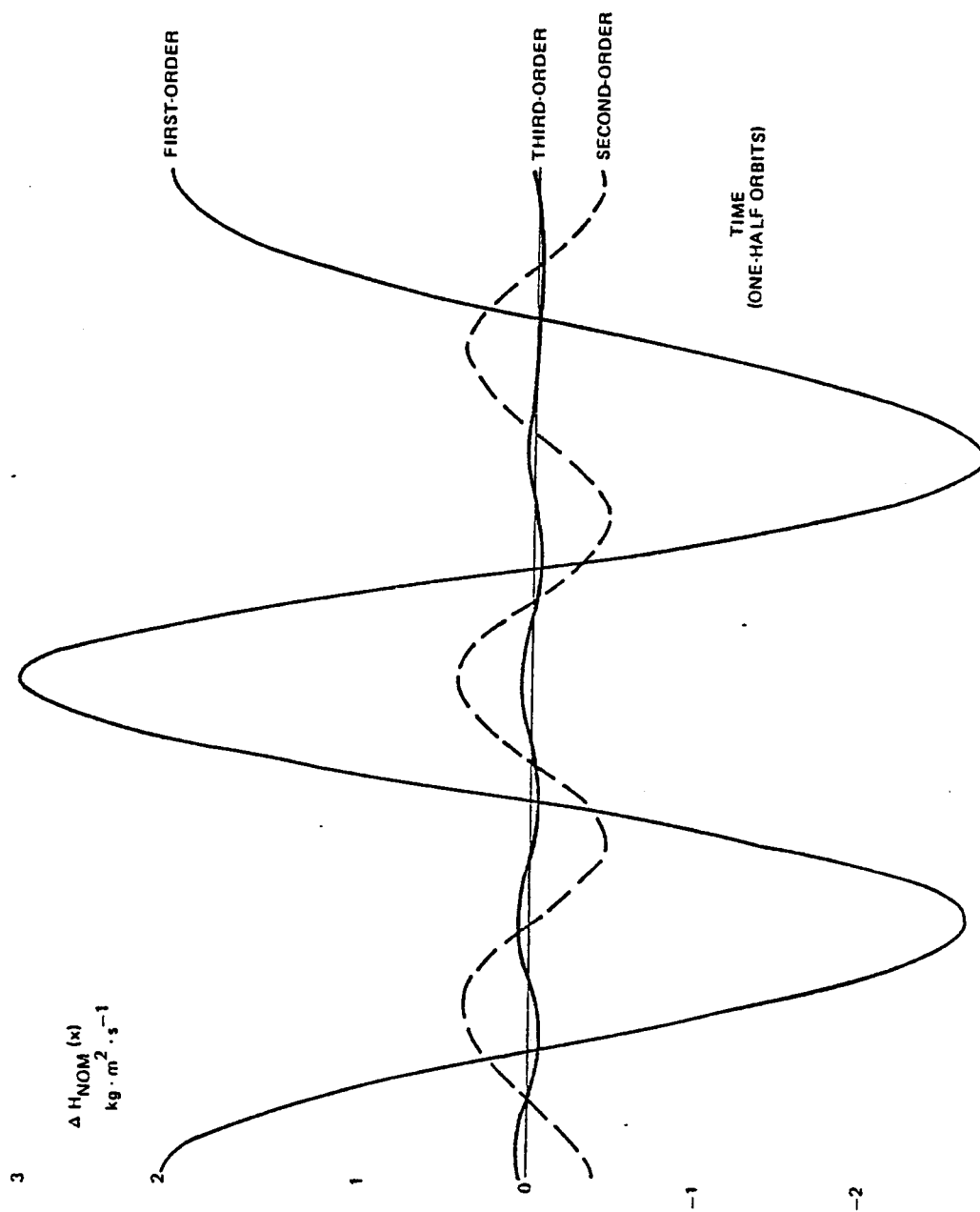


Figure 7-11. Errors in First-, Second-, and Third-Order Fourier Representation of \underline{H}_{NOM} for Cycling Time of One Half-Orbit

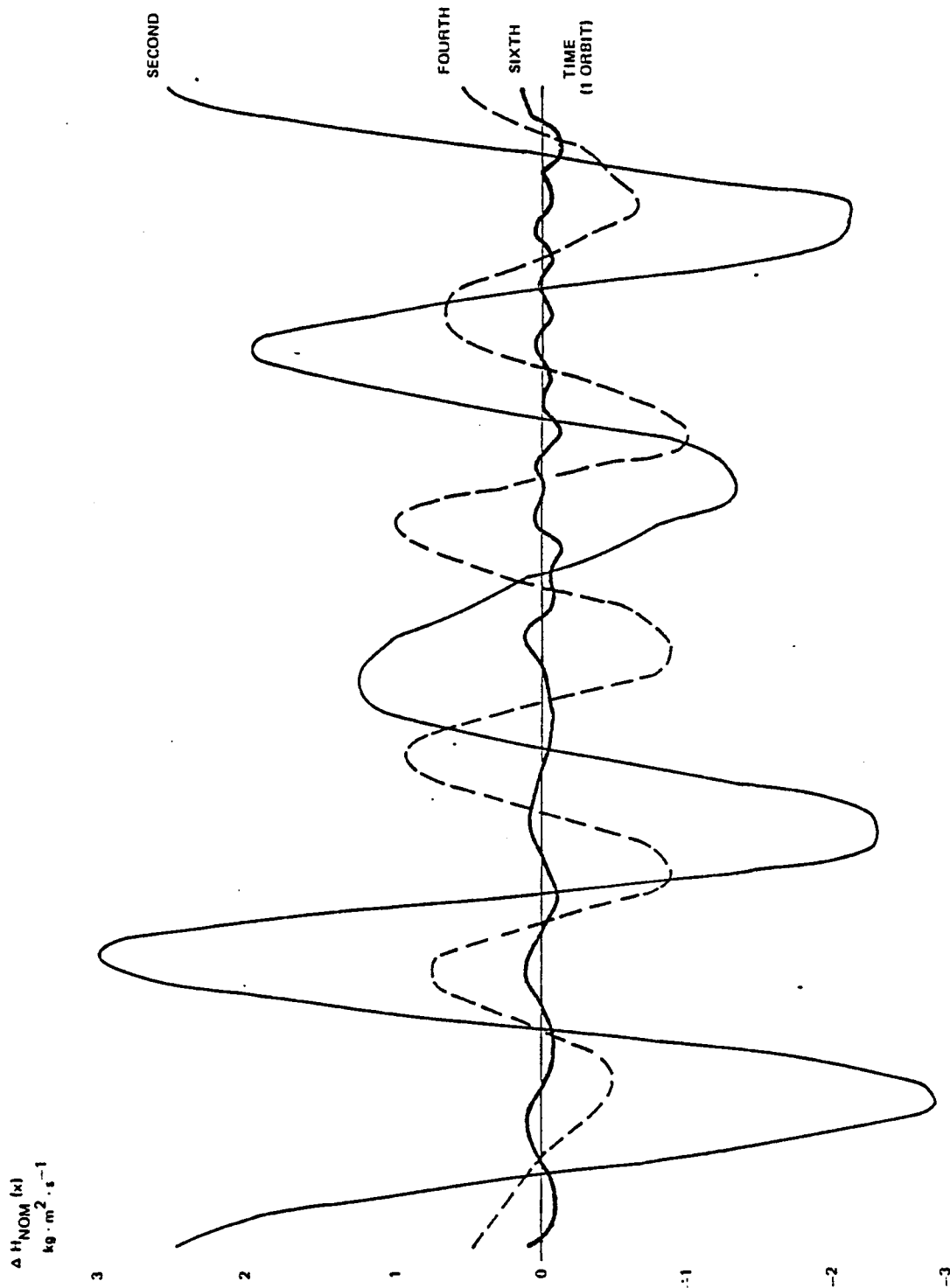


Figure 7-12. Errors in Second-, Fourth- and Sixth-Order Fourier Representation of \bar{H}_{NOM} for Cycling Time of One Orbit

second-, and third-order Fourier representations, respectively, in Figure 7-11, with similar results for the second-, fourth-, and sixth-order Fourier representations in Figure 7-12.

Numerical integration effects were tested by varying the number of integration steps from 5 to 121. Because of the dominance of the factors discussed above, the integration step size had negligible effect on the accuracy of the \vec{H}_{NOM} representation.

7.2.2 PERFORMANCE OF CONTROL LAWS AT INERTIAL ATTITUDES

This subsection presents the simulation results obtained from STOCLS for the case of inertial attitudes. The performance of the closed-loop, open-loop, and mixed-mode control laws is studied in Sections 7.2.2.1, 7.2.2.2, and 7.2.2.3, respectively, and a comparison of their performances is given in Section 7.2.2.4.

The purpose of these simulation studies can in general be summarized as the following: (1) to enhance our physical understanding of the control laws; (2) to optimize the constants used in the control laws; (3) to study the effects on the control law performance caused by different geometrical conditions; (4) to examine the sensitivity of the laws' performances against abnormal or failure conditions; and (5) to compare the performance of various control laws under both nominal and abnormal situations.

Unless stated otherwise, the nominal values of parameters listed in Appendix B are used for all studies. In particular, the reaction wheel moments of inertia are 0.382 kilogram-meter², the value used in previous studies of ST momentum management. Orbit type A (Table 7-1), with minimum separation between the orbital and geomagnetic poles, and attitude type G (Table 7-2) are used for all inertial attitude studies unless noted otherwise. Also, the initial wheel speeds are assumed to be zero. Wheel speeds, ω , are presented in hertz. Values for energy consumption, E , are proportional to actual energy usage and are given by

$$E = \int_{t=0}^T \left(\sum_{i=1}^4 \mu_{Ti}^2 \right) dt$$

in units of 10^8 (ampere-meters²) per second where $\vec{\mu}_T$ is the commanded magnetic dipole moment, T is one or more orbits, and the integration is approximated by summing over all time steps (nominally 1 second in length) in the simulation. When simulations extend beyond one orbital period, succeeding orbital periods are referred to as orbit 2, orbit 3, etc.

7.2.2.1 Performance of Closed-Loop Control Laws

The study results for the closed-loop control laws are summarized in the following subsections.

7.2.2.1.1 Magnetic Gain Study

A parametric study for the magnetic gain K_M was performed for a period of four orbits with the center speed control loop switched off. The results (Figure 7-13) show that the maximum wheel speed (ω_{\max}) is minimum when $K_M = 0.002$ and the energy consumption is minimum when $K_M = 0.0009$. From $K_M = 0.0009$ to 0.002 , ω_{\max} is improved by 13.7 percent at the expense of 5.0 percent more energy. The value $K_M = 0.002$ was chosen for all subsequent studies.

7.2.2.1.2 Center Speed Control Loop Study

A study was performed to optimize the constants used in the center speed control loop. The results show that the performance of the center speed control loop is very insensitive to the constant K_P . Essentially the same results were obtained for K_P ranging from 0. to 30. However, the performance of the center speed control loop is quite sensitive to the value of K_Σ . Figure 7-14 shows the variation of ω_{\max} with respect to the orbit number for K_Σ values ranging from 0.000 to 0.067. It can be seen that ω_{\max} improves with time when K_Σ varies from 0.000 to 0.010. However, when K_Σ is further increased, the center speed control loop tends to overcorrect the situation

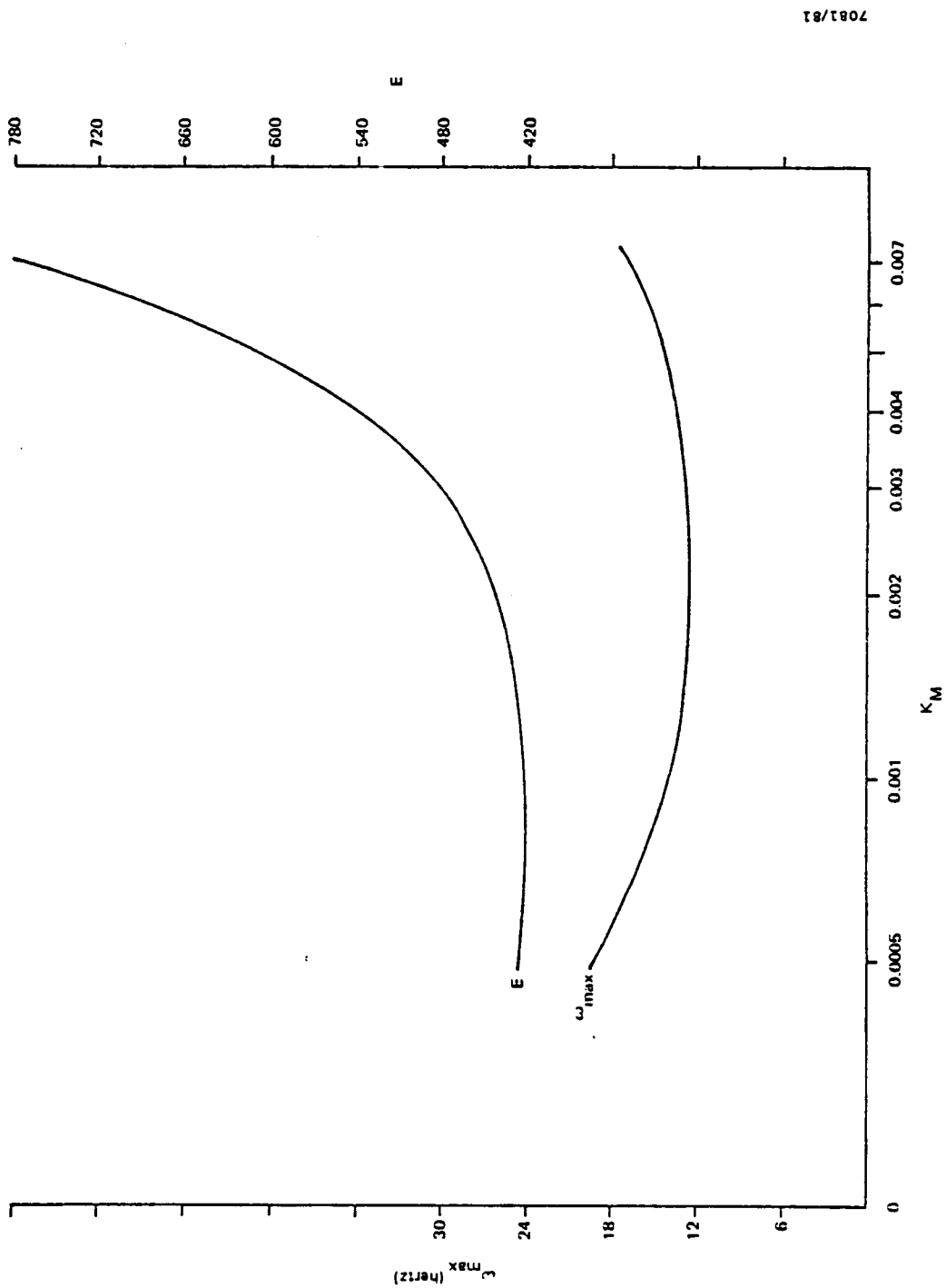
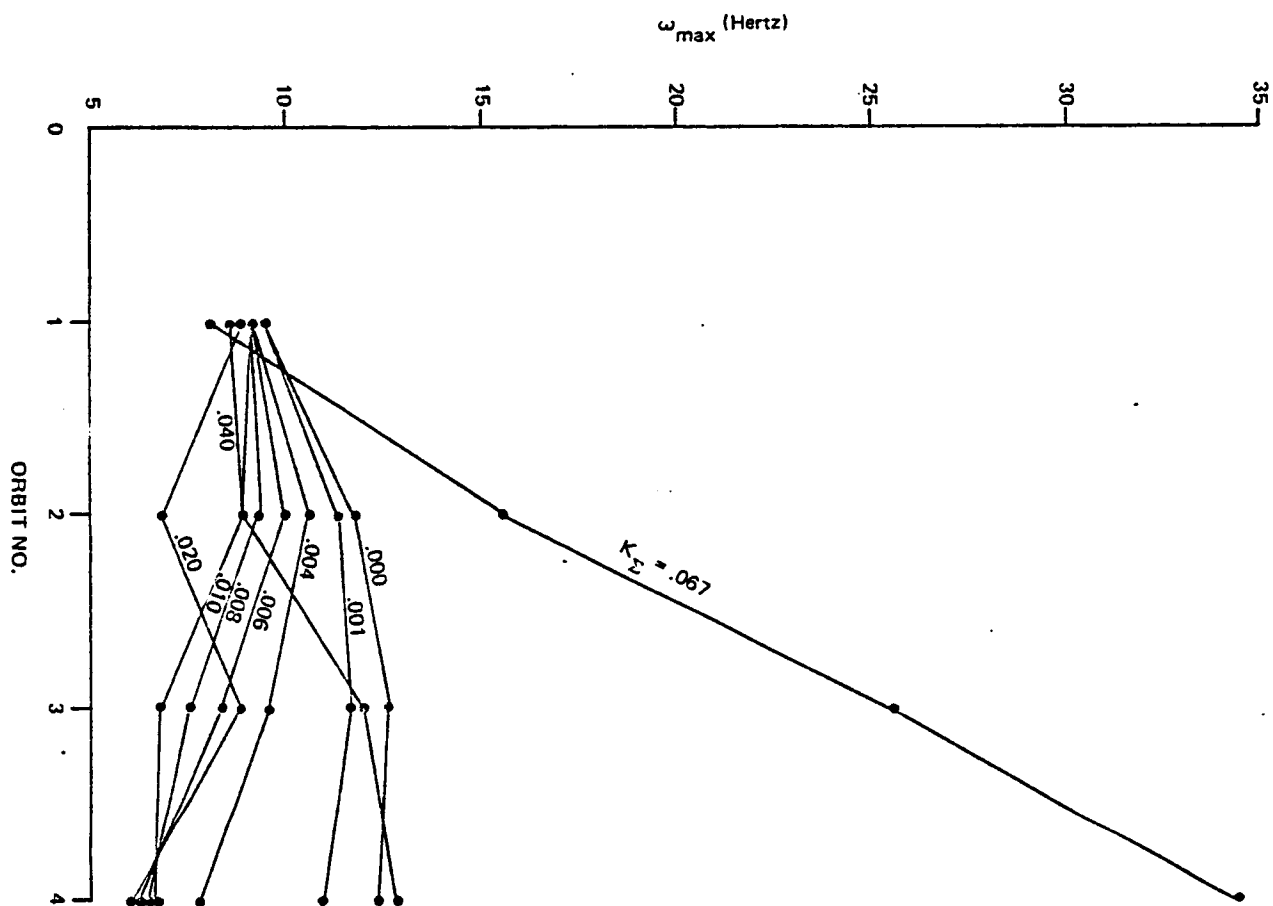


Figure 7-13. Parametric Study of K_M



7081/81

Figure 7-14. Dependence of Maximum Wheel Speed on K_{Σ}

and results in high fluctuations in the reaction wheel speeds. The energy consumption, which is shown in Figure 7-15, is not sensitive to K_{Σ} for any K_{Σ} value below 0.02. Thus, as a conclusion, the optimal value for K_{Σ} is approximately 0.01. $K_p = 0$ and $K_{\Sigma} = 0.02$ are used in all subsequent studies of the closed-loop control laws.

7.2.2.1.3 Geometry Study

The effects on the control law performance due to different orbit and attitude geometries are shown in Tables 7-3 and 7-4 and Figure 7-16. Table 7-3 gives the maximum wheel speeds (ω_{\max}) and the total energy consumption (E) during a four-orbit period with various attitude geometries for the two orbit types (A and B). The mean values of ω_{\max} , $\bar{\omega}_{\max}$, averaged over all attitudes and their standard deviations, σ , are also given in the table. Figure 7-16 plots $\bar{\omega}_{\max} \pm \sigma$ for the two orbit types and Table 7-4 lists the orbit numbers in which ω_{\max} exceeds $\bar{\omega}_{\max} + \sigma$. From Figure 7-16, orbit type B is better than orbit type A so far as the reduction of the reaction wheel speed is concerned. This is because the geomagnetic field carries higher geometrical variations in orbit type B (maximum separation of orbital and geomagnetic poles) than in orbit type A (see Figure 7-1). However, to achieve better wheel speed, orbit type B also requires more energy than orbit type A (see Table 7-3). From Table 7-4, the largest wheel speed excursions occur when $\beta = 35.3$ degrees, where $\vec{\pi}_{GG}$ has the maximum average magnitude. For the same β angle, $\lambda = 90$ degrees gives the worst geometrical condition for both orbit types. In general, good momentum management is achieved under normal conditions. The maximum reaction wheel speed is highest in the first orbit and drops continuously over the next few orbits (see Figure 7-16).

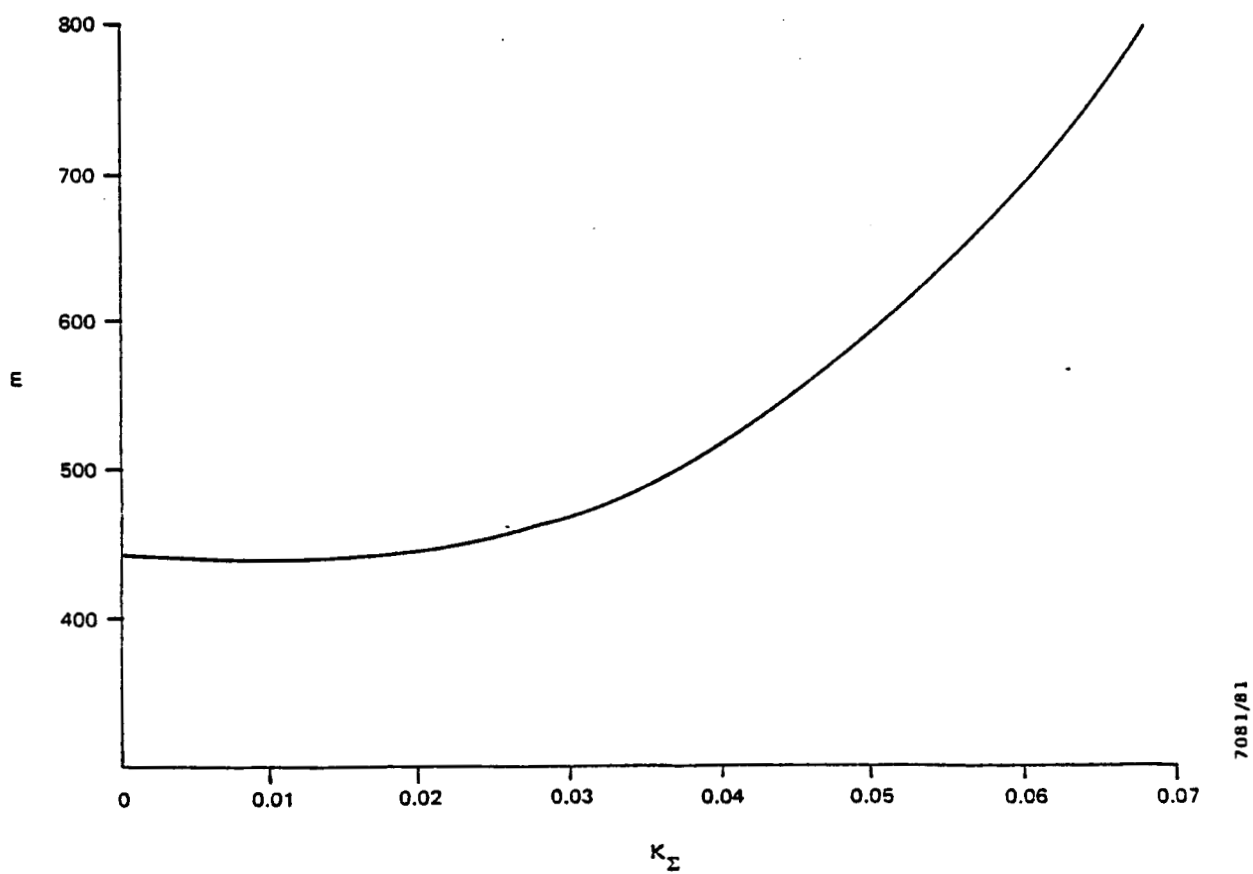


Figure 7-15. Dependence of Energy Consumption on K_{Σ}

Table 7-3. Geometry Dependence of Closed-Loop Control Laws

β	λ	ω_{\max} (Hz)				E
		ORBIT 1	ORBIT 2	ORBIT 3	ORBIT 4	
ORBIT TYPE A						
0	0	10.6	8.4	8.3	5.9	108
	90	11.6	8.4	8.3	6.0	98
	180	10.6	8.4	8.3	5.9	108
45	0	9.2	9.0	6.8	6.6	443
	90	10.4	9.8	9.2	8.0	387
	180	9.0	5.9	5.6	4.5	480
35.3	0	8.4	9.8	8.0	7.6	419
	90	12.4	10.6	10.8	8.2	392
	180	10.0	6.2	6.2	4.8	428
$\omega_{\max} \pm \sigma$		10.24 ± 1.27	8.50 ± 1.59	7.94 ± 1.58	6.39 ± 1.33	
ORBIT TYPE B						
0	0	8.8	5.1	4.5	5.1	228
	90	9.2	5.9	5.0	5.6	213
	180	8.8	5.1	4.5	5.1	228
45	0	10.8	7.2	6.2	4.7	510
	90	9.2	6.0	6.3	6.6	741
	180	7.5	6.0	6.2	5.0	557
35.3	0	11.4	7.4	6.2	4.5	452
	90	10.0	7.2	7.5	7.4	614
	180	8.4	5.9	6.2	5.1	558
MWS $\pm \sigma$		9.34 ± 1.21	6.20 ± 0.87	5.84 ± 0.99	5.46 ± 0.95	

7081/81

Table 7-4. Closed-Loop Control Law Performance for Comparison of Different Attitude Geometries

ORBIT TYPE	β	λ		
		0	90	180
A	0	—	1	—
	35.3	—	1, 2, 3, 4	—
	45	—	4	—
B	0	—	—	—
	35.3	1, 2	2, 3, 4	—
	45	1, 2	4	—

7081/81

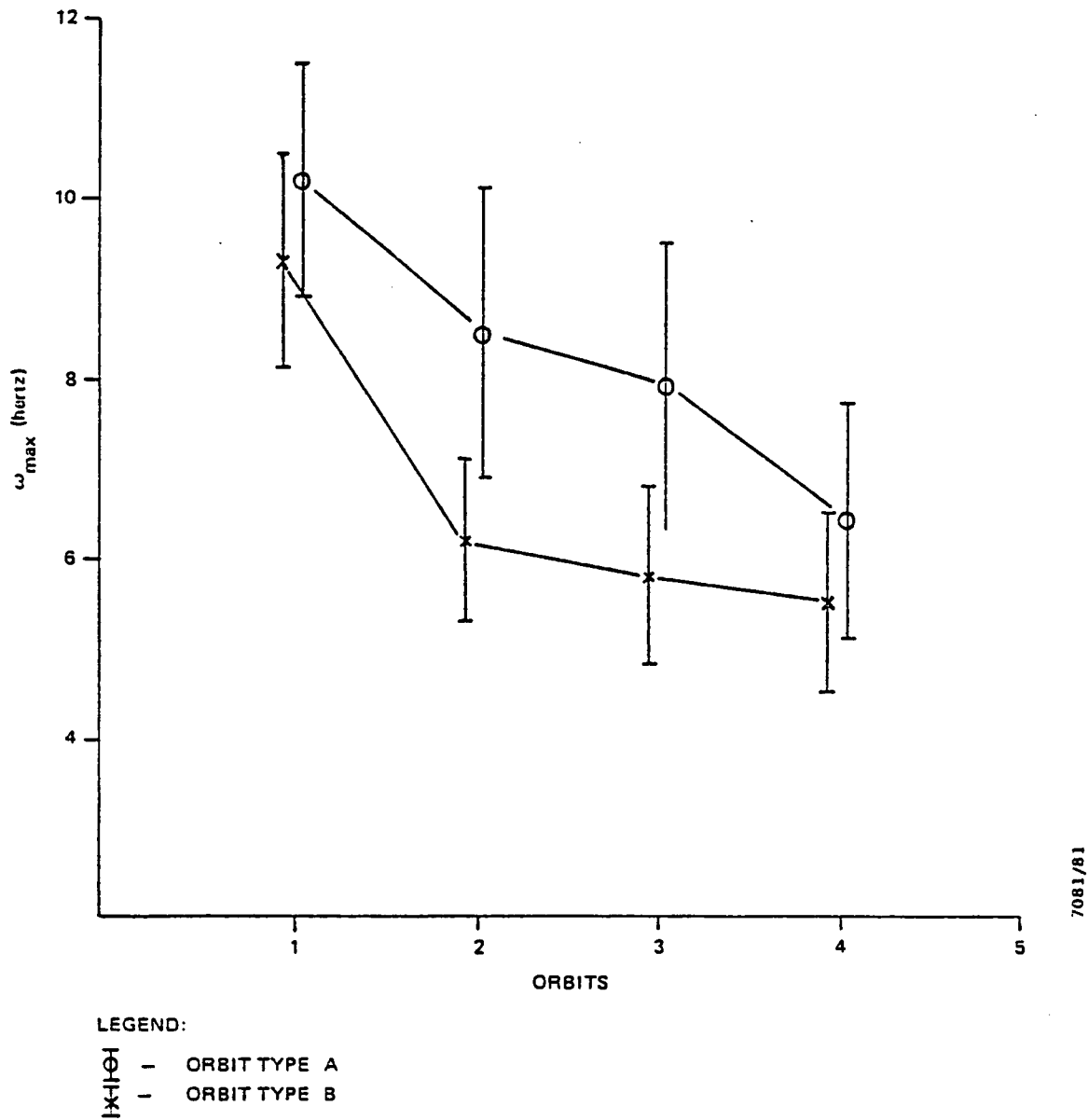


Figure 7-16. Comparison of Closed-Loop Control Law Performance for Different Orbit Geometries

7.2.2.1.4 Minimization Criteria Study

A study was performed to compare the performance of the current CP law (control law 2 of Table 5-3) with that of the alternative closed-loop control law (control law 3 of Table 5-3). The results show that the former gives about 25 percent lower maximum wheel speed with only approximately 2 percent higher energy consumption. The results are the same whether the weight matrix A is given by $A = I$ or $A = M$.

7.2.2.1.5 Failure Conditions Study

Several simulations were performed to study the effects caused by magnetic coil or reaction wheel failures. The results are summarized in Table 7-5. Three conclusions can be reached:

1. The detected coil failure does not cause high wheel speeds, but a great deal of additional energy has to be spent to keep the wheel speed down.

2. The detected wheel failure strongly degrades the momentum management. The maximum wheel speed remains near 10 hertz through the four-orbit period, when normally it can be brought down to 6.8 hertz.

3. Undetected coil failure causes slightly higher wheel speed than detected coil failure.

7.2.2.1.6 Initial Conditions Study

A study was performed to analyze the time required to bring the reaction wheel speed down from different initial conditions. The results are shown in Table 7-6.

7.2.2.2 Performance of Open-Loop Control Laws

The study results for the open-loop control laws are summarized below. In all studies, the nominal momentum profile \vec{H}_{NOM} is generated with a half-orbit desaturation period, whereas the desaturation period and updating frequency used

Table 7-5. Effects on Closed-Loop Control Laws
Due to Coil and Wheel Failures

COIL NUMBER FAILED	WHEEL NUMBER FAILED	DETECTED/ UNDETECTED	ω_{\max} (Hz)				E
			ORBIT 1	ORBIT 2	ORBIT 3	ORBIT 4	
0	0	—	9.2	9.0	6.8	6.6	443
1	0	D	9.2	9.0	6.8	6.8	1080
2	0	D	9.2	9.0	6.8	6.8	1170
0	1	D	12.8	10.4	10.0	10.8	667
0	2	D	10.4	12.0	10.0	10.0	484
1	1	D	12.8	10.4	10.0	10.8	1200
1	0	U	11.2	9.6	6.8	7.8	947

7081/01

Table 7-6. Initial Conditions Study for Closed-Loop Control Laws

STARTING \vec{H}_{RW} X, Y, Z COMPONENTS (Kg · m ² · s ⁻¹)	STARTING ω_{max} (Hz)	TIME REQUIRED TO REDUCE ω_{max} TO BELOW 10 Hz (SECONDS)
20.0	12.0	100
30.0	17.6	400
50.0	28.8	600

7081/01

in the control law are 600 seconds and 200 seconds, respectively. All simulation results are generated from a two-orbit period.

7.2.2.2.1 Geometry Study

In general, the performance of an open-loop control law is not very sensitive to the geometrical conditions. The energy consumption depends on the magnitude of the secular term of the gravity-gradient torque and the strength of the geomagnetic field. The maximum wheel speed is controlled by the periodic component of the gravity-gradient torque and the relative directions between this term and the commanded magnetic torque.

Tables 7-7 and 7-8 compare the maximum wheel speed (ω_{\max}) and the energy consumption (E) during a two-orbit period for different orbit types and attitude parameters. Table 7-7 compares the two orbit types, using simulation results obtained from different attitudes and minimization criteria. On the average, orbit type B gives approximately 9 percent higher ω_{\max} but uses approximately 10 percent less energy than orbit type A. Orbit type B uses less energy because of the greater strength of the geomagnetic field encountered. It gives higher ω_{\max} because of the larger directional variation in the geomagnetic field (see Figure 7-1). This causes the commanded magnetic torque to have a larger directional variation and, therefore, a greater chance to be in phase with the periodic component of the gravity-gradient torque.

Table 7-8 compares the two attitude types at $\beta = 45$ degrees and $\beta = 35.3$ degrees using simulation results obtained from different orbit types, λ angles, and minimization criteria. On the average, $\beta = 45$ degrees gives about 11 percent lower ω_{\max} while using about 5 percent more energy than $\beta = 35.3$ degrees. This result

Table 7-7. Comparison of Open-Loop Control Law Performance for Different Orbit Geometries

CONTROL LAW ID ^a	β ANGLE (DEG)	λ ANGLE (DEG)	ω_{\max} (Hz)		E	
			ORBIT TYPE A	ORBIT TYPE B	ORBIT TYPE A	ORBIT TYPE B
4	35.3	0	7.4	8.2	189	151
		90	8.4	9.6	193	169
		180	10.8	10.8	207	186
	45	0	7.4	7.6	194	161
		90	7.8	8.6	197	177
		180	9.0	10.4	215	197
5	35.3	0	6.4	6.8	228	187
		90	8.4	11.2	263	255
		180	10.0	9.0	250	248
	45	0	5.9	6.5	247	212
		90	7.8	9.6	273	271
		180	8.0	7.6	261	259
MEAN VALUE			8.1	8.8	226	206
PERCENTAGE DIFFERENCE			8.6%		9.7%	

7081/81

^aREFER TO TABLE 5-3.

Table 7-8. Comparison of Open-Loop Control Law Performance for Different Attitude Geometries

CONTROL LAW ID ^a	ORBIT TYPE	λ ANGLE (DEG)	ω_{\max}		E	
			$\beta = 35.3^\circ$	$\beta = 45^\circ$	$\beta = 35.3^\circ$	$\beta = 45^\circ$
4	A	0	7.4	7.4	189	194
		90	8.4	7.8	193	197
		180	10.8	9.0	207	215
	B	0	8.2	7.6	151	161
		90	9.6	8.6	169	177
		180	10.8	10.4	186	197
5	A	0	6.4	5.9	228	247
		90	8.4	7.8	263	273
		180	10.0	8.0	250	261
	B	0	6.8	6.5	187	212
		90	11.2	9.6	255	271
		180	9.0	7.6	248	259
MEAN VALUE			8.9	8.0	211	222
PERCENTAGE DIFFERENCE			11.3%		5.2%	

^aREFER TO TABLE 5.3.

7081/81

is as expected because ω_{\max} is dominated by the magnitude of the periodic term of \vec{T}_{GG} , whereas the energy consumption is dominated by that of the secular term of \vec{T}_{GG} .

7.2.2.2.2 Minimization Criteria Study

Table 7-9 compares the current ME law, which minimizes the energy (control law 4 of Table 5-3) and an alternative open-loop control law, which minimizes the reaction wheel speed caused by the secular term of \vec{T}_{GG} (control law 5 of Table 5-3). From an average of 12 different geometries, the former gives approximately 9 percent higher ω_{\max} than the latter, with an energy savings of approximately 32 percent.

7.2.2.2.3 Failure Condition and Modeling Error Study

A set of simulation studies was performed to examine the effects on the open-loop control laws due to various failure conditions and modeling errors. The conclusions are summarized below:

1. One detected coil failure does not affect the wheel speed but almost doubles energy consumption.
2. One undetected coil failure causes approximately a 20-percent increase in ω_{\max} and a 200-percent to 300-percent increase in energy.
3. Neglect of orbit perturbation in open-loop calculation has negligible effect.
4. One detected wheel failure causes about a 50-percent increase in ω_{\max} with the same amount of energy consumption.
5. A geomagnetic field modeling error due to the difference between the second- and the eighth-order spherical harmonics representation causes a 24-percent increase in ω_{\max} and a 27-percent increase in energy.

Table 7-9. Comparison of Open-Loop Control Law Performance With Different Minimization Criteria

ORBIT TYPE	β ANGLE (DEG)	λ ANGLE (DEG)	ω_{\max} (Hz)		E	
			CONTROL LAW NO. 4	CONTROL LAW NO. 5	CONTROL LAW NO. 4	CONTROL LAW NO. 5
A	35.3	0	7.4	6.4	189	228
		90	8.4	8.4	193	263
		180	10.8	10.0	207	250
	45.0	0	7.4	5.9	194	247
		90	7.8	7.8	197	273
		180	9.0	8.0	215	261
B	35.3	0	8.2	6.8	151	187
		90	9.6	11.2	169	255
		180	10.8	9.0	186	248
	45.0	0	7.6	6.5	161	212
		90	8.6	9.6	177	271
		180	10.4	7.6	197	259
MEAN VALUE			8.8	8.1	186	246
PERCENTAGE DIFFERENCE			8.6%		32.3%	

7081/81

6. For an approximately 10 percent systematic error in \vec{B} superimposed on another 10 percent random noise, ω_{\max} increases by about 50 percent and energy consumption increases by about 130 percent.

7.2.2.2.4 Initial Conditions Study

To study the sensitivity of the control law to the initial conditions, simulations were performed to analyze the time required to settle the reaction wheel speed from different starting values. These results are shown in Table 7-10.

Table 7-10. Initial Conditions Study for Open-Loop Control Laws

Starting H_W X, Y, Z Components ($\text{kg} \cdot \text{m}^2 \cdot \text{s}^{-1}$)	Starting ω_{\max} (Hz)	Time Required To reduce ω_{\max} to Below 10 Hz (sec)
20.0	12.0	300
30.0	17.6	400
50.0	28.8	600

7.2.2.3 Performance of Mixed-Mode Control Laws

The study results for the mixed-mode control laws are summarized in a manner analogous to that for the open-loop control laws. In all studies, the nominal momentum profile is generated with a half-orbit desaturation period, and the time interval Δt used in calculating the desired torque \vec{T}_D (see Equation (5-4)) is fixed at 200 seconds. The updating frequency of \vec{T}_D and the magnetic dipole commands is set to 50 seconds. The time length of each simulation is two orbits.

7.2.2.3.1 Geometry Study

The performance of the mixed-mode control laws on attitude is nearly independent of the orbit type. Table 7-11 compares the two orbit types for various attitudes and minimization criteria.

The dependence of the performance of the mixed-mode control laws on attitude is controlled by the relative magnitudes between the periodic and the secular terms of the gravity-gradient torque. In general, high ω_{\max} results when the periodic term of \vec{T}_{GG} is large, and more energy is consumed when the secular term is large. Table 7-12 compares performance when $\beta = 45$ degrees and 35.3 degrees. As expected, the former gives 12 percent lower ω_{\max} while using 10 percent more energy.

7.2.2.3.2 Minimization Criteria Study

Table 7-13 compares the two minimization criteria: one minimizes the energy (ME) and one minimizes the reaction wheel speed caused by the secular term of \vec{T}_{GG} (MWS). From an average of 12 different geometries, the ME law gives 20 percent higher ω_{\max} while using 30 percent less energy than the MWS law.

7.2.2.3.3 Failure Conditions and Modeling Error Study

The failure conditions and modeling errors exercised in the mixed-mode law are the same as those exercised in the open-loop law. The same conclusions as in the open-loop law were obtained for the first four failure conditions. However, the last two conclusions regarding the effects due to geomagnetic field modeling errors are quite different for the mixed-mode control law. The geomagnetic field modeling error due to the difference between the second and the eighth-order spherical harmonics representation causes a 9-percent increase in ω_{\max} and an 8-percent increase in

Table 7-11. Comparison of Mixed-Mode Control Law Performance for Different Orbit Geometries

MINIMIZATION CRITERIA	β ANGLE (DEG)	λ ANGLE (DEG)	ω_{\max} (Hz)		E^*	
			ORBIT TYPE A	ORBIT TYPE B	ORBIT TYPE A	ORBIT TYPE B
ME	35.3	0	8.6	9.0	154	149
		90	13.6	14.0	143	137
		180	8.4	7.6	139	145
	45.0	0	7.1	8.8	165	161
		90	12.0	12.4	154	148
		180	8.0	7.2	154	158
MWS	35.3	0	7.7	6.8	214	207
		90	10.8	11.2	157	165
		180	8.4	6.9	165	211
	45.0	0	6.3	6.0	249	214
		90	9.4	10.0	173	187
		180	7.2	6.5	190	236
MEAN VALUE			9.0	8.9	172	177
PERCENTAGE DIFFERENCE			1.1%		2.9%	

7081/01

Table 7-12. Comparison of Mixed-Mode Control Law Performance for Different Attitude Geometries

MINIMIZATION CRITERIA	ORBIT TYPE	λ ANGLE (DEG)	ω_{\max}		E	
			$\beta = 35.3^\circ$	$\beta = 45^\circ$	$\beta = 35.3^\circ$	$\beta = 45^\circ$
ME	A	0	8.6	7.1	154	165
		90	13.6	12.0	143	154
		180	8.4	8.0	139	154
	B	0	9.0	8.8	149	161
		90	14.0	12.4	137	148
		180	7.6	7.2	145	158
MWS	A	0	7.7	6.3	214	249
		90	10.8	9.4	157	173
		180	8.4	7.2	165	190
	B	0	6.8	6.0	207	214
		90	11.2	10.0	165	187
		180	6.9	6.5	211	236
MEAN VALUES			9.4	8.4	166	183
PERCENTAGE DIFFERENCE			11.9%		10.2%	

7081/81

Table 7-13. Comparison of Mixed-Mode Control Law Performance With Different Minimization Criteria

ORBIT TYPE	β ANGLE (DEG)	λ ANGLE (DEG)	$\omega_{\max}^{(Hz)}$		E	
			ME	MWS	ME	MWS
A	35.3	0	8.6	7.7	154	214
		90	13.6	10.8	143	157
		180	8.4	8.4	139	165
	45.0	0	7.1	6.3	165	249
		90	12.0	9.4	154	173
		180	8.0	7.2	154	190
B	35.3	0	9.0	6.8	149	207
		90	14.0	11.2	137	165
		180	7.6	6.9	145	211
	45.0	0	8.8	6.0	161	214
		90	12.4	10.0	148	187
		180	7.2	6.5	158	236
MEAN VALUES			9.7	8.1	151	197
PERCENTAGE DIFFERENCE			19.8%		30.5%	

7081/81

E, whereas the 10-percent systematic plus 10-percent random error in \vec{B} has essentially no effect on the mixed-mode law performance. These results may be compared with those from the open-loop law (Section 7.2.2.2): a 24-percent increase in ω_{\max} and a 27-percent increase in E due to modeling errors; a 50-percent increase in ω_{\max} and a 130-percent increase in E due to errors in \vec{B} .

7.2.2.3.4 Initial Conditions Study

As for the closed-loop and open-loop control laws, the initial conditions study for the mixed-mode law was performed by analyzing the time required to reduce the reaction wheel speed to below 10 hertz from various starting values. These results are shown in Table 7-14.

Table 7-14. Initial Conditions Study for Mixed-Mode Control Laws

Starting H_W X, Y, Z Components ($\text{kg} \cdot \text{m}^2 \cdot \text{s}^{-1}$)	Starting ω_{\max} (Hz)	Time Required To reduce ω_{\max} to Below 10 Hz (sec)
20	12.0	50
30	17.6	200
50	28.8	350

7.2.2.4 Comparison of Control Laws

In this subsection, the mixed-mode control law is first compared with the open-loop control law under nominal conditions with the same minimization criteria. Then the performance of a mixed-mode law (i.e., the mixed-mode MWS law) is compared with the current ME and CP laws for both nominal and abnormal conditions.

Tables 7-15 and 7-16 gives the comparison between the mixed-mode and the open-loop control laws for ME and MWS

Table 7-15. Comparison of the Mixed Mode Law With the Open-Loop Under Nominal Conditions With ME Criterion

ORBIT TYPE	β ANGLE (DEG)	λ ANGLE (DEG)	ω_{\max}		E	
			OPEN- LOOP	MIXED- MODE	OPEN- LOOP	MIXED- MODE
A	35.3	0	7.4	8.6	189	154
		90	8.4	13.6	193	143
		180	10.8	8.4	207	139
	45.0	0	7.4	7.1	194	165
		90	7.8	12.0	197	154
		180	9.0	8.0	215	154
B	35.3	0	8.2	9.0	151	149
		90	9.6	14.0	169	137
		180	10.8	7.6	186	145
	45.0	0	7.6	8.8	161	161
		90	8.6	12.4	177	148
		180	10.4	7.2	197	158
MEAN VALUE			8.8	9.7	186	151
PERCENTAGE DIFFERENCE			10.2%		23.2%	

7081/81

Table 7-16. Comparison of the Mixed-Mode Law With the Open-Loop Law Under Nominal Conditions With MWS Criterion

ORBIT TYPE	β ANGLE (DEG)	λ ANGLE (DEG)	ω_{\max}		E	
			OPEN- LOOP	MIXED- MODE	OPEN- LOOP	MIXED- MODE
A	35.3	0	6.4	7.7	228	214
		90	8.4	10.8	263	157
		180	10.0	8.4	250	165
	45.0	0	5.9	6.3	247	249
		90	7.8	9.4	273	173
		180	8.0	7.2	261	190
B	35.3	0	6.8	6.8	187	207
		90	11.2	11.2	255	165
		180	9.0	6.9	248	211
	45.0	0	6.5	6.0	212	214
		90	9.6	10.0	271	187
		180	7.6	6.5	259	236
MEAN VALUE			8.1	8.1	246	197
PERCENTAGE DIFFERENCE			0%		24.9%	

7081/81

criteria, respectively. Twelve different geometries under nominal situations were simulated. The averaged results show that under the same conditions the mixed-mode law is, in general, superior to the open-loop law because it saves a great deal of energy with equal or slightly higher ω_{\max} . Table 7-17 compares the mixed-mode MWS law with the current ME law under nominal conditions. From an average of 12 different orbit and attitude geometries, the mixed-mode MWS law reduces the maximum wheel speed by 9 percent, at an expense of 6 percent more energy. In general, the performance of the mixed-mode MWS law is comparable with the current ME law under nominal conditions. The former gives slightly lower ω_{\max} but uses slightly more energy. However, when modeling errors or abnormal conditions exist, the mixed-mode law performance is superior to the current ME law. This can be seen by a direct comparison of the conclusions given in Sections 7.2.2.2.3 and 7.2.2.3.3.

Figures 7-17 and 7-18 show typical comparisons among the three control laws. In Figure 7-17, the maximum wheel speed and energy consumption resulting from the three control laws are compared under nominal and error conditions of different severity. The sample error conditions selected are the modeling errors on the geomagnetic field \vec{B} . Figure 7-17(a) shows the nominal condition where the measured and the calculated geomagnetic fields are identical. In Figure 7-17(b), the measured geomagnetic field has about 10 percent systematic error plus another 10 percent random error. Similar errors exist in the case of Figure 7-17(c) except that the magnitude of the errors is about 20 percent. The following conclusions can be obtained from Figure 7-17.

1. Under nominal conditions, the current ME law uses the least amount of energy, whereas the mixed-mode MWS law provides the lowest ω_{\max} .

Table 7-17. Comparison of the Mixed-Mode MWS Law With the Current ME Law Under Nominal Conditions

ORBIT TYPE	β ANGLE (DEG)	λ ANGLE (DEG)	ω_{\max} (Hz)		E	
			MIXED-MODE MWS	CURRENT ME	MIXED-MODE MWS	CURRENT ME
A	35.3	0	7.7	7.4	214	189
		90	10.8	8.4	157	193
		180	8.4	10.8	165	207
	45.0	0	6.3	7.4	249	194
		90	9.4	7.8	173	197
		180	7.2	9.0	190	215
B	35.3	0	6.8	8.2	207	151
		90	11.2	9.6	165	169
		180	6.9	10.8	211	186
	45.0	0	6.0	7.6	214	161
		90	10.0	8.6	187	177
		180	6.5	10.4	236	197
MEAN VALUE			8.1	8.8	197	186
PERCENTAGE DIFFERENCE			8.6%		5.9%	

7081/81

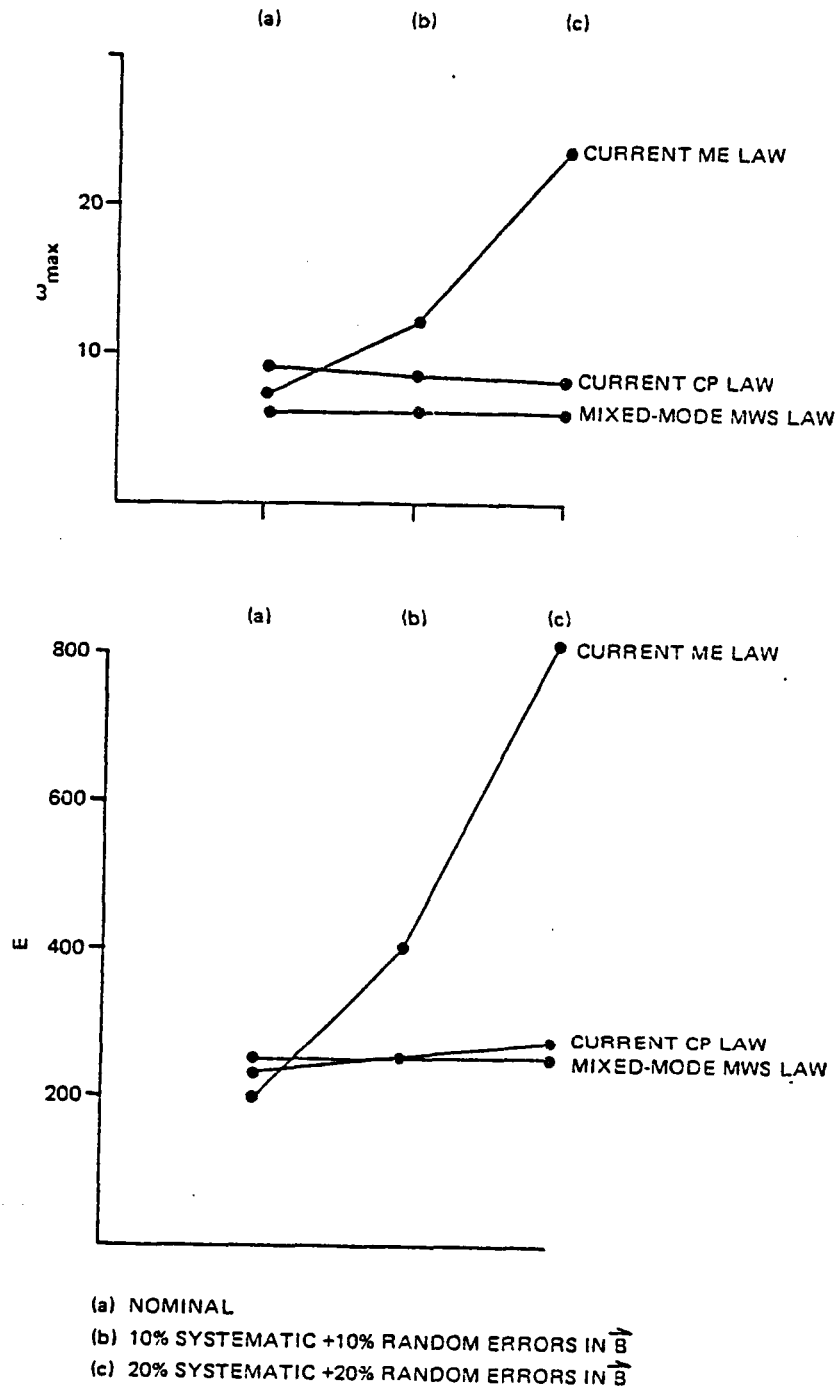
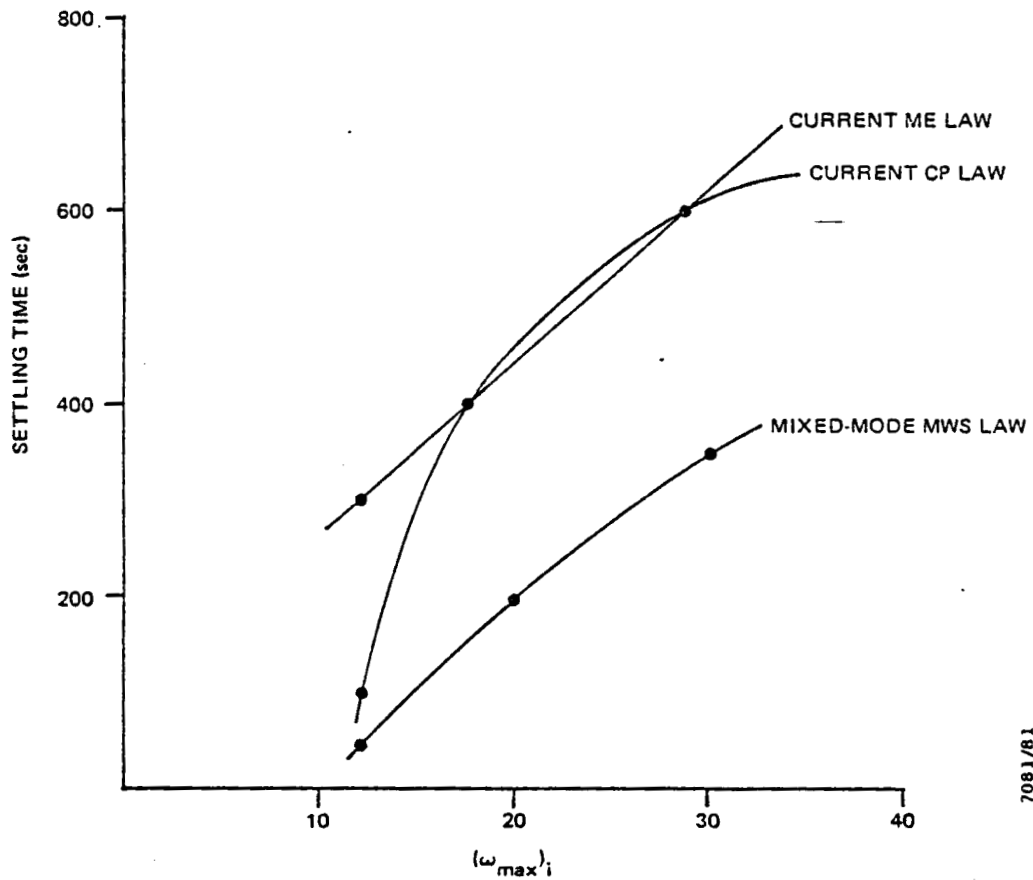


Figure 7-17. Comparison of Control Laws Under Nominal and Error Conditions



7081/81

Figure 7-18. Comparison of Wheel Speed Settling Times Required by Different Control Laws

2. When error conditions exist, the current ME law is very sensitive to the errors and gives very poor performance, whereas both the current CP law and the mixed-mode MWS law are nearly independent of the error conditions.

3. A comparison of the current CP law and the mixed-mode MWS law shows that the two laws use approximately the same amount of energy but the latter always provides much lower ω_{\max} .

Figure 7-18 compares the settling time required by the three control laws for different starting reaction wheel speeds. The settling time in Figure 7-18 is defined as the time required to reduce the maximum reaction wheel speed to below 10 hertz from given starting values. It can be seen from Figure 7-18 that settling time is much shorter for the mixed-mode law than for the two current control laws.

As a conclusion, the simulation results indicate that mixed-mode MWS laws seem to be superior to the two current ST control laws in many respects. Mixed-mode control laws could be implemented for a minimum energy criterion. Under failure conditions, it is expected that the minimization criterion used is not as important as the frequency of updates. This is in agreement with our physical understanding of the control laws.

7.2.3 PERFORMANCE OF CONTROL LAWS DURING MANEUVERS

This subsection presents simulation results for a series of maneuvers from one inertial attitude to another. The 15 maneuvers simulated are listed in Table 7-18. This table lists the initial and final attitudes in terms of the rotation angle λ and β defined in Figure 7-2. (Angle $\phi = 0$ in all cases.) Table 7-18 also gives the total maneuver angle about the eigenaxis for each case. Each maneuver is characterized by constant acceleration for

Table 7-18. Simulated Maneuvers

MANEUVER	INITIAL ATTITUDE		FINAL ATTITUDE		MANEUVER LENGTH	
	λ_1	β_1	λ_2	β_2	DEGREES	TIME (SEC)
1	0	45	90	45	90	700
2	180	45	270	45	90	700
3	0	45	180	45	180	1300
4	90	45	270	45	180	1300
5	-90	45	90	45	180	1300
6	0	45	90	0	90	700
7	90	45	180	0	90	700
8	0	0	90	45	98.4	756
9	90	0	180	45	90	700
10	0	45	0	-45	90	700
11	90	45	90	-45	90	700
12	180	45	180	-45	90	700
13	0	45	180	-45	180	1300
14	90	45	270	-45	180	1300
15	-90	45	90	-45	180	1300

7081/81

100 seconds, followed by a period of constant angular velocity at 0.15 degree per second, followed by constant deceleration for 100 seconds. Total maneuver times are listed in the last column of Table 7-18.

Initial reaction wheel momentum was determined from calculations of nominal momentum profiles assuming use of the current ME control law. This momentum was distributed among the reaction wheels according to the pseudo-inverse law. Inertial pointing at the initial attitude was simulated for a one-half orbital period, at which time the maneuver was started. Maneuvers of 90 degrees took approximately a one-eighth orbit period to execute, whereas those of 180 degrees took about a one-fourth orbital period.

All 15 maneuvers listed in Table 7-18 were simulated using the current CP control law for orbits of both type A (minimum separation of the orbital and geomagnetic poles) and type B (maximum separation). Orbit type A passes through the South Atlantic Anomaly (SAA) between orbital phases 0.85 and 0.90, i.e., about 0.2 of an orbit following a 90-degree maneuver or 0.1 of an orbit following a 180-degree maneuver. Orbit type B avoids the SAA entirely. The maximum and minimum wheel speeds occurring between the end of the maneuver and the end of the orbital period are given in columns 2 through 5 in Table 7-19 for the CP law simulations. As expected, the mean and standard deviations of the extreme wheel speeds following maneuvers were larger for orbit type A where the small strength and variation of the geomagnetic field result in less control. Energy consumption for the entire orbit (in units defined in Section 7.2.2) is given in columns 2 and 3 of Table 7-20 for the CP law simulations. In the majority of cases, energy consumption is larger for orbit type A.

Table 7-19. Reaction Wheel Speed Following Maneuvers

MANEUVER	CP LAW		ME LAW		
	ORBIT A $\omega_{\text{max, min}}$	ORBIT B $\omega_{\text{max, min}}$	ORBIT A $\omega_{\text{max, min}}$	ORBIT B $\omega_{\text{max, min}}$	$T_{\text{MAN}} = 0.75P$ $\omega_{\text{max, min}}$
1	14.4 -7.2	6.4 -3.8	8.0 -6.5	8.8 -6.4	
2	4.0 -1.6	1.0 -1.5	5.0 -6.5		
3	13.6 -6.4	5.0 -5.0	5.5 -4.5		
4	2.8 -12.4	4.0 -2.0	10.4 -5.6		
5	6.0 -13.5	4.4 -6.4	9.0 -7.0		
6	12.5 -2.5	10.0 -7.5	13.6 -6.4		
7	2.4 -15.2	8.8 -1.6	3.5 -11.0		
8	16.8 -8.0	8.0 -8.8	12.8 -6.4	6.4 -6.4	
9	4.5 -13.5	4.5 -7.5	9.6 -12.8		
10	6.4 -6.4	0.8 -6.4	5.6 -5.6		
11	4.0 -1.6	3.2 -0.8	6.4 -4.0	4.8 -7.2	4.0 -7.2
12	4.8 -12.0	6.4 -6.4	5.6 -6.4		4.8 -2.4
13	15.2 -10.4	7.5 -7.0	4.8 -8.0		8.0 -8.0
14	17.0 -34.0	6.5 -6.5	8.0 -8.0		6.4 -13.2
15	0.8 -6.8	1.2 -6.0	8.8 -3.7		9.8 -3.0
MEAN σ	8.3 -10.1 ± 5.8 7.9	5.2 -5.5 ± 2.8 2.7	7.8 -6.8 ± 3.0 2.5		

7081/81

Table 7-20. Energy Consumption for Maneuvers

MANEUVER	CP LAW		ME LAW		
	ORBIT A	ORBIT B	ORBIT A	ORBIT B	$T_{MAN} = 0.75P$
1	260	209	131		
2	140	88	138		
3	212	174	111	67	
4	263	116	136		
5	102	110	156		
6	101	127	89		
7	91	129	92		
8	210	146	158		
9	73	69	107		
10	125	82	86	80	
11	106	97	86		81
12	152	116	109		70
13	131	129	170	84	189
14	95	99	209	75	172
15	150	125	197		159
MEAN σ	147 ± 61	121 ± 36	132 ± 40		

7081/81

Maneuver 14 (orbit type A) resulted in the largest wheel speeds. This was due to a continuous build-up of the y-component of the gravity-gradient torque during the positive eigenaxis rotation. Smaller maximum and minimum wheel speeds (8.0 and -17.5 hertz, respectively) were obtained when the maneuver was executed with a negative rotation about the eigenaxis. These results indicate that, for long maneuvers, the direction of the rotation is important for minimizing wheel speeds.

Continuation of CP law simulations beyond an orbital period clarified our understanding of the center speed control loop. We found that inclusion of wheel speeds during the maneuver in the center speed calculations resulted in large wheel speed excursions in succeeding half-orbits. Ignoring maneuver wheel speeds in the calculations corrected this anomaly.

All maneuvers for orbit type A were repeated using the current ME law with the lead/lag time set at 500 seconds. The maximum and minimum wheel speeds (columns 6 and 7 of Table 7-19), as well as the energy consumption (column 4 of Table 7-20), were slightly reduced relative to the results obtained for the CP law. Four orbit type B maneuvers were repeated using the current ME law. Energy consumption for the ME law was less (column 5, Table 7-20), but wheel speeds increased for two cases and decreased for the other two (columns 8 and 9, Table 7-19).

The effect of the SAA for ME law maneuvers was investigated by shifting the start of the maneuver to orbital phase 0.75 of orbit type A. Under these conditions, maneuvers 11 and 12 end just as the spacecraft is entering the SAA, and maneuvers 13 through 15 extend through the SAA. The results are presented in the final columns of Tables 7-19 and 7-20. (Maximum and minimum wheel speeds are for the entire

half-orbit following the maneuver in cases 13 through 15.) For the five maneuvers, mean energy consumption is reduced, but slightly higher wheel speeds are obtained.

It had been concluded in previous studies (Section 4.1) that there are two unfavorable track segments for momentum management. Orbit type A includes one of these: longitude 240 to 340 degrees with spacecraft longitude increasing. This region is traversed from about phase 0.67 to phase 0.95 in orbit type A. Our results confirm that momentum management (wheel speed minimization) is generally more difficult in this region than elsewhere (specifically, orbit type B, which traverses neither region).

Time permitted only a few studies of maneuvers under abnormal conditions and comparisons with the mixed-mode MWS law described in Section 5. Maneuver 1, orbit type A, was repeated for the mixed-mode law, using a 1000-second lead time instead of the half-orbit specified in Section 5. Maximum and minimum wheel speeds following the maneuver and energy consumption for the orbit are compared with the earlier results from the CP and ME control laws in column 3 of Table 7-21. The performances of the mixed-mode and ME control laws are much better than that of the CP, with the mixed-mode law yielding a slightly smaller range of wheel speeds but using slightly more energy. Undetected failure of reaction wheel 1 (with constant $\omega = 5.6$ hertz) was simulated. The ME law performance was the worst, with double the wheel speed range and four times the energy consumption compared to normal conditions (column 4, Table 7-21). The performances of the CP and mixed-mode laws were better, presumably because of their closed-loop characteristics. Simulation results of a detected failure of wheel 1 (constant $\omega = 0$ hertz) are given in column 5, Table 7-21. As was the case for normal conditions, the ME and mixed-mode laws

Table 7-21. Maneuvers Under Abnormal Conditions
(Maneuver 1, Orbit Type A)

LAW	PARAMETERS	CONDITIONS			
		NORMAL	WHEEL FAILURE		\vec{B} NOISE
			UNDETECTED	DETECTED	
CP	ω_{\max}	14.4	9.6	19.5	15.2
	ω_{\min}	-7.2	-13.6	-21.0	-5.6
	E	260	284	344	314
ME	ω_{\max}	8.0	16.8	11.0	8.0
	ω_{\min}	-6.5	-13.6	-11.0	-6.5
	E	131	573	131	245
MM	ω_{\max}	6.0	7.5	11.2	4.5
	ω_{\min}	-8.0	-12.5	-12.0	-9.5
	E	149	324	152	206

7081/81

produced smaller ranges in wheel speeds, but the mixed-mode law used more energy. The final column of Table 7-21 lists the results when the noise and bias described in Section 7.2.2 were added to \vec{B} . Again, the ME and mixed-mode law performances are superior, with the mixed-mode law yielding both smaller wheel speeds and decreased energy consumption.

General conclusions that may be drawn from these maneuver studies include the following:

- The increased difficulty of momentum management during SAA passage is confirmed.
- The ME law is generally superior to the CP law in minimizing both wheel speeds and energy consumption.
- The performances of the ME and mixed-mode control laws are similar under normal conditions, but the mixed-mode law is superior in the presence of certain undetected failures.

REFERENCES

- 7-1. Myron A. Shear, "Utility Subroutines," Spacecraft Attitude Determination and Control, ed. James R. Wertz. Dordrecht, Holland: D. Reidel Publishing Company, 1978
- 7-2. National Aeronautics and Space Administration, NASA SP-3054, World Maps of Constant B, L, and Flux Contours, E. G. Stassinopoulos, 1970

APPENDIX A - DERIVATION OF MINIMUM WHEEL SPEED LAWS

This appendix presents a more general derivation of control laws based on a minimum wheel speed criterion that includes the current CP law equations. In this derivation, the assumed relation between \vec{T}_M and \vec{T}_D as given in Equation (2-13) is not required. In addition, an open-loop law is presented that is based on a minimum wheel speed criterion.

The current CP law is a closed-loop control law that minimizes the reaction wheel speed. As shown in Equation (2-15), the reaction wheel speed is minimized when

$$\mathcal{L} = \vec{H}_{RW}^T Q \vec{H}_{RW} \quad (A-1)$$

is minimized, where $Q = (\vec{W}W^T)^{-1}$. From Equation (2-3),

$$\begin{aligned} \vec{H}_{RW}(t_f) &= \vec{H}_{RW}(t_i) + \int_{t_i}^{t_f} (\vec{T}_M + \vec{T}_{GG}) dt \\ &= \left[\vec{H}_{RW} + \Delta t (\vec{T}_M + \vec{T}_{GG}) \right]_{t=t_i} \end{aligned}$$

or

$$\frac{1}{\Delta t} \vec{H}_{RW}(t_f) = \frac{1}{\Delta t} \vec{H}_{RW}(t_i) + \vec{T}_M(t_i) + \vec{T}_{GG}(t_i) \quad (A-2)$$

Substituting Equation (2-12) into Equation (A-2) with $K_M = \frac{1}{\Delta t}$ and $\vec{H}_T = \vec{H}_{RW}$ (which is true for the inertial case) gives

$$\frac{1}{\Delta t} \vec{H}_{RW}(t_f) = (\vec{T}_M - \vec{T}_D)_{t=t_i} \quad (A-3)$$

Thus, by substituting Equation (A-3) into Equation (A-1), the reaction wheel speed is minimized when

$$\mathcal{L}' = (\vec{T}_M - \vec{T}_D)^T Q (\vec{T}_M - \vec{T}_D) \quad (A-4)$$

is minimized, where \vec{T}_M is the magnetic torque and \vec{T}_D is a desired torque given by Equation (2-12) at inertial attitudes.

Thus, the problem of deriving the current CP law reduces to the problem of deriving an expression for \vec{T}_M that minimizes the quantity defined in Equation (A-4) and at the same time satisfies the condition that \vec{T}_M is perpendicular to the geomagnetic field \vec{B} . That is,

$$\vec{B}^T \vec{T}_M = 0 \quad (A-5)$$

Applying the method of Lagrange multipliers, the quantity f is first defined as the following:

$$f = \frac{1}{2} (\vec{T}_M - \vec{T}_D)^T Q (\vec{T}_M - \vec{T}_D) + \lambda \vec{B}^T \vec{T}_M \quad (A-6)$$

where λ is the Lagrange multiplier.

Then the partial derivative of f with respect to T_M is set to zero. That is,

$$\frac{\partial f}{\partial T_M} = Q (\vec{T}_M - \vec{T}_D) + \lambda \vec{B} = \vec{0}$$

$$\vec{T}_M = \lambda \vec{B}' + \vec{T}_D \quad (A-7)$$

where

$$\vec{B}' = Q^{-1} \vec{B} = WW^T \vec{B} \quad (A-8)$$

By combining Equations (A-7) and (A-5), the following is derived:

$$\begin{aligned} \vec{T}_M &= - \frac{\vec{B} \cdot \vec{T}_D}{\vec{B} \cdot \vec{B}'} \vec{B}' + \vec{T}_D \\ &= \vec{B} \times \left(\vec{B}' \times \frac{-\vec{T}_D}{\vec{B} \cdot \vec{B}'} \right) \end{aligned} \quad (A-9)$$

$$\begin{aligned} &= - \vec{B} \times \vec{\mu}_M \\ &= \frac{\tilde{\vec{B}}^T \tilde{\vec{B}}' \vec{T}_D}{\vec{B} \cdot \vec{B}'} \end{aligned} \quad (A-10)$$

Thus, given any desired torque, \vec{T}_D , the magnetic torque, \vec{T}_M , which minimizes the expression in Equation (A-4) is unique. The magnetic moment that produces this magnetic torque is not unique, since there are an infinite number of solutions to

$$\vec{T}_M = -\vec{B} \times \vec{\mu}_M$$

given \vec{T}_M and \vec{B} . One solution, by inspection, is to let

$$\vec{\mu}_M = \frac{\vec{B}' \times \vec{T}_D}{\vec{B} \cdot \vec{B}'} \quad (A-11)$$

which is the expression used in the current CP law.

In general, this solution does not minimize the magnitude of the magnetic moment nor the torquer current. These solutions can be obtained by using pseudo-inverse theory to solve

$$\vec{T}_M = -\tilde{B} \vec{\mu}_M = -\tilde{B} M \vec{\mu}_T \quad (A-12)$$

for $\vec{\mu}_M$ and $\vec{\mu}_T$, respectively. In particular,

$$\vec{\mu}_M = \frac{\vec{B} \times \vec{T}_M}{\vec{B} \cdot \vec{B}} \quad (A-13)$$

is the solution that minimizes the magnitude of $\vec{\mu}_M$.

This law, like all closed-loop laws, cannot remove all the secular torque in a given desaturation interval, since only that component perpendicular to \vec{B} can be removed at any given time. It also attempts to remove the cyclic torque which is inefficient.

Based upon the experience of the ME law, which uses a constant costate vector, the minimum wheel speed closed-loop law can be made open loop by requiring that the desired torque, \vec{T}_D , remain constant over the interval and also satisfy the condition that

$$\int \vec{T}_M dt = - \int \vec{T}_{CG} dt \quad (A-14)$$

Substituting the expression in Equation (A-10) for T_M gives an equation for T_D that is easily solved.

Integration of this equation over half-orbit periods eliminates the cyclic terms and produces a constant desired torque that is proportional to the secular torque weighted by the magnetic field geometry and the minimum wheel speed criterion.

The scalar denominator, $\vec{B} \cdot \vec{B}'$, in Equation (A-10) does not vary significantly for the ST orbit. Thus, instead of requiring T_D to remain constant, require

$$\vec{P} = \vec{T}_D / \vec{B} \cdot \vec{B}' \quad (A-15)$$

to be constant and solve the boundary condition above for \vec{P} . This yields control law 5 of Table 5-3.

Control law 5 is an open-loop law with a minimum wheel speed criterion applied to the secular torque. The simulation results of Section 7 show that this law indeed produces lower wheel speeds on the average while using very little more energy than the ME law.

APPENDIX B - NAMELISTS

This appendix describes the NAMELISTs for the FORTRAN computer programs developed by CSC for analytical studies of ST momentum management. Table B-1 describes NAMELIST /INPUT/ for the nominal momentum profile utility, HNOM. Table B-2 describes NAMELIST /SIMPRM/ for the ST Onboard Control Simulator (STOCLS).

Table B-1. NAMELIST /INPUT/ (1 of 2)

PARAMETER	TYPE	DESCRIPTION	DEFAULT
TSTART	R*8	START TIME (YYMMDD.HHMMSSMMM)	840311.0029000D0
NINT	I*4	NUMBER OF INTEGRATION INTERVALS	5
MLN	I*4	ORDER OF MAGNETIC FIELD MODEL	8
ICON	I*4	CONTROL FLAG FOR FASTOX: = 0, NO PERTURBATIONS OR VELOCITY = 1, PERTURBATIONS BUT NO VELOCITY	1
TEPOCH	R*8	EPOCH TIME FOR FASTOX (YYMMDD.HHMMSS)	840311.0029000D0
A	R*8	SEMIMAJOR AXIS FOR FASTOX (KILOMETERS)	6878.165D0
E	R*8	ECCENTRICITY FOR FASTOX	0.D0
EYE	R*8	INCLINATION FOR FASTOX	28.8D0
RAN	R*8	RIGHT ASCENSION OF ASCENDING NODE FOR FASTOX (DEGREES)	64.906D0
WO	R*8	ARGUMENT OF PERIGEE FOR FASTOX (DEGREES)	0.D0
EMO	R*8	MEAN ANOMALY AT EPOCH FASTOX (DEGREES)	0.D0
ROTZ, ROTY, ROTX	R*8	ATTITUDE RELATIVE TO ORBITAL FRAME; 3, 2, 1 EULER ROTATION	3*0.D0
XXMOI, YYMOI, ZZMOI, XYMOI, YZMOI, XZMOI	R*8	MOMENT OF INERTIA TENSOR ELEMENTS (KILOGRAMS-METERS ²)	16390.D0 51900.D0 50715.D0 3*0.D0
NF	I*4	ORDER OF FOURIER COEFFICIENTS TO BE CALCULATED (LIMIT IS 2*NINT)	5
NHALF	I*4	NUMBER OF HALF-ORBITS TO PROCESS	1
WEIGHTING MATRIX PARAMETERS			
M1W2A3	I*4	OPTIONS FOR WEIGHTING MATRIX [A]: = 1, USE MAGNETIC COIL MOUNTING MATRIX = 2, USE REACTION WHEEL MOUNTING MATRIX = 3, USER INPUT FOR [A] [A] ^T	1
MMT(9)	R*8	USER INPUT FOR [A] [A] ^T WHEN M1W2A3 = 3	1.D0, 3*0.D0, 1.D0, 3*0.D0, 1.D0
CANG	R*8	MAGNETIC COIL MOUNTING ANGLE (DEGREES)	35.26D0
WANG	R*8	REACTION WHEEL MOUNTING ANGLE (DEGREES)	20.0D0
NCOIL	I*4	NUMBER OF THE DISABLED MAGNETIC COIL: = 0, NONE DISABLED	0
INPUT/OUTPUT			
NWHEEL	I*4	NUMBER OF THE DISABLED REACTION WHEEL: = 0, NONE DISABLED	0
INOUT(20)	I*4	DIAGNOSTIC PRINT LEVELS — INOUT(1): > 0, $1T_{GG}$, $1BMMB^T$, $(1BMM^TB^T)^{-1}$ P AND SPHERICAL COORDINATES	2, 19*0 10 = NO OUTPUT 16 = HIGHEST LEVEL OF OUTPUT

Table B-1. NAMELIST /INPUT/ (2 of 2)

PARAMETER	TYPE	DESCRIPTION	DEFAULT
INOUT(20) CONT'D		<p>> 1, N, t, R, B, T_{GG}, $BMM^T B^T$ + (TMN, TSUM AND SPHERICAL COORDINATES)</p> <p>> 2, PRO, PD</p> <p>> 3, H_{NOM} (FOURIER) - H_{NOM}</p> <p>INOUT(2):</p> <p>> 0, SPHERICAL COORDS FOR \vec{R}, \vec{B}, \vec{T}_{GG}</p> <p>> 1, SPHERICAL COORDS FOR \vec{B}_{GCI}</p> <p>INOUT(7): SUBROUTINE GRAVITY</p> <p>INOUT(8): SUBROUTINE DXFORM (NAMELIST /INPUT/ AND H_{NOM} ALWAYS PRINTED)</p>	
IDUMP	I*4	FORTTRAN UNIT FOR DIAGNOSTICS (NOT IN USE)	6
ITAPE	I*4	FORTTRAN UNIT FOR TAPE (NOT IN USE)	10

18/1872

Table B-2. NAMELIST /SIMPRM/ (1 of 5)

PARAMETER	TYPE	DESCRIPTION	DEFAULT
GENERAL CONTROL AND TRUTH MODEL PARAMETERS			
TSTART	R*8	START TIME (YYMMDD.HHMMSSMMM)	840311.0029000D0
ORBITS	R*8	NUMBER OF ORBITS TO SIMULATE	1.0D0
ICON	I*4	CONTROL FLAG FOR FASTOX: = 0, NO PERTURBATIONS OR VELOCITY = 1, PERTURBATIONS BUT NO VELOCITY	1
TEPOCH	R*8	EPOCH TIME FOR FASTOX (YYMMDD.HHMMSS)	840311.0029000D0
A	R*8	SEMIMAJOR AXIS FOR FASTOX (KILOMETERS)	6878.165D0
E	R*8	ECCENTRICITY FOR FASTOX	0.D0
EYE	R*8	INCLINATION FOR FASTOX	28.8D0
RAN	R*8	RIGHT ASCENSION OF ASCENDING NODE FOR FASTOX (DEGREES)	64.906D0
WO	R*8	ARGUMENT OF PERIGEE FOR FASTOX (DEGREES)	0.D0
EMO	R*8	MEAN ANOMALY AT EPOCH FASTOX (DEGREES)	0.D0
XXMOI, YYMOI, ZZMOI, XYMOI, YZMOI, XZMOI	R*8	MOMENT OF INERTIA TENSOR ELEMENTS (KILOGRAMS-METERS ²)	16390.D0 51900.D0 50715.D0 3*0.D0
MLN	I*4	ORDER OF MAGNETIC FIELD FOR THE TRUTH MODEL	8
RWI(4)	R*8	REACTION WHEEL MOMENTS OF INERTIA (KILOGRAM-METERS ²)	4*0.382D0
CANG	R*8	MAGNETIC COIL MOUNTING ANGLE (DEGREES)	35.26D0
WANG	R*8	REACTION WHEEL MOUNTING ANGLE (DEGREES)	20.0D0
NCOIL	I*4	NUMBER OF THE DISABLED MAGNETIC COIL: = 0, NONE DISABLED	0
NWHEEL	I*4	NUMBER OF THE DISABLED REACTION WHEEL: = 0, NONE DISABLED	0
HMAX	R*8	MAXIMUM SINGLE-WHEEL MOMENTUM (KILOGRAM- METERS ³ -SECONDS ⁻¹)	120.D0
HZERO(3)	R*8	INITIAL MOMENTUM IN RWA SYSTEM WHICH IS DIS- TRIBUTED BY $H_{RW} = W^T(WW^T)^{-1}H$	3*0.D0
NDELT	I*4	SIMULATION STEP SIZE (SECONDS)	1
NUP	I*4	NUMBER OF STEPS BETWEEN UPDATES. NOTE: THE TIME BETWEEN UPDATES = NUP*NDELT	50
NCTRL	I*4	CONTROL LAW TO USE: = 1, UNMODIFIED CP LAW = 2, CLOSED-LOOP LAW = 3, OPEN-LOOP LAW = 4, MIXED-MODE LAW = 5, SIMPLIFIED MIXED-MODE LAW	1
DPMLM	R*8	LIMIT FOR MAGNETIC DIPOLE MOMENT FOR EACH TORQUER (AMPERE-METERS ²)	4000.D0

Table B-2. NAMELIST /SIMPRM/ (2 of 5)

PARAMETER	TYPE	DESCRIPTION	DEFAULT
MCOIL	I*4	NUMBER OF UNDETECTED, DISABLED MAGNETIC COIL: = 0, NONE DISABLED	0
MWHEEL	I*4	NUMBER OF UNDETECTED, DISABLED REACTION WHEEL: = 0, NONE DISABLED	0
COILC	R*8	CONSTANT VALUE OF DIPOLE MOMENT, μ_T , FOR UNDETECTED, DISABLED COIL (MCOIL) (AMPERE-METERS ²)	0.00
WHEELC	R*8	CONSTANT VALUE OF WHEEL SPEED FOR UNDETECTED, DISABLED REACTION WHEEL (HERTZ). IF WHEELC = 0.00, THE INITIAL VALUE DETERMINED FROM H_0 IS KEPT THROUGH THE RUN FOR DISABLED WHEEL (MWHEEL)	0.00
CONTROL LAW PARAMETERS			
GAINM	I*4	GAIN FACTOR FOR UNMODIFIED CP LAW OR CLOSED-LOOP LAW (NCTRL = 1, 2)	1.00
MLNC	I*4	ORDER OF MAGNETIC FIELD FOR CALCULATED FIELD USED IN OPEN-LOOP LAW (NCTRL = 3)	4
MLNO	I*4	ORDER OF MAGNETIC FIELD FOR OBSERVED FIELD USED IN ALL CONTROL LAWS	8
ICONC	I*4	CONTROL FLAG FOR FASTOX USED BY OPEN-LOOP LAW TO CALCULATE POSITION VECTOR: = 0, NO PERTURBATIONS OR VELOCITY = 1, PERTURBATIONS BUT NO VELOCITY	0
M1W2A3	I*4	OPTIONS FOR WEIGHTING MATRIX, [A]: = 1, USE MAGNETIC COIL MOUNTING MATRIX = 2, USE REACTION WHEEL MOUNTING MATRIX = 3, USER INPUT (AMAT)	3
AMAT(12)	I*4	USER WEIGHTING MATRIX, [A] (DEFAULT IS THE IDENTITY MATRIX)	1.00, 3*0.00, 1.00, 3*0.00, 1.00, 3*0.00
OPEN-LOOP CONTROL LAW			
NSAT	I*4	THE LENGTH OF THE DESATURATION INTERVAL (MUST BE A MULTIPLE OF THE UPDATE INTERVAL - NUP*NDLT) IN SECONDS	600
AF(3)	R*8	FOURIER COEFFICIENT, \hat{a} , USED TO CALCULATE NOMINAL MOMENTUM PROFILE	3*0.00
BF(3)	R*8	FOURIER COEFFICIENT, \hat{b} USED TO CALCULATE NOMINAL MOMENTUM PROFILE	3*0.00
NUPME	I*4	TIME BETWEEN DIPOLE MOMENT UPDATES (SECONDS)	50
NUPMX	I*4	DESATURATION PERIOD FOR MIXED-MODE LAW	200

B-5

Table B-2. NAMELIST /SIMPRM/ (3 of 5)

PARAMETER	TYPE	DESCRIPTION	DEFAULT
CLOSED-LOOP CONTROL LAW PARAMETERS			
HNL1	R*8	RW CENTER SPEED CONTROL LOOP FIRST AXIS NONLINEARITIES BREAKPOINT, H_{NL1}	10.200
HNL2	R*8	RW CENTER SPEED CONTROL LOOP SECOND AND THIRD AXES NONLINEARITIES BREAKPOINT, H_{NLR}	19.800
XKP	R*8	FACTOR, K_p , IN CENTER SPEED CALCULATION	2.828D0
XSG	R*8	FACTOR, K_g IN CENTER SPEED CALCULATION	0.06659D0
\$CSMAN	L*1	OPTION TO IGNORE WHEEL SPEEDS DURING MANEUVER FOR CENTER SPEED CONTROL LOOP: = F, IGNORE = T, DO NOT IGNORE	F
NOISE AND BIAS PARAMETERS			
NOFF(8)	I*4	<p>FLAGS INDICATING WHETHER TO APPLY NOISE (0 = NO NOISE, ANY OTHER VALUE = NOISE) TO THE FOLLOWING PARAMETERS:</p> <p>NOFF(1), \vec{H}_{RW}, REACTION WHEEL MOMENTUM USED BOTH IN CLOSED-LOOP AND OPEN-LOOP CONTROL LAWS</p> <p>NOFF(2), \vec{B}, THE OBSERVED VALUE OF THE MAGNETIC FIELD USED IN BOTH CONTROL LAWS</p> <p>NOFF(3), \vec{T}_{TOTAL}, TOTAL TORQUE ON S/C USED IN THE TRUTH MODEL</p> <p>NOFF(4), SPARE</p> <p>NOFF(5), \vec{R}_{CAL}, THE POSITION VECTOR AS CALCULATED BY BOTH CONTROL LAWS</p> <p>NOFF(6), \vec{B}_{CAL}, THE CALCULATED MAGNETIC FIELD VECTOR USED IN THE OPEN-LOOP CONTROL LAW</p> <p>NOFF(7), \vec{T}_{GG}, THE CALCULATED GRAVITY-GRADIENT TORQUE USED IN BOTH CONTROL LAWS</p> <p>NOFF(8), SPARE</p>	<p>0</p> <p>0</p> <p>0</p> <p>0</p> <p>0</p> <p>0</p> <p>0</p> <p>0</p>
NRFLG	I*4	RANDOM NUMBER GENERATOR SPEED (MUST BE A LARGE, POSITIVE, ODD NUMBER) FOR NOISE MODEL	999999
SMEAN(8)	R*4	MEAN VALUE OF NOISE TO BE APPLIED TO EACH OF THE PARAMETERS LISTED IN DESCRIPTION OF NOFF	8*0.0
STDV(8)	R*4	NOISE MODEL STANDARD (1σ) DEVIATION TO BE APPLIED TO EACH OF THE PARAMETERS LISTED IN DESCRIPTION OF NOFF	8*0.0
RBIAS(3)	R*8	BIAS ADDED TO THE SYSTEM MAGNETIC DIPOLE MOMENT VECTOR, \vec{M}_M WHERE $\vec{M}_M = [M] \hat{A}_T$	3*0.00

Table B-2. NAMELIST /SIMPRM/ (4 of 5)

PARAMETER	TYPE	DESCRIPTION	DEFAULT
MANEUVERS			
TMAN	R*8	TIME TO BEGIN MANEUVER (IN NUMBER OF ORBITS SINCE START OF SIMULATION, e.g., 0.5D0 = 1/2 ORBIT \approx 2800 SECONDS); IF NEGATIVE, NO MANEUVER (THIS IS THE ONLY PARAMETER THAT DETERMINES WHETHER OR NOT A MANEUVER IS EXECUTED)	-1.D0
OMGF	R*8	MAXIMUM ANGULAR VELOCITY, ω_f , DURING SLEW (DEGREES PER SECOND)	0.15D0
TACC	R*8	TIME TO ACCELERATE FROM 0 VELOCITY TO ω_f , ALSO TO DECELERATE TO 0 VELOCITY (SECONDS)	100.D0
ROTZ(2), ROTY(2), ROTX(2)	R*8	ATTITUDE RELATIVE TO ORBITAL FRAME: 3, 2, 1 EULER ROTATION ANGLES, RESPECTIVELY. ROTZ(1), ROTY(1), ROTX(1) YIELD INITIAL ATTITUDE; ROTZ(2), ROTY(2), ROTX(2) YIELD FINAL ATTITUDE AFTER MANEUVER	2*0.D0 2*0.D0 2*0.D0
LEAD	I*4	LEAD TIME USED IN OPEN-LOOP LAW (SECONDS)	350
LAG	I*4	LAG TIME USED IN OPEN-LOOP LAW (SECONDS)	350
AF2(3), BF2(3)	R*8	FOURIER COEFFICIENTS USED TO CALCULATE \vec{H}_{NOM} FOLLOWING MANEUVER	3*0.D0, 3*0.D0
PVEC(3)	R*8	COSTATE VECTOR, \vec{P} , FOR THE MIXED-MODE LAW DURING MANEUVER (OBTAINED FROM PREVIOUS EXECUTION OF OPEN-LOOP LAW)	3*0.D0
PRINTER PLOT CONTROLS ^a			
PTINC	R*8	TIME INCREMENT BETWEEN POINTS (SECONDS)	50.D0
MAXL	I*4	MAXIMUM NUMBER OF LINES DESIRED IN GRAPH (VALID RANGE: 3 THROUGH 80)	80
IOPT	I*4	OPTION DESIRED IF TWO OR MORE POINTS FALL IN THE SAME SPACE: = 0, LATER CHARACTERS OVERRIDE EARLIER = 1, INSERT A DIGIT INDICATING NUMBER OF POINTS FALLING IN EACH SPACE	1
XL, XH, YL, YH	R*4	LOWER AND UPPER LIMITS FOR X- AND Y VALUES RESPECTIVELY. IF XL = XH = 0., THEN X-AXIS SCALING IS BASED ON THE MAXIMUM VALUES OF X. IF YL = YH = 0., THEN Y-AXIS SCALING IS BASED ON THE MAXIMUM VALUES OF Y	0., 0., 0., 0.,
INPUT/OUTPUT PARAMETERS			
IDUMP	I*4	FORTRAN UNIT FOR DIAGNOSTIC OUTPUT FROM CONTROL LAW SUBROUTINES	7

^aREFER TO SUBROUTINE GRAPH IN ATTIT.ATTMAIN.UTIL LIBRARY FOR COMPLETE DESCRIPTION OF THESE PARAMETERS.

Table B-2. NAMELIST /SIMPRM/ (5 of 5)

PARAMETER	TYPE	DESCRIPTION	DEFAULT
INOUT(20)	I*4	DIAGNOSTIC PRINT LEVELS: INOUT(1), MAIN PROGRAM, STOCLS INOUT(2), SUBROUTINES ATTINT AND PROP INOUT(3), CONTROL LAW SUBROUTINES CPMOD, ME, OR MM INOUT(4), SUBROUTINE PROPME (PROPAGATION IN ME DURING MANEUVER) INOUT(7), SUBROUTINE GRAVITY INOUT(8), SUBROUTINE DXFORM	2, 19*0 (0 = NO OUTPUT) (6 = HIGHEST LEVEL OF OUTPUT)
ITAPE	I*4	FORTTRAN UNIT FOR TAPE (NOT USED)	10
NPRT	I*4	FORTTRAN UNIT FOR OUTPUT FROM MAIN PROGRAM STOCLS	8
NWRT	I*4	PRINT EVERY NWRTth STEP	10

18/1/87

APPENDIX C - ANALYTICAL APPROXIMATION TO MOMENTUM MANAGEMENT EXPRESSIONS

The momentum profile that is actually realized in a momentum management scheme is a complex function of environmental factors (magnetic field and disturbance torques), the control law, and the interaction of the two. An accurate prediction of the true momentum profile requires rather sophisticated environmental models and computer simulation. However, many of the salient features of a momentum management control law can be deduced from rather simple analytical models. Analytical models also provide much more human insight into the problem, which allows an analytical approach to the evaluation of a control law. The dependence upon many numerical results where the relationship between inputs and outputs is empirical makes understanding and evaluation difficult at best.

In Section C.1 analytical approximations to the gravity-gradient torque and the resulting angular momentum will be presented. Section C.2 addresses simple approximations to the Earth's magnetic field and the functions of the field that are employed in a momentum management scheme.

C.1 GRAVITY-GRADIENT TORQUE ANALYTICAL MODEL

The fundamental expression for the gravity-gradient torque was given in Equation (3-5) as

$$\vec{T}_{GG} = 3\Omega_o^2 [\hat{R}_V \times (I\hat{R}_V)] \quad (C-1)$$

where all the terms are defined in Section 3.3.

This expression has already incorporated several simplifying assumptions, including a circular spacecraft orbit and a spherical Earth.

Equation (C-1) implies the following: (1) the direction of the torque is normal to the local vertical (\hat{R}_V); (2) the magnitude of the torque varies as the square of the orbital mean motion (inversely proportional to the geocentric distance cubed, Kepler's law); and (3) the torque is zero for a spherically symmetric spacecraft. To deduce further properties of the torque, a coordinate system aligned with the orbital plane is useful. Consider a right-handed coordinate system whose z-axis is directed along the orbital angular momentum vector with the x-axis directed toward any convenient reference in the orbital plane, e.g., the ascending node. Furthermore, let λ and β denote the orbital longitude and latitude of the spacecraft pointing direction, and ϕ denote the roll orientation about the pointing (nominally ϕ will be determined by directing the solar array toward the Sun). With these definitions, \hat{R}_V may be expressed as

$$\hat{R}_V = A_1(\phi) A_2(-\beta) A_3(\lambda) \begin{pmatrix} \cos \mu \\ \sin \mu \\ 0 \end{pmatrix} \quad (C-2)$$

where $A_i(\theta)$ denotes a right-handed rotation transformation about the i th coordinate axis by the angle θ . In this equation, μ is the true anomaly of the orbit, which is given by

$$\mu = \Omega_0 t + \mu_0 \quad (C-3)$$

since circular motion is assumed (Ω_0 is the orbital angular rate). Performing the indicated operations of Equation (C-2) gives the following expression for \hat{R}_V :

$$R_V = \begin{bmatrix} c_\beta c_\psi \\ c_\phi s_\psi - s_\phi s_\beta c_\psi \\ - (s_\phi s_\psi + c_\phi s_\beta c_\psi) \end{bmatrix}$$

where $\psi = \mu - \lambda$ and the notation c_θ and s_θ denotes $\cos \theta$ and $\sin \theta$ respectively.

Let $k_i v_i$ denote the i th component of the vector $\hat{R}_V \times I \hat{R}_V$ where $k_1 = I_{33} - I_{22}$, $k_2 = I_{11} - I_{33}$, and $k_3 = I_{22} - I_{11}$. (I is the inertia matrix, which is assumed to be diagonal; i.e., the torque is expressed in principal axes coordinates.)

Then,

$$\hat{R}_V \times I \hat{R}_V = \begin{pmatrix} k_1 v_1 \\ k_2 v_2 \\ k_3 v_3 \end{pmatrix}$$

and direct substitution of previously defined expressions leads to

$$V = \begin{bmatrix} v_1 \\ v_2 \\ v_3 \end{bmatrix} = \begin{bmatrix} s_\phi c_\phi (s_\beta^2 c_\psi^2 - s_\psi^2) - s_\beta s_\psi c_\psi (c_\phi^2 - s_\phi^2) \\ - c_\beta c_\psi (c_\phi s_\beta c_\psi + s_\phi s_\psi) \\ c_\beta c_\psi (-s_\phi s_\beta c_\psi + c_\phi s_\psi) \end{bmatrix}$$

Use of fundamental trigonometric identities and further manipulations lead to one of the basic results desired, i.e.,

$$\vec{T}_{GG} = \frac{3}{4} \Omega_0^2 [V_1 \cos 2\psi + V_2 \sin 2\psi + V_3] \quad (C-4)$$

where

$$V_1 = \begin{bmatrix} k_1 (1 + s_\beta^2) \sin 2\phi \\ -k_2 c_\phi \sin 2\beta \\ -k_3 s_\phi \sin 2\beta \end{bmatrix} \quad V_2 = 2 \begin{bmatrix} -k_1 s_\beta \cos 2\phi \\ -k_2 c_\beta s_\phi \\ k_3 c_\beta c_\phi \end{bmatrix}$$

$$V_3 = - \begin{bmatrix} k_1 c_\beta^2 \sin 2\phi \\ k_2 c_\phi \sin 2\beta \\ k_3 s_\phi \sin 2\beta \end{bmatrix}$$

The V_i 's are functions of the orientation angles only, hence remain fixed during a given pointing. The properties of Equation (C-4) have been alluded to throughout this document--namely, that the gravity-gradient torque consists of a periodic part with a period of one half-orbit (governed by V_1 and V_2) and a secular part (V_3). Thus, it is the fundamental attributes of this simple analytical expression that gives credence to the concept of an open-loop control law over a half-orbit period.

Many of the momentum management expressions involve the integration of functions over a fixed time domain. Since Equation (C-4) is expressed as a function of an angle which

is a linear function of time (Equation (C-3)), it is convenient to perform the integrations with the angle as the independent variable and use the relationship

$$\int_{t_1}^{t_2} G(t) dt = \frac{1}{\Omega_0} \int_{\psi_1}^{\psi_2} G(\psi) d\psi = \frac{1}{\Omega_0} \int_{\mu_1}^{\mu_2} G(\mu) d\mu$$

where $G(t)$ is any function of time.

The total momentum then over the time interval (t_1, t_2) due to gravity-gradient torque is obtained by direct integration of Equation (C-4), which gives

$$\begin{aligned} \vec{H}_{GG} = \frac{3}{8} \Omega_0 \left[(\sin 2\psi_2 - \sin 2\psi_1) V_1 - (\cos 2\psi_2 - \cos 2\psi_1) V_2 \right. \\ \left. + 2 (\psi_2 - \psi_1) V_3 \right] + \vec{H}_1 \end{aligned}$$

where $\psi_i = \mu_i - \lambda = \Omega_0 t_i + \mu_0 - \lambda$. \vec{H}_1 is a constant of integration that physically corresponds to the momentum in the system at t_1 . Additional trigonometric identities allow simplification of this last expression; namely,

$$\begin{aligned} \vec{H}_{GG} = \frac{3}{4} \Omega_0 \left\{ \sin \eta_1 [V_1 \cos \eta_2 + V_2 \sin \eta_2] \right. \\ \left. + \eta_1 V_3 \right\} + \vec{H}_1 \end{aligned} \tag{C-5}$$

where $\eta_1 = \psi_2 - \psi_1$ and $\eta_2 = \psi_2 + \psi_1$. Over a half-orbit period, the accumulated momentum is

$$H_{GG} = \frac{3}{4} \Omega_0 \Pi V_3$$

The continuous accumulative momentum profile due to gravity-gradient torque is easily obtained by letting the upper limit of integration vary, i.e., $\psi_2 = \psi_1 + \gamma$, where γ is an independent angular variable. Then $\eta_1 = \gamma$, $\eta_2 = 2\psi_1 + \gamma$, and substitution into Equation (C-5) plus more manipulations yields

$$\vec{H}_{GG}(\gamma) = \frac{3}{8} \Omega_o \left[V_1' \cos 2\gamma + V_2' \sin 2\gamma + 2\gamma V_3 - V_1' \right] + \vec{H}_1 \quad (C-6)$$

where

$$V_1' = V_1 \sin 2\psi_1 - V_2 \cos 2\psi_1$$

$$V_2' = V_1 \cos 2\psi_1 + V_2 \sin 2\psi_1$$

Equation (C-6) is important for momentum management sizing considerations, since it clearly shows the amount of momentum introduced into the system as a function of time.

With a closed-loop control law, it is also necessary to evaluate the influence of the periodic torque. This can be accomplished by deriving an expression for $\vec{T}_{GG} \cdot \vec{T}_{GG}$. Before pursuing this idea, however, one more assumption can be made within the order of approximations already considered. The Space Telescope, like many spacecraft, has an approximate cylindrical inertia distribution. Thus, assuming $I_{22} = I_{33}$ gives $k_1 = 0$, $k_3 = -k_2 = k_g$. Under this assumption, the primary equations reduce to

$$\vec{T}_{GG} = \frac{3}{2} \Omega_o^2 k_g c_\beta [s_\beta U_1 \cos 2\psi + U_2 \sin 2\psi + s_\beta U_1] \quad (C-7)$$

$$H_{GG} \begin{vmatrix} \psi_2 \\ \psi_1 \end{vmatrix} = \frac{3}{2} \Omega_0 k_g c_\beta \left\{ \sin \eta_1 [s_\beta U_1 \cos \eta_2 + U_2 \sin \eta_2] \right. \\ \left. + s_\beta \eta_1 U_1 \right\} + \vec{H}_1 \quad (C-8)$$

$$\vec{H}_{GG}(\gamma) = \frac{3}{4} \Omega_0 k_g c_\beta [W_1 \cos 2\gamma + W_2 \sin 2\gamma - W_1 \\ + 2s_\beta \gamma U_1] + \vec{H}_1 \quad (C-9)$$

where

$$U_1 = \begin{bmatrix} 0 \\ c_\phi \\ -s_\phi \end{bmatrix} = A_1(\phi) \begin{bmatrix} 0 \\ 1 \\ 0 \end{bmatrix}, \quad U_2 = \begin{bmatrix} 0 \\ s_\phi \\ c_\phi \end{bmatrix} = A_1(\phi) \begin{bmatrix} 0 \\ 0 \\ 1 \end{bmatrix}$$

$$W_1 = U_1 s_\beta \sin 2\psi_1 - U_2 \cos 2\psi_1$$

$$W_2 = U_1 s_\beta \cos 2\psi_1 + U_2 \sin 2\psi_1$$

Also,

$$\vec{T}_{GG} \cdot \vec{T}_{gg} = \frac{9}{4} \Omega_0^4 k_g^2 c_\beta^2 (1 + s_\beta^2 + 2 s_\beta^2 \cos 2\psi - c_\beta^2 \cos^2 2\psi)$$

The average total torque magnitude is

$$\left(\int T_{GG} \cdot T_{GG} \right)^{1/2} / 1/2P = 3/2 \Omega_0^2 k_g c_\beta \sqrt{1/2 (1 + 3s_\beta^2)}$$

The following properties can now be summarized about the gravity-gradient torque (for the assumptions made):

- The total torque (periodic and secular) lies in the V_2 - V_3 plane.

- The periodic torque forms an ellipse with one axis directed toward the secular torque.
- The secular torque has a maximum of $3/4 \Omega_o^2 k_g$ when the pointing is 45 degrees from the orbital plane ($\beta = 45^\circ$). This vanishes for pointings in the orbital plane and pointings perpendicular to the orbital plane.
- The periodic torque is a maximum for orbital plane pointings.
- The maximum instantaneous torque is $3/2 \Omega_o^2 k_g$ for $\beta \leq 45$ degrees or $3/2 \Omega_o^2 k_g \sin 2\beta$ for $\beta > 45$ degrees.
- The maximum average torque is approximately $1.23 \Omega_o^2 k_g$, which occurs approximately when $\beta = 35.3$ degrees
- All torques vanish for pointings toward the orbital poles.

All of the previous expressions and derivations have been relative to the spacecraft principal axes coordinate. Similar expressions relative to orbital plane coordinates may be obtained by applying the inverse transformation of Equation (C-2) to the vectors U_i and W_i ; e.g., the torque expressed in orbit plane coordinates is given by

$$\vec{T}_{GGO} = 3/2 \Omega_o^2 k_g c_\beta \left[s_\beta U_1' \cos 2\psi + U_2' \sin 2\psi + s_\beta U_1' \right] \quad (C-10)$$

where

$$U_i' = A_3^{-1}(\lambda) A_2^{-1}(-\beta) A_1^{-1}(\phi) U_i$$

Let $\epsilon_1 = (0, 1, 0)^T$ and $\epsilon_2 = (0, 0, 1)^T$; then

$U_i = A_1(\phi)\epsilon_i$, ($i = 1, 2$). Hence, $U_i' = A_3^{-1}(\lambda) A_2^{-1}(-\beta) \epsilon_i$
or, explicitly,

$$U_1' = \begin{bmatrix} -\sin \lambda \\ \cos \lambda \\ 0 \end{bmatrix} = \begin{bmatrix} \cos (\lambda + 90) \\ \sin (\lambda + 90) \\ 0 \end{bmatrix}$$

$$U_2' = \begin{bmatrix} -\cos \lambda \sin \beta \\ -\sin \lambda \sin \beta \\ \cos \beta \end{bmatrix}$$

Thus, the secular torque always lies in the orbital plane 90 degrees from the projection of the pointing. If the limits of integration are symmetrical relative to the projection of the pointing on the orbital plane--i.e.,

$\psi_1 = \lambda - L$, $\psi_2 = \lambda + L$, $\eta_1 = 2L$, and $\eta_2 = 0$

(Equation (C-8))--then all the momentum is directed toward

U_1' with magnitude $3/4 \Omega_0 k_g \sin 2\beta (\eta_1 + \sin \eta_1)$.

C.2 MAGNETIC FIELD ANALYTICAL MODEL

The magnetic dipole model of the geomagnetic field is given by the vector equation (Reference 3-3)

$$\vec{B}(R) = \frac{a^3 H_0}{r^3} \left[3(\hat{m} \cdot \hat{R}) \hat{R} - \hat{m} \right]$$

where \vec{R} is the position vector of the spacecraft, \hat{R} is the unit vector in the direction of \vec{R} , and r is the length of \vec{R} . $a^3 H_0$ is a constant whose value is approximately 7.943×10^{15} Weber-meters (evaluated for 1978), and \hat{m} is the unit vector directed toward the dipole north pole (terrestrial southern hemisphere) i.e., the latitude and longitude of the dipole are 78.6 S and 109.3 E (1978). For a circular orbit, r remains constant. Therefore, in this case, the dipole model may be expressed as

$$\vec{B}(R) = k_m [3(\hat{m} \cdot \hat{R}) \hat{R} - \hat{m}] \quad (C-11)$$

where k_m is a constant.

The direction of m varies as the Earth rotates so that the total directional change is approximately 20 degrees in 12 hours. However, over a small part of a day (like a half-orbit of a near-Earth satellite), \hat{m} will not vary significantly since it lies near the axis of rotation. In 1 hour, for example, \hat{m} will remain within 1.5 degrees of a mean direction. Thus, to a reasonable approximation, Equation (C-11) can be used to represent the magnetic field relative to a fixed reference system. It should be noted that the intent of the models in this section is for an understanding of the nature of momentum management schemes--these models may not be sufficiently accurate for actual implementation. Actually the simplification made here represents

a worst case condition for momentum management, since the true field will have more variability than the analytic model used here.

The unit vector \hat{R} may be expressed as

$$\hat{R} = \cos \mu \hat{P} + \sin \mu \hat{Q}$$

where \hat{P} and \hat{Q} are orthonormal vectors in the orbital plane and μ is the true anomaly angle of the orbit. Substitution of this last expression into Equation (C-11) and the use of trigonometric identities leads to the simple form

$$\vec{B} = \frac{3}{2} k_m [\cos 2\mu B_1 + \sin 2\mu B_2 + B_3] \quad (C-12)$$

where $B_1 = m_1 \hat{P} - m_2 \hat{Q}$, $B_2 = m_1 \hat{Q} + m_2 \hat{P}$, $B_3 = m_1 \hat{P} + m_2 \hat{Q} - 2/3 \hat{m}$, $m_1 = \hat{m} \cdot \hat{P}$, and $m_2 = \hat{m} \cdot \hat{Q}$.

It is also straightforward to show that: $B_1 \cdot B_2 = 0$ and $B_1^2 = B_2^2 = m_1^2 + m_2^2 = 1 - m_3^2$ where $m_3 = \hat{m} \cdot (\hat{P} \times \hat{Q})$.

Equation (C-12) demonstrates that the magnetic vector and the gravity-gradient torque share similar properties--namely, a constant component and a simple periodic component with a period of one half-orbit. The periodic contribution always lies in the orbital plane, is identically zero when \hat{m} is directed toward the orbital pole, and has maximum amplitude when \hat{m} lies in the orbital plane. The constant part (B_3) is not truly constant, since it includes m , but, as stated before, it can be assumed fixed for a small fraction of a day. Its influence on a momentum management scheme will depend upon the particular fixed direction. Note that the mathematical form of both the magnetic field and the

gravity-gradient torque is of the same functional form. This facilitates the manipulations of these forms (e.g., integration).

The dyadic form $\tilde{B}^2 = -\tilde{B}\tilde{B}^T = -\tilde{B}^T\tilde{B}$ plays a dominant role in all of the momentum management control laws (assuming that the weighting matrix is the identity). This is particularly true in an open-loop law, which requires that the inverse of the integral exist. The functional form of \tilde{B}^2 is obtained directly from Equation (C-12):

$$\tilde{B}^2 = 9/4 k_m^2 \left[\cos^2 2\mu \tilde{B}_1^2 + \sin 2\mu \cos 2\mu (\tilde{B}_1\tilde{B}_2 + \tilde{B}_2\tilde{B}_1) + \sin^2 2\mu \tilde{B}_2^2 + \tilde{B}_3^2 + \tilde{G}\tilde{B}_3 + \tilde{B}_3\tilde{G} \right]$$

where G represents the cyclic part of B ; i.e., $G = \cos 2\mu B_1 + \sin 2\mu B_2$. This last relationship may also be written in the form

$$\tilde{B}^2 = 9/8 k_m^2 \left[C_\psi \cos 4\mu + D_4 \sin 4\mu + C_2 \cos 2\mu + D_2 \sin 2\mu + C_0 \right] \quad (C-13)$$

where

$$C_4 = \tilde{B}_1^2 - \tilde{B}_2^2$$

$$D_4 = (\tilde{B}_1\tilde{B}_2 + \tilde{B}_2\tilde{B}_1)$$

$$C_2 = 2(\tilde{B}_1\tilde{B}_3 + \tilde{B}_3\tilde{B}_1)$$

$$D_2 = 2(\tilde{B}_2\tilde{B}_3 + \tilde{B}_3\tilde{B}_2)$$

and

$$C_0 = \tilde{B}_1^2 + \tilde{B}_2^2 + 2 \tilde{B}_3^2$$

The torque, \vec{T}_M , produced by the magnetic field interaction with the coil field, is always of the form $\vec{T}_M = \tilde{B}\tilde{B}^T\vec{P}$, where \vec{P} is a fixed vector for an open-loop law and varies like the gravity-gradient torque in a closed-loop law. The expression above then clearly shows that the magnetic torque profile has a fourth harmonic component even in the simplest case. The analytical gravity-gradient model had only second harmonics. Therefore, the resultant momentum profile that is the integral of the sum of magnetic and gravity-gradient torques will also have fourth harmonics. In truth, both torques will have many higher harmonics, since their true functional forms are more complex than those presented here. The influence of this fourth harmonic on the nominal momentum profile needed for open-loop laws is included in the simulation results of Section 7.2.1.

The integral of \tilde{B}^2 is now easily obtained by the integration of simple trigonometric forms, in particular

$$\int_{\mu_0}^{\mu_0+\Pi} \tilde{B}^2 d\mu = 9/8 k_m^2 \Pi [\tilde{B}_1^2 + \tilde{B}_2^2 + 2 \tilde{B}_3^2] \quad (C-14)$$

Integrals over the time domain are obtained by dividing by the orbital angular rate Ω_0 as was done with the torque equations.

For a fixed vector V , the matrix $\hat{V}^2 = VV^T - V \cdot VI$ is singular (I is the identity matrix). Since $B_1 = B_2 = 0$ when \hat{m} is perpendicular to the orbital plane, it is clear that the expression in Equation (C-14) does not possess an

inverse in this case. Later an expression for the determinant of Equation (C-14) will be developed that illustrates how it approaches zero as \hat{m} approaches the orbital pole. It is also clear that as the range of integration decreases, the definite integral matrix of \tilde{B}^2 approaches the null matrix, and thus lacks an inverse.

The magnetic field expressions developed thus far have been independent of a particular coordinate system. However, as was the case with the torque models, additional insight may be gained by employing orbital plane coordinates. In particular, the introduction of the orbital latitude and longitude of \hat{m} (similar to the pointing angles) is helpful. Let β_m denote the orbital latitude of \hat{m} (positive direction toward the orbital momentum vector) and λ_m represent the orbital longitude (positive direction toward orbital velocity vector), then

$$\hat{m} = \begin{bmatrix} m_1 \\ m_2 \\ m_3 \end{bmatrix} = \begin{bmatrix} \cos \beta_m \cos \lambda_m \\ \cos \beta_m \sin \lambda_m \\ \sin \beta_m \end{bmatrix}$$

In this coordinate system,

$$B_1 = \cos \beta_m Y_1$$

$$B_2 = \cos \beta_m Y_2$$

$$Y_1^T = (\cos \lambda_m, -\sin \lambda_m, 0)$$

$$Y_2^T = (\sin \lambda_m, \cos \lambda_m, 0)$$

$$B_3^T = \frac{1}{3} (\cos \beta_m \cos \lambda_m, \cos \beta_m \sin \lambda_m, -2 \sin \beta_m) = \cos \beta_m B_3'^T$$

and

$$B_3'^T = \frac{1}{3} (\cos \lambda_m, \sin \lambda_m, -2 \tan \beta_m)$$

Thus,

$$\begin{aligned} \vec{B} &= \frac{3}{2} k_m [\cos \beta_m (\cos 2\mu Y_1 + \sin 2\mu Y_2) + B_3] \\ &= \frac{3}{2} k_m \cos \beta_m [\cos 2\mu Y_1 + \sin 2\mu Y_2 + B_3'] \end{aligned}$$

The vectors Y_1 and Y_2 lie in the orbital plane and are orthonormal. Hence, the cyclic component of \vec{B} traces out a circle in the orbital plane, and the radius of the circle is proportional to $\cos \beta_m$. The magnitude of the vector B_3 is $1/3\sqrt{1 + 3 \sin^2 \beta_m}$ and has an orbital latitude β_3 related to β_m by $\tan \beta_3 = 2 \tan \beta_m$. The direction of \vec{B} always lies along the parallel of orbital latitude β_3 .

The magnitude of \vec{B} squared (B^2) is given by

$$B^2 = k_m^2 \left[1 + 3 \cos^2 \beta_m \cos^2 (\mu - \lambda_m) \right]$$

which has a minimum of k_m^2 , a maximum of $k_m^2 (1 + 3 \cos^2 \beta_m)$, and a mean value of $k_m^2 (1 + 3/2 \cos^2 \beta_m)$.

The terrestrial latitude of \hat{m} is approximately -78.6 degrees; therefore, the orbital latitude β_m takes on its extreme values when $\sin \beta_m = \sin(-78.6 \pm i)$ where i is the inclination of the orbital plane.

Assuming $i = 28.8$ degrees for ST implies $-72.6 \leq \beta_m \leq -49.8$, $67.1 \leq \beta_3 \leq 81.1$, $0.55 \leq |B_3| \leq 0.64$, and $k_m \leq |B| \leq 1.5 k_m$.

Let C_0 denote the symmetric matrix which appears inside the brackets of Equation (C-14); i.e., $C_0 = B_1^2 + B_2^2 + 2 B_3^2$ and $S = -9C_0$. Then the elements of S are given by

$$s_{11} = 8 + \cos^2 \beta_m (1 + 2 \sin^2 \lambda_m)$$

$$s_{22} = 8 + \cos^2 \beta_m (1 + 2 \cos^2 \lambda_m)$$

$$s_{33} = 20 \cos^2 \beta_m$$

$$s_{12} = s_{21} = -\cos^2 \beta_m \sin 2 \lambda_m$$

$$s_{13} = s_{31} = 2 \sin 2\beta_m \cos \lambda_m$$

$$s_{23} = s_{32} = 2 \sin 2\beta_m \sin \lambda_m$$

The determinant of S , $d(S)$, is given by $d(S) = 36 \cos^2 \beta_m (3 \cos^2 \beta_m + 8) (\cos^2 \beta_m + 4)$ which is zero if and only if $\beta_m = 90$ degrees. The elements of the adjoint matrix of S , S^* , which is useful in obtaining the inverse of S ($SS^* = S^*S = d(S)I$), are given by the following expressions:

$$s_{11}^* = 4 \cos^2 \beta_m \left[36 + 9 \cos^2 \beta_m + 2 \cos^2 \lambda_m (3 \cos^2 \beta_m + 2) \right]$$

$$s_{22}^* = 4 \cos^2 \beta_m \left[40 + 15 \cos^2 \beta_m - 2 \cos^2 \lambda_m (3 \cos^2 \beta_m + 2) \right]$$

$$s_{33}^* = 3 \cos^4 \beta_m + 32 \cos^2 \beta_m + 64$$

$$s_{12}^* = s_{21}^* = 8 \cos^2 \beta_m \sin \lambda_m \cos \lambda_m (3 \cos^2 \beta_m + 2)$$

$$s_{13}^* = s_{31}^* = -4 \sin \beta_m \cos \beta_m \cos \lambda_m (3 \cos^2 \beta_m + 8)$$

$$s_{23}^* = s_{32}^* = -4 \sin \beta_m \cos \beta_m \sin \lambda_m (3 \cos^2 \beta_m + 8)$$

To summarize these last few results in matrix form, let

$$\begin{aligned} C &= \int_{\mu_0}^{\mu_0 + \Pi} \tilde{B}^2 d\mu = \frac{9}{8} k_m^2 \Pi \left[\tilde{B}_1^2 + \tilde{B}_2^2 + 2 \tilde{B}_3^2 \right] \\ &= \frac{9}{8} k_m^2 \Pi C_0 \\ &= -\frac{1}{8} k_m^2 \Pi S \end{aligned}$$

Then

$$C^{-1} = \frac{-8}{k_m^2 \Pi} S^{-1} = \frac{-8}{k_m^2 \Pi d(S)} S^*$$

Recall that the integral C is evaluated over a half-orbit using the orbital angle as the independent parameter. Integration over the time domain is obtained by dividing C by the orbital angular rate, ω_0 .

At least one eigenvalue of C^{-1} will approach infinity as $\cos \beta_m$ approaches zero. The eigenvector corresponding to this eigenvalue will then be greatly amplified by the transformation C^{-1} as $\cos \beta_m$ nears zero; i.e., the costate vector $P = C^{-1}H_D$ may become large if H_D is in the direction of this eigenvector when $\cos \beta_m$ is small. Since the amount of energy needed to produce a desired magnetic torque is proportional to the length of P , it is clear that the required energy is very dependent upon the direction of the magnetic dipole as well as the relative direction of the momentum vector; e.g., the maximum momentum length condition ($\beta = 45$) is not necessarily the maximum energy condition.

The integral of \tilde{B}^2 , Equation (C-13), over arbitrary limits μ_1 to μ_2 is given by

$$\int_{\mu_1}^{\mu_2} \tilde{B}^2 d\mu = \frac{9}{8} k_m^2 \left\{ \sin \theta_1 \left[\cos \theta_1 (C_4 \cos 2\theta_2 + D_4 \sin 2\theta_2 + C_2 \cos \theta_2 + D_2 \sin \theta_2) \right] + \theta_1 C_0 \right\}$$

where $\theta_1 = \mu_2 - \mu_1$ and $\theta_2 = \mu_1 + \mu_2$. This last expression is proportional to θ_1 for small values of θ_1 , and thus approaches zero as the range of integration is shortened.